FUNCTIONAL IMAGING OF THE ANESTHETIZED BRAIN IN PRIMATES AND RODENTS

DISSERTATION

for the award of the degree
"Doctor rerum naturalium" (Dr. rer. nat.)
of the Georg-August-Universität Göttingen

within the doctoral program IMPRS Neurosciences
of the Georg-August University School of Sciences (GAUSS)

submitted by

NIKOLOZ SIRMPILATZE

from Kutaisi, Georgia

Göttingen, 2021

THESIS COMMITTEE:

Prof. Dr. Susann Boretius
Functional Imaging Laboratory, German Primate Center (DPZ), Göttingen

Prof. Dr. Jochen Staiger
Department of Neuroanatomy, University Medical Center Göttingen (UMG)

Prof. Dr. Hansjörg Scherberger
Neurobiology Laboratory, German Primate Center (DPZ), Göttingen

MEMBERS OF THE EXAMINATION BOARD:

Referee: Prof. Dr. Susann Boretius
Functional Imaging Laboratory, German Primate Center (DPZ), Göttingen

2nd Referee: Prof. Dr. Jochen Staiger
Department of Neuroanatomy, University Medical Center Göttingen (UMG)

FURTHER MEMBERS OF THE EXAMINATION BOARD:

Prof. Dr. Hansjörg Scherberger
Neurobiology Laboratory, German Primate Center (DPZ), Göttingen

Prof. Dr. Christine Stadelmann-Nessler
Institute for Neuropathology, University Medical Center Göttingen (UMG)

PD Dr. Peter Dechent
Department of Cognitive Neurology, University Medical Center Göttingen (UMG)

Prof. Dr. Ralf Heinrich
Department of Cellular Neurobiology, Georg-August University of Göttingen

Date of oral examination: September 14th 2021

"The only thing we know about consciousness
is that it is soluble in *chloroform*."

— Luca Turin

And to me that idea, when we finally discover it,
will be so compelling, and so inevitable, so beautiful,
we will all say to each other,
"How could it have ever been otherwise?"

— John Wheeler

In the loving memory of my mother, Eirini Zantidou.

ABSTRACT

Understanding the brain is aided by visualizing neural activity over time. The most popular method for doing so in humans is functional magnetic resonance imaging (fMRI)—a method that tracks blood oxygenation as a proxy for neural activity. fMRI relies on neurovascular coupling, the brain's capacity to increase its blood supply locally and on demand. Apart from humans, fMRI can be also applied to experimental animals and thereby plays an essential role in translating findings across species. Additionally, the combination of animal fMRI with electrophysiological and optical methods is crucial for uncovering the neural correlates of the observed blood-oxygen-level-dependent (BOLD) fMRI signal. Since fMRI necessitates immobility, animals must be either restrained or anesthetized. Most researchers take the latter approach, for both practical and ethical reasons. However, anesthesia confounds the results of fMRI experiments by profoundly altering neural activity and by interfering with neurovascular coupling. This conundrum, which can be viewed both as a *challenge* and an *opportunity*, motivated the three studies presented in this thesis.

The *challenge* lies in choosing the right anesthesia for animal fMRI experiments. The ideal anesthetic protocol must provide sufficient sedation, guarantee immobility, and crucially, preserve a degree of neural responsiveness and neurovascular coupling. Anesthetic protocols based on the continuous infusion of the sedative medetomidine exhibit these qualities and have thus become a popular choice for rats—the most widely used animal fMRI model. Despite this, it has not yet been established how fMRI readouts evolve over several hours of medetomidine anesthesia and how they are affected by variations in timing, dose, and route of administration. In my first study (Chapter 2), I used four different protocols of medetomidine administration to anesthetize rats for up to six hours and repeatedly evaluated stimulus-evoked responses and fMRI measures of functional connectivity. I found that the temporal evolution of fMRI readouts varied between administration schemes. Based on the results, I made recommendations regarding the administration of medetomidine and the timing of fMRI experiments. These factors are important for obtaining reproducible results and should be considered for the design and interpretation of future rat fMRI studies.

The *opportunity* lies in exploiting anesthesia's effects on fMRI to better understand large-scale phenomena in the anesthetized brain. The case in point is burst-suppression, a poorly understood pattern of neural activity that appears in deep anesthesia and coma. In animals anesthetized with isoflurane, burst-suppression has been associated with the widespread synchronization of brain areas. In the second study (Chapter 3), I used fMRI data from four species—humans, macaques, marmosets, and rats—to precisely describe the fMRI signatures of anesthesia-induced burst-suppression and to map their distribution across the brain. I discovered a marked difference between primates and rodents. In rats the entire neocortex engaged in burst-suppression, while in the three primate species certain cortical areas were excluded—most notably the visual cortex. Based on the fMRI data alone, I could not determine the underlying cause of this exclusion. I concluded

that answering this question would necessitate direct recordings of neural activity in the visual cortex of both primates and rodents.

In the third study (Chapter 4), I aimed to develop the methods required for such direct neural recordings. Specifically, I conducted a series of pilot experiments in isoflurane-anesthetized rats and demonstrated the feasibility of *in vivo* two-photon calcium imaging through chronically implanted cranial windows. I was able to record the activity of hundreds of layer 2/3 neurons in the rat somatosensory and visual cortex and confirm my previous findings regarding the pancortical distribution of burst-suppression. I also examined the effects of varying the isoflurane dose on spontaneous activity and stimulus-evoked responses, thereby reproducing several known properties of burst-suppression in rodents. The developed methods can be easily adapted to record from the marmoset visual cortex, with the aim of understanding the primate-rodent difference described in Chapter 3.

The above studies showcase that anesthetizing animals for functional neuroimaging experiments should not be viewed as a necessary evil. Anesthetic protocols can be optimized to allow for a host of neuroscientific questions to be asked. Moreover, such experiments can shed light on the functional organization of the anesthetized brain and on elusive anesthetic mechanisms of actions.

CONTENTS

I THESIS CHAPTERS 1

1 GENERAL INTRODUCTION 3
- 1.1 Functional magnetic resonance imaging (fMRI) . . . 4
  - 1.1.1 Nuclear Magnetic Resonance (NMR) . . . 4
  - 1.1.2 Blood-oxygen-level-dependent (BOLD) contrast . . . 6
  - 1.1.3 Neurovascular coupling . . . 6
  - 1.1.4 Common approaches for experimental design and analysis . . . 7
- 1.2 fMRI in experimental animals . . . 9
  - 1.2.1 Medetomidine . . . 11
  - 1.2.2 Isoflurane . . . 12
- 1.3 Optical methods . . . 13
  - 1.3.1 Neuronal calcium imaging . . . 13
  - 1.3.2 Two-photon microscopy . . . 14
- 1.4 Study summaries . . . 14
  - 1.4.1 Study A: Chapter 2 . . . 14
  - 1.4.2 Study B: Chapter 3 . . . 15
  - 1.4.3 Study C: Chapter 4 . . . 16

2 STUDY A: ATTACHED REPRINT OF PUBLISHED MANUSCRIPT 17

3 STUDY B 31
- 3.1 Introduction . . . 32
- 3.2 Results . . . 34
  - 3.2.1 fMRI signatures of EEG-defined burst-suppression in humans . . . 34
  - 3.2.2 Mapping burst-suppression in humans without EEG . . . 37
  - 3.2.3 Burst-suppression maps in nonhuman primates resemble the human map . . . 37
  - 3.2.4 Burst-suppression in rats is pancortical . . . 43
  - 3.2.5 The primate V1 is uncoupled from the rest of the cortex during burst-suppression . . . 45
- 3.3 Discussion . . . 46
- 3.4 Methods . . . 49
  - 3.4.1 Experimental subjects and anesthesia . . . 49
  - 3.4.2 MRI acquisition . . . 51
  - 3.4.3 MRI preprocessing . . . 53
  - 3.4.4 Carpet plots and PCA . . . 55
  - 3.4.5 Correspondence to EEG . . . 56
  - 3.4.6 Burst suppression maps . . . 56
  - 3.4.7 Region-of-interest analysis . . . 57

4 STUDY C 59
- 4.1 Introduction . . . 60
  - 4.1.1 Motivation . . . 60

4.1.2 Neural recording techniques . . . 61
4.1.3 Stimulus modalities . . . 63
4.1.4 Study scope and goals . . . 63
4.2 Materials and Methods . . . 64
4.2.1 Animals . . . 64
4.2.2 Experimental timeline . . . 64
4.2.3 Viral constructs . . . 64
4.2.4 Implants . . . 67
4.2.5 Surgery . . . 67
4.2.6 Two-photon calcium imaging . . . 69
4.2.7 Histology . . . 71
4.2.8 Sensory and optogenetic stimulation . . . 71
4.2.9 Two-photon image processing . . . 71
4.2.10 Detection of bursts . . . 73
4.3 Results . . . 73
4.3.1 Animal survival and implant longevity . . . 73
4.3.2 Neuronal expression of calcium indicators . . . 74
4.3.3 Burst-suppression across isoflurane doses . . . 76
4.3.4 Stimulus-evoked bursts . . . 78
4.4 Discussion . . . 78
4.4.1 Methodological considerations . . . 81
4.4.2 The anesthetic dose-dependency of burst-suppression . . . 83
4.4.3 Stimulus-evoked bursts . . . 83
4.4.4 From rats to marmosets . . . 84
5 GENERAL DISCUSSION 85
5.1 Anesthesia as a necessary evil . . . 85
5.2 Investigating anesthetic mechanisms of action . . . 86
5.3 Anesthesia as a tool for understanding unconscious states . . . 86

II APPENDIX 89

A SUPPLEMENTARY MATERIAL 91

BIBLIOGRAPHY 103

LIST OF FIGURES

Figure 1.1 Typical fMRI experimental design and analysis . . . 8
Figure 3.1 fMRI signatures of human burst-suppression . . . 36
Figure 3.2 Human map of burst-suppression . . . 38
Figure 3.3 Identifying and mapping burst-suppression in macaques . . . 39
Figure 3.4 Identifying and mapping burst-suppression in marmosets . . . 40
Figure 3.5 Identifying and mapping burst-suppression in rats . . . 42
Figure 3.6 The primate V1 is uncoupled from the rest of the cortex during burst-suppression . . . 44
Figure 4.1 Surgeries and cranial implants . . . 65
Figure 4.2 Experimental timelines per animal . . . 70
Figure 4.3 Neuronal expression of calcium indicators . . . 75
Figure 4.4 Burst-suppression across isoflurane doses . . . 77
Figure 4.5 Responses to sensory stimulation . . . 79
Figure 4.6 Responses to optogenetic stimulation . . . 80
Figure A.1 Examples of fMRI runs without asymmetric PCs . . . 91
Figure A.2 Correlation of subcortical structures with burst-suppression in humans and macaques . . . 92
Figure A.3 Correlation of subcortical structures with burst-suppression in marmosets and rats . . . 93
Figure A.4 Ventricular motion during burst-suppression . . . 94
Figure A.5 Identifying and mapping burst-suppression in the Rat 2 dataset . . . 95
Figure A.6 Unthresholded burst-suppression maps across species . . . 96
Figure A.7 Temporal signal-to-noise (tSNR) maps across species . . . 97
Figure A.8 BOLD signal timeseries across sevoflurane doses in humans . . . 98
Figure A.9 Burst-suppression timescales across species . . . 99
Figure A.10 ROI detection and cell classification . . . 101

LIST OF TABLES

Table 3.1 Datasets analyzed in this study 34
Table 4.1 The allocation of viral constructs to injection sites per animal . . . 66
Table 4.2 Analyzed two-photon calcium imaging recordings 72
Table 4.3 Number of detected cells and maximum fluorescence change (maxΔF/F) per imaged window 74
Table 4.4 Burst-suppression across isoflurane doses 76
Table A.1 Repeated-measures ANOVA results for Supplementary Figure A.8 100
Table A.2 Post-hoc pairwise tests for Supplementary Figure A.8 100

Part I

THESIS CHAPTERS

1

GENERAL INTRODUCTION

"What are you doing with those?" asked Orsino. Berkowitz said, "At a guess, she's been scanning the marmoset brain. Have you, Jenny?"
"I started considerably lower in the animal scale."
She opened the cage and took out one of the marmosets, which looked at her with a miniature sad-old-man-with-sideburns expression. She clucked to it, stroked it and gently strapped it into a small harness.
Orsino said, "What are you doing?".
"I can't have it moving around if I'm going to make it part of a circuit, and I can't anesthetize it without vitiating the experiment."

— "Think!" by Isaac Asimov

The above excerpt is from the short story *Think!* by Isaac Asimov, first published in 1977. The characters, whom today we would call neuroscientists, have invented a novel brain scanning technology. Their method, the 'laser encephalogram (LEG)', has apparently attained the holy grail of neuroscience: rapidly scanning every brain cell *in vivo* without destroying it. They apply this method to a restrained marmoset monkey, though they mention that they "started considerably lower in the animal scale". One of the characters inquires about the necessity of animal restraint and gets the following prescient answer from the lead scientist: "I can't have it moving around if I'm going to make it part of a circuit, and I can't anesthetize it without vitiating the experiment." This issue is as relevant for neuroscientists today as it was for the fictional characters in the story, and has motivated this thesis.

Neuroscience may still be very far from inventing the LEG but has, nonetheless, no shortage of impressive neuroimaging methods that stretch the limits of modern technology. Perhaps the most (in)famous such method, which has dominated human neuroscience since the 1990s, is functional magnetic resonance imaging (fMRI). fMRI is the main method used throughout this thesis, and we will therefore invest some time in introducing it. We will explore its physical principles, its capabilities, and its limitations—i.e. all the ways in which it differs from an LEG (Section 1.1). fMRI may primarily be a human neuroscience method but its history also "started considerably lower in the animal scale", and animals still have a major role to play. We will introduce the field of 'small animal fMRI' and its importance for neuroscientific research (see Section 1.2). However, the use of experimental animals in fMRI poses a challenge. Like many imaging techniques, fMRI is sensitive to motion, and the image quality suffers terribly from it. To overcome this issue,

scientists employ one of the approaches suggested by the lead scientist in *Think!*: they either restrain the animals or they anesthetize them. One could say that they are stuck between a rock and a hard place: restraint entails a host of practical and ethical difficulties, while anesthesia confounds the experiment by dramatically altering brain activity.

This thesis is about the second solution, as it is being applied to fMRI. Anesthesia affects brain activity in complex ways, both via its direct neuronal effects, but also through its influence on the vascular system and the cardio-respiratory physiology. Therefore, conducting fMRI studies under anesthesia and interpreting their results is a challenging endeavor, fraught with uncertainty. Nevertheless, scientists have taken on the challenge by pursuing the ideal anesthetic protocol for fMRI—a protocol that will keep the animal sufficiently sedated while having minimal effects on key physiological processes. The first study of this thesis, presented in Chapter 2, contributes towards that goal by aiming to advance the standardization of anesthetic protocols used for fMRI in rats.

Anesthetic effects on fMRI can be viewed as more than a limitation. Shifting our perspective, we can also see them as an opportunity: fMRI may be used to better understand the functional state of the anesthetized brain. We hope that the second study, presented in Chapter 3 will cast light on this line of thinking. In it, we exploit the confounding effects of anesthesia on fMRI to investigate burst-suppression—a pattern of synchronous neural activity that occurs during deep anesthesia and coma. We take advantage of fMRI's capacity to be applied across the 'animal scale' by exploring burst-suppression in rats, nonhuman primates, and humans.

Finally, in the third study (Chapter 4) we dive deeper into burst-suppression via an additional neuroimaging method—two-photon calcium imaging. This method's working principles (introduced in Section 1.3) lend it somewhat more resemblance to the fabled LEG. We will conclude the introductory chapter by providing summaries for the three studies that compose this thesis (Section 1.4).

1.1 FUNCTIONAL MAGNETIC RESONANCE IMAGING (FMRI)

1.1.1 *Nuclear Magnetic Resonance (NMR)*

One of the four fundamental properties characterizing every nucleus of an atom is the so-called spin, which gives rise to the spin angular momentum. Nuclei with a net spin also possess a magnetic dipole moment, proportional to their spin angular momentum. The most abundant nucleus in biological tissues—the hydrogen nucleus ^{1}H, has an associated spin number of $1/2$, which endows it with useful magnetic properties. In the absence of an external magnetic field, the magnetic moment vectors of hydrogen nuclei are randomly oriented in space. Upon the application of an external field (B_0), the vectors align along the magnetic field lines in two possible orientations: either parallel ('spin-up' state) or anti-parallel ('spin-down' state) to the field. More nuclei end up in the energetically favorable spin-up state, giving rise to a macroscopic net magnetization vector. The proportion of nuclei that occupy either state follows the Boltzmann distribution and depends on the B_0 strength. A higher magnetic field strength results in a larger excess of spin-up nuclei, and thus a larger net magnetization vector. Due to the spin angular momentum, the nuclei are not statically aligned with the field axis but instead are in precessional motion around it.

An often-used mechanical analogy is the spinning top, which precesses around the axis of gravity. The precessional frequency (ω_o, also called the Larmor frequency) is proportional to B_o, following the Larmor equation: $\omega_o = \gamma \cdot B_o$. The proportionality constant γ is called the gyromagnetic ratio, with a value of 42.58 MHz/T for ^1H.

According to the above principles, we could describe a patient lying inside a standard 3 T clinical MRI scanner as being in the following equilibrium state: the patient's ^1H nuclei are generating a net magnetization vector along the axis of the scanner's magnetic field (longitudinal magnetization vector) and are precessing around that axis with a frequency of ≈128 MHz. Several additional steps are needed to convert the longitudinal magnetization into useful signal. First, the equilibrium state is disturbed through the application of an additional magnetic field (B_1) perpendicular to B_o, in the form of a radiofrequency pulse (the excitation pulse). The excitation pulse frequency must equal the precessional (Larmor) frequency of hydrogen to fulfil the so-called 'resonance condition' and enable energy transfer. The transferred energy flips some nuclei into the higher-energy spin-down state and causes them to precess in phase. On a macroscopic scale, this tilts the net magnetization vector away from B_o by a given flip angle (commonly 90°). The vector now has a component in the plane perpendicular to B_o—the so-called transverse magnetization, which also rotates with the Larmor frequency. The rotating transverse vector induces an oscillating current at a nearby antenna (the 'receiver coil'). The voltage induced at the coil's end constitutes the raw NMR signal.

Following excitation, the system returns to equilibrium through two independent relaxation processes—longitudinal (T_1) and transverse (T_2) relaxation. The T_1 process depends on the interaction of spins with their environment: thermal motion in surrounding molecules leads to microscopic magnetic field fluctuations that constantly cause spins to flip. Over time, more spins will tend to return to the energetically favorable spin-up configuration, leading to a recovery of the original longitudinal magnetization. T_2 relaxation results from individual spin-spin interactions that alter their precessional frequencies and lead to a loss of their phase coherence over time (dephasing). Macroscopically this translates into a decay of the transverse magnetization vector, and hence, the received NMR signal. Both processes are exponential, and occur simultaneously at different time-scales, with the associated time constants also named T_1 and T_2. In biological tissues and at conventional magnetic field strengths, T_1 times are typically in the order of a few seconds, while T_2 times in the order of tens to hundreds of milliseconds. The precise time-constants vary depending on the tissue, which is what ultimately leads to the visible tissue contrast on MRI images. This is achieved by manipulating several parameters of the excitation-relaxation cycle, which is repeated multiple times during MRI data acquisition. Two important parameters are the repetition time (TR)—the time between consecutive excitations, and the echo time (TE)—the time between an excitation pulse and the readout of the NMR signal. These and other parameters can be adjusted to maximize differences in the signal received from tissues of interest. For example, an image can be made sensitive to tissue differences in T_1 (T_1-weighted image) or T_2 (T_2-weighted image) times.

T_1 and T_2 are by far not the only options. MRI physicists have come up with ingenious ways to force the hydrogen nuclei to dance to their will. During MRI data acquisition, the scanner receives a set of programmed instructions—called the pulse sequence—that precisely regulates the transmission/reception of radiofrequency pulses and the switching of

multiple secondary magnetic field gradients. The pulse sequence parameters determine the contrast on the resulting image and the tissue properties it represents. The possibilities are endless, limited only by the ingenuity of the pulse programmer—the conductor of spins. The contrast in MRI images can be thus tailored to specific clinical and research questions by making it sensitive to properties of interest, such as diffusion, perfusion, or magnetic susceptibility. The relevant property for fMRI is blood oxygenation.

1.1.2 *Blood-oxygen-level-dependent (BOLD) contrast*

We have introduced T_2 decay as the dephasing of precessing spins over time due to spin-spin interactions. The ideal T_2 process occurs in a perfectly homogeneous external magnetic field. In reality, field inhomogeneities accelerate spin dephasing through local variations of precessional frequencies. The true, shorter time-constant is named T_2*. Since most inhomogeneities are static, this effect can be reversed by applying a so-called 'refocusing pulse', which cancels the accumulated phase offsets. However, the pulse programmer can choose to not counteract the inhomogeneity effect and deliberately render an MRI image sensitive to differences in T_2* time. Why would such sensitivity be desirable? One reason is to visualize substances that locally distort the magnetic field, such as the iron atom contained in hemoglobin. In the absence of bound oxygen (deoxyhemoglobin), the iron atom has four unpaired electrons, causing strong magnetic distortion. When oxygen is bound (oxyhemoglobin), the electrons are paired and their effect on the magnetic field is minimized. Therefore, deoxyhemoglobin is paramagnetic, enhancing local magnetic field inhomogeneities and accelerating spin dephasing. Oxyhemoglobin is diamagnetic, with magnetic susceptibility similar to its surroundings. An image made sensitive to T_2* dephasing effects will have lower signal in the presence of deoxyhemoglobin and thus acquire blood-oxygen-level dependent (BOLD) contrast.

The BOLD effect was first described in a seminal paper by Ogawa et al., 1990. The discovery was allegedly made by chance, when the researchers observed dark lines in the cortex of a rat (veins), which disappeared when the animals were provided with pure oxygen. The usefulness of this effect for capturing brain activity across time (fMRI) was quickly realized and multiple teams came up with pulse sequences tailored to that need. These sequences needed to be both sensitive to T_2* effects and fast, in order to capture blood oxygenation changes with reasonable temporal resolution. The most widely used such sequences are based on the echo planar imaging (EPI) approach (Bandettini et al., 1992; Mansfield, 1977), which can achieve very fast scan times. In practice, the entire human brain can be imaged within 1 – 2 seconds, and these limits are being continuously pushed (Moeller et al., 2010; Todd et al., 2016).

1.1.3 *Neurovascular coupling*

BOLD fMRI cannot measure neural activity but instead infers it through the proxy measure of blood oxygenation. The bridge between the two is formed by neurovascular coupling. The human brain has immense metabolic demands, famously consuming 20% of total energy despite being only 2% of the body mass. Since it neither contains large energy stores, nor can it generate energy from fatty acids, the brain relies on a constant supply

of glucose through blood. Perhaps because of these special metabolic constraints, neural tissue has the ability to increase its blood supply on demand. This 'functional hyperemia' does not simply meet the demand. It overcompensates by delivering an excess of oxygen and glucose, and it even persists during hyperglycemia and hyperoxia (Lindauer et al., 2010; Powers et al., 1996; Wolf et al., 1997). Therefore some have proposed alternative roles for functional hyperemia, including heat regulation and waste removal (Yablonskiy et al., 2000). The signaling mechanism mediating the coupling between neurons and blood vessels has been intensively investigated, but the emerging picture is complex. The process likely involves multiple pathways, including direct vascular effects of neuronally-derived substances (e.g. glutamate) as well as indirect cellular mediators—astrocytes and pericytes. The relevant importance of each component remains unclear (Hillman, 2014).

The end result of neurovascular coupling is an increase of both cerebral blood flow (CBF) and volume (CBV). These two factors, together with the cerebral metabolic rate of oxygen ($CMRO_2$), determine the concentration of deoxyhemoglobin and with it, the BOLD signal (Logothetis and Pfeuffer, 2004). During functional hyperemia these three parameters undergo complex interdependent changes, which are hard to disentangle (Buxton and Frank, 1997; Buxton et al., 1998; Grubb et al., 1974). Here we will present a simplified overview of the main phases, according to the so-called 'balloon' model (Buxton et al., 1998). Following neural activity, the BOLD signal starts rising after a delay of about 500 ms and reaches its peak at 3 – 6 s (Hillman, 2014). This is mainly driven by an increase of CBF, which brings oxygen to the active area faster than it can be extracted, and hence, reduces the ratio of deoxyhemoglobin. This inflow of blood causes a passive inflation of the venous 'balloon', and a subsequent increase in CBV. CBV recovers to baseline much slower than CBF, causing an accumulation of deoxyhemoglobin—expressed as a prolonged BOLD signal undershoot that follows the peak. The above shape of the BOLD response can be described in the form of a linear impulse response function—called the hemodynamic response function, or HRF (Glover, 1999). The HRF allows us to simulate the BOLD signal in response to a stimulus, given information about the onset and duration of that stimulus (Figure 1.1).

1.1.4 *Common approaches for experimental design and analysis*

We have seen that the BOLD signal constitutes a highly distorted representation of the original neural activity: its peak occurs with considerable delay, and it can take tens of seconds to return to baseline, even following brief neural events. Moreover, BOLD signal values carry no intrinsic meaning; only their relative change is of interest. This relative change typically equals 1 – 2%, sometimes even less. The above limitations force fMRI researchers to adopt careful experimental designs and sophisticated approaches for data analysis.

The classical fMRI experiment (see Figure 1.1) involves a subject inside an MRI scanner being presented with a stimulus or given a behavioral task ('task-based fMRI'), while the experimenter is acquiring the fMRI dataset—a series of fast T_2*-weighted images using an EPI pulse sequence. The task epochs need to be interspersed with periods of rest, to allow for the BOLD signal to return to baseline. The information about the task timing can be convolved with an HRF to generate a model of the expected BOLD response. The ac-

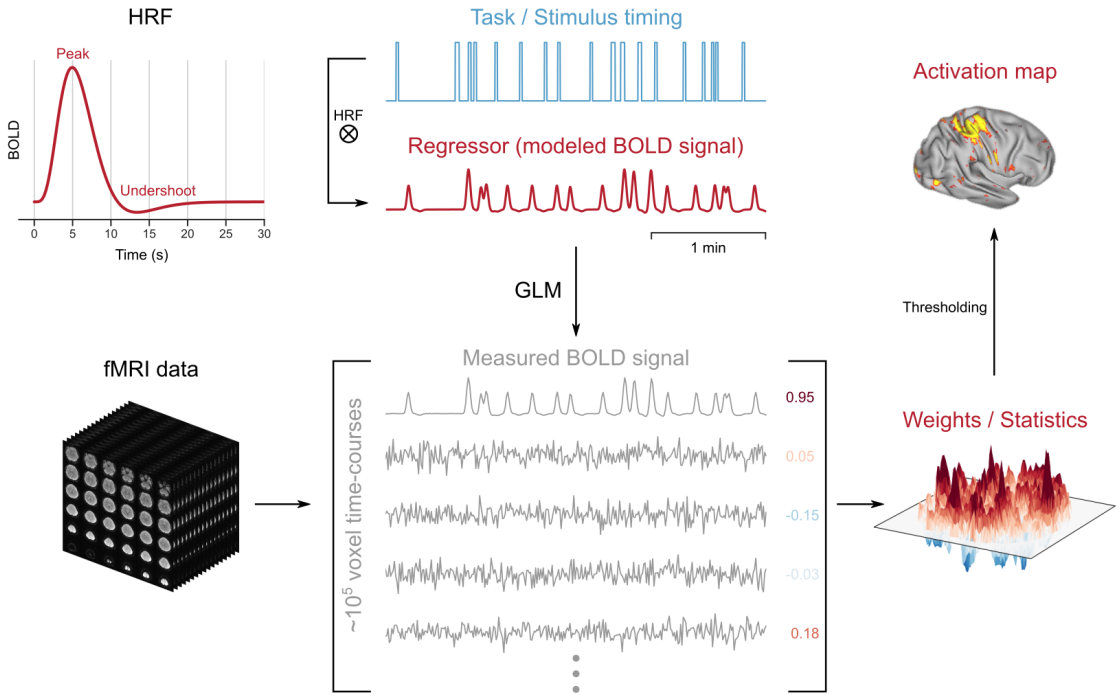

Figure 1.1: Typical fMRI experimental design and analysis. A hemodynamic response function (HRF, top left) shows the temporal evolution of the BOLD response, including a peak and an undershoot. The timing of the behavioral task, or the presented stimulus, is convolved with the HRF to derive a model of the expected BOLD signal. This is used as a regressor in a general linear model (GLM) analysis, whereby it is compared with the measured BOLD time-course of every voxel. Each voxel is assigned a weight representing the regressor's contribution to explaining the variance of the voxel time-course. Activation maps can be generated via appropriate statistical testing and thresholding of the output weights.

quired fMRI dataset typically undergoes multiple preprocessing steps, including motion correction, removal of slow temporal drifts and spatial smoothing (among many others). Every voxel (3D pixel) time-course of the preprocessed dataset is then correlated with the estimated model of the BOLD signal, to locate brain areas exhibiting the expected task-modulated response. This step is typically performed with a mass univariate general linear model (GLM, Bandettini et al., 1993). The GLM uses the expected BOLD response as a reference function ('regressor') and estimates every voxel time-course as a dependent variable. It can incorporate multiple regressors for various tasks and can also include information about nuisance variables (commonly head motion). Every voxel time-course is modeled as a linear combination of the included regressors, each multiplied with an associated weight (beta value) that quantifies the regressor's contribution to the explained variance. Voxels with significant correlation to a given regressor can be identified by running statistical tests on the computed maps of beta values (Worsley, 2001). Since each fMRI dataset contains $\approx 10^5$ voxels, the above approach runs into a massive multiple comparisons problem. Several methods are in use to remedy this problem and derive appropriate significance thresholds (Benjamini and Hochberg, 1995; Smith and Nichols, 2009; Worsley, 2001). Brain areas surviving the thresholding are said to be 'active', i.e. responding to the

task or stimulus. Notice that the above approach also permits the discovery of areas that are anti-correlated with the regressors—exhibiting a so-called negative BOLD response. Voxel time-courses within such areas decrease in response to task epochs. The extent to which the negative BOLD response represents neural inhibition is an area of ongoing research (Moraschi et al., 2012; Mullinger et al., 2014; Pasley et al., 2007; Wade, 2002).

An alternative to task-based fMRI is the so-called 'resting-state' fMRI—sometimes referred to as 'task-free'. fMRI data can be acquired without an associated task or stimulus, capturing spontaneous ongoing brain activity (Biswal et al., 1995; Fox and Raichle, 2007; Raichle, 2011). Here the goal is to identify voxels with highly correlated BOLD signal time-courses, i.e. brain areas that tend to be spontaneously co-active. Areas with covarying activities are said to be 'functionally connected'—a potentially misleading term, since the mere correlation of time-courses does not guarantee the existence of a direct neural connection. There are several approaches for analyzing resting-state fMRI data. The simplest one is to extract the BOLD signal time-course of a predefined region-of-interest, called the seed, and to use it as a regressor for GLM (Biswal et al., 1995). This seed-based correlation approach identifies areas with time-courses similar to the seed. The method can be extended by dividing the brain into parcels and computing the correlation of every parcel pair. The resulting values can be stored in a pair-wise correlation matrix, which can serve as the starting point for additional network-based analyses (Gilson et al., 2019; Mumford et al., 2010; Wang et al., 2010). The prior definition of seeds and parcels constitutes a bias, which can be avoided by adopting a data-driven approach. fMRI data can be decomposed into a set of spatio-temporal components using dimensionality reduction techniques (commonly independent component analysis, ICA) or clustering algorithms (Cordes et al., 2002; Erhardt et al., 2011; Nickerson et al., 2017). These algorithms tend to assign voxels with similar timeseries to the same group or cluster. The combination of all above approaches has led to the discovery that the brain is organized into a set of reproducible functional networks—i.e. groups of brain areas that are preferentially co-active across individuals (Damoiseaux et al., 2006; Power et al., 2011; Yeo et al., 2011). Some are associated with basic sensory and motor activity, while others relate to more domain-general functions—such as attention or cognitive control (Raichle et al., 2001). Alterations in these functional networks have been correlated with neuro-psychiatric diseases (Greicius, 2008).

1.2 FMRI IN EXPERIMENTAL ANIMALS

Perhaps the biggest virtue of fMRI is its capacity to be applied to humans without harm. The non-invasiveness, coupled with the wide availability of clinical MRI scanners, have turned fMRI into a workhorse for human neuroscience (Miller et al., 2016; Van Essen et al., 2013; Van Essen and Ugurbil, 2012). This prompts the question of why we need animal fMRI. Animal experiments have been intertwined with the history of fMRI from the very beginning, as evidenced by the discovery of the BOLD effect in rats (Ogawa et al., 1990). Their continued relevance is attested by the >800 published studies that employ animal fMRI (Mandino et al., 2020). This popularity is driven by the unique suitability of animal fMRI to certain experimental questions. Firstly, fMRI's capacity to be applied to both humans and animals makes it an attractive choice for preclinical translational studies

(Jonckers et al., 2015). Examples include investigation of brain re-organization following peripheral nerve injury and stroke (Dijkhuizen et al., 2001; Pelled et al., 2007). Secondly, animal fMRI is instrumental for studying the physiology of neurovascular coupling and the basis of the BOLD contrast. As discussed above, the purpose and mechanisms of neurovascular coupling are not fully understood, complicating the interpretation of studies that rely on hemodynamic substitutes of neural activity. In animals, the various components of the neurovascular system can be dissected by combining BOLD fMRI with electrophysiological and optical recordings of neural activity. This line of work has led to some landmark studies on the neural correlates of the fMRI signal (Goense and Logothetis, 2008; Logothetis et al., 2001) and continues yielding insights into the functional hemodynamics of the brain (Chen et al., 2019). The expanding capacity of animal fMRI to be combined with genetic, pharmacological, and surgical manipulations, as well as with optical methods for modulating and recording neural activity, has enabled the exploration of increasingly complex neuroscientific questions (Albers et al., 2018; Jonckers et al., 2015; Mandino et al., 2020; Schulz et al., 2012; Schwalm et al., 2017; Wang et al., 2018; Yu et al., 2016).

More than half of all animal fMRI studies are performed on rats (55%), followed by nonhuman primates (23%), and mice (Mandino et al., 2020). The first two are also the ones represented in this thesis. The relative unpopularity of mice might come as a surprise, given the wide availability of mouse disease models and genetic tools. However, mouse fMRI still faces considerable challenges, related to the small brain size—stretching the technical limits of even dedicated small-animal MRI systems—and to the difficulty of maintaining stable physiological conditions (Grandjean et al., 2020; Mandino et al., 2020; Reimann and Niendorf, 2020; Reimann et al., 2018).

Despite the aforementioned promising applications and advances, animal fMRI still faces a key challenge: it necessitates the almost complete immobility of the subject being scanned—achieved through restraint or anesthesia. The first option presents several practical and ethical issues. MRI scanners are tight, dark spaces that become extremely loud during operation. Convincing an animal to stay inside for hours as well as remain fully immobile during data acquisition involves labor-intensive and and time-consuming habituation protocols. Moreover, even trained animals can experience considerable stress, which may not be easy to identify. Apart from this being an ethical issue, stress can also dramatically alter brain function, and thus confound study results (Peeters et al., 2001). Additionally, not all animal species are amenable to habituation. Nonhuman primates can be more readily trained compared to rodents (Liang et al., 2015; Milham et al., 2020; Stenroos et al., 2018), while for some species habituation would be outright impossible.

These difficulties have led most researchers to the second option: anesthetized measurements account for 78% of animal fMRI studies (Mandino et al., 2020). Anesthesia obviously comes with its own set of challenges and pitfalls. It is, by definition, incompatible with behavioral tasks, restricting the available options to stimulus-evoked and resting-state fMRI. 'Resting-state' is not quite the right term, as anesthesia differs radically from waking rest. Anesthetics affect both neural activity and cerebral vasculature, compromising neurovascular coupling (Gao et al., 2017; Masamoto and Kanno, 2012; Pan et al., 2015). They also cause systemic changes in cardiovascular and respiratory physiology. Therefore, fMRI studies in anesthetized animals are challenging to perform, analyze,

and interpret. Nevertheless, researchers have sought to strike a compromise by optimizing the anesthetic regimens they employ. The ideal anesthetic protocol for animal fMRI has to ensure sufficient sedation and immobility, while maintaining stable physiology. It must also preserve some degree of specific neural activity and neurovascular coupling.

The four anesthetics used by the vast majority of animal fMRI studies are isoflurane, medetomidine, α-chloralose, and urethane (Mandino et al., 2020). The first two appear throughout this thesis and will be introduced below in detail. The other two—α-chloralose and urethane—have become less common over the years, mainly due to their toxicity. Historically, α-chloralose has been a popular choice for neurovascular coupling experiments, because early studies had shown that it preserves hemodynamic and metabolic responses to sensory stimulation (Ueki et al., 1988). However, its use is impractical, due to low solubility, slow pharmacokinetics, and the need for both mechanical ventilation and intravenous catheterization. Its repeated administration also leads to hepatic and renal damage (Silverman and Muir, 1993). Urethane can only be used for terminal experiments and is thus not suited for longitudinal study designs.

1.2.1 *Medetomidine*

Medetomidine is a highly potent and selective α_2-adrenergic receptor agonist (α_2:α_1 binding ratio of 1620:1). It constitutes an equal racemic mixture of two stereoisomers: levo- and dextro-medetomidine. The latter, referred to as dexmedetomidine, is the active component and can induce effects identical to medetomidine at half the dose. Medetomidine's desirable effects include sedation, moderate analgesia, muscle relaxation and anxiolysis. It can enhance the potency of other anesthetics and thus reduce their dosing requirements. This property is referred to as the 'anesthetic sparing effect' and makes medetomidine useful in combination with other drugs. The sedative effects of medetomidine are believed to be mediated by its actions on arousal pathways. The highest concentration of α_2-adrenergic receptors in the brain is found in the locus coeruleus—a noradrenergic center that promotes wakefulness by disinhibiting the ascending arousal system. Dexmedetomidine binds to presynaptic α_2-adrenergic receptors of locus coeruleus neurons and causes their hyperpolarization. This reduces the opening probability of presynaptic calcium channels and ultimately suppresses noradrenaline release. The end result is sleep-like sedation, mimicking non-rapid-eye-movement sleep. Subjects sedated with medetomidine remain readily arousable by noxious stimuli (Bol et al., 1997, 1999; Lukasik and Gillies, 2003; Sinclair, 2003).

Medetomidine exerts strong cardiovascular effects. The reduced noradrenergic outflow within the central nervous system dampens the sympathetic tone, and thus the heart rate. Direct effects on peripheral α_2-adrenergic receptors lead to elevated vascular tone and resistance, thereby increasing blood pressure. The hypertension induces physiological reflex bradycardia and leads to a further decrease of heart rate. High doses of medetomidine may lead to dangerous bradyarrhythmias. Fortunately, these can be rapidly reversed by competitive α_2-antagonists, the most specific of which is atipamezole. The administration of atipamezole can antagonize the effects of medetomidine within 3–7 minutes, facilitating swift recovery from anesthesia. Medetomidine's effects on breathing are minor. When

administered alone, medetomidine carries no risk of respiratory depression (Bol et al., 1997, 1999; Sinclair, 2003).

Weber et al., 2006 introduced a novel medetomidine-based regimen for longitudinal fMRI studies in rats. The protocol included an initial bolus dose of medetomidine, followed up by its continuous s.c. infusion starting 15 min later. This regimen presented several advantages for fMRI studies: sedation lasting for several hours, easy subcutaneous administration, no need for intubation, no toxicity, and most importantly, robust stimulus-evoked BOLD responses (Weber et al., 2006). Other research groups have since confirmed these benefits and expanded the protocol's applications to resting-state fMRI studies (Kalthoff et al., 2013; Pawela et al., 2009; Williams et al., 2010; Zhao et al., 2008). Medetomidine-based anesthetic regimens have now become an established practice for rat fMRI and have also been used in other species. However, several concerns remain regarding the duration and stability of medetomidine anesthesia and there is yet no consensus on the precise administration scheme. In Chapter 2, we tried to address some of these concerns and aimed to advance the standardization of medetomidine administration protocols for rat fMRI experiments.

1.2.2 *Isoflurane*

Isoflurane is an inhalable agent that belongs to the class of halogenated volatile anesthetics, alongside similar compounds like sevoflurane, desflurane, and enflurane. These agents undergo very little biotransformation and can be completely eliminated by exhaling air. Therefore, they permit very rapid induction and recovery of anesthesia. Their dosage—expressed as the percentage of anesthetic vapor in the inhaled gas mixture—can be precisely controlled and adjusted to the needs of the procedure being performed. In contrast to injectable anesthetics, a stable depth can be maintained throughout the anesthetic episode. Owing to these properties, halogenated agents form an integral part of general anesthesia in clinical practice. They are also often employed in veterinary medicine and animal research, with isoflurane being the most widely used member of the family (Flecknell, 2015).

Isoflurane exerts dose-dependent effects on the cardiovascular and respiratory systems. At high doses it leads to hypotension and respiratory depression. Therefore isoflurane is commonly combined with intubation and mechanical ventilation. At lower doses it can be administered via facial masks (nose cones in rodents) and allow for spontaneous breathing (Flecknell, 2015). In the brain, isoflurane acts on almost all major receptors, suppressing excitatory synaptic transmission and enhancing γ-aminobutyric acid type A ($GABA_A$) receptor activity (Franks, 2008; Hemmings, 2009; Rudolph and Antkowiak, 2004). It also dose-dependently dilates cerebral blood vessels via altering calcium currents in smooth muscle cells (Flynn et al., 1992; Iida et al., 1998). The resulting increase in baseline CBF can limit the magnitude of stimulus-evoked hemodynamic responses and is thought to underly a dose-dependent suppression of BOLD responses (Masamoto et al., 2009, 2007). In rats anesthetized with isoflurane, BOLD responses were reported to be unstable at 1.0–1.3 % and undetectable at 1.5% (Chao et al., 2014). Nevertheless, low doses of isoflurane have been proposed as a viable alternative for longitudinal fMRI studies (Masamoto et al., 2007; Sommers et al., 2009). Others have suggested to combine an extremely low

dose of isoflurane with the continuous infusion of medetomidine (Brynildsen et al., 2017). The combination takes advantage of the anesthetic sparing effects of medetomidine and also balances the opposing actions of the two drugs on the vascular system (vasodilation by isoflurane, vasoconstriction by medetomidine). This approach has been successfully used for fMRI in rats (Brynildsen et al., 2017) and nonhuman primates (Milham et al., 2020). However, medetomidine enhances the depressive effect of isoflurane on respiration (Sinclair, 2003), and maintaining robust BOLD responses may necessitate mechanical ventilation (van Alst et al., 2019).

Task-free fMRI studies in isoflurane-anesthetized animals have led to some interesting observations: researchers have reported a global synchronization of BOLD signal time-courses across the entire cortex (Kalthoff et al., 2013; Liu et al., 2013; Paasonen et al., 2018). As we will demonstrate in Chapter 3, this global synchronization is a manifestation of burst-suppression—a neural activity pattern in which bursts of slow waves alternate with periods of electrical silence (Kroeger et al., 2013). In that study we identified the precise fMRI correlates of burst-suppression and mapped the spatial distribution of this neural activity pattern across the brains of multiple primate and rodent species.

1.3 OPTICAL METHODS

Our fMRI study of burst-suppression (Chapter 3) led to interesting findings but also raised questions that cannot be addressed by fMRI alone. We therefore turned to optical methods, which relate to neural activity more directly and can achieve faster temporal resolution. For reasons explained in Chapter 4, we opted for *in vivo* two-photon calcium imaging. The following paragraphs will introduce this method in brief.

1.3.1 *Neuronal calcium imaging*

Calcium ions constitute versatile signals in all cell types. In neurons, they adopt multiple specialized roles that are tightly coupled with neuronal morphology and function. They operate across temporal and spatial scales, and in different sub-cellular compartments (Grienberger and Konnerth, 2012). In presynaptic terminals they trigger the release of neurotransmitters (Neher and Sakaba, 2008); in postsynaptic dendritic spines they mediate synaptic plasticity (Zucker, 1999); in the nucleus they can regulate gene transcription depending on neuronal activity (Lyons and West, 2011). Therefore, the imaging of calcium can provide insight into all aspects of neuronal function. The intracellular calcium concentration, which is normally several orders of magnitude smaller than the extracellular one, can rapidly increase through influx from multiple channels. The most important contributors are voltage-gated calcium channels, ionotropic glutamate receptors, nicotinic acetylcholine receptors, and transient receptor potential type C channels. Calcium can also be released from the endoplasmic reticulum, mediated by inositol triphosphate and ryanodine receptors. In this thesis we focus on calcium signals in the neuronal soma, which reflect spiking activity. The main source of somatic calcium is the action potential-induced opening of voltage-gated calcium channels (Grienberger and Konnerth, 2012).

Two main classes of molecules are being used to visualize calcium in neurons: chemical calcium dyes and genetically-encoded calcium indicators (GECIs). The latter type, chiefly

represented by the GCaMP family, has become increasingly popular for *in vivo* applications (Grienberger and Konnerth, 2012). GCaMP consists of a circularly permuted enhanced green fluorescent protein, alongside the calcium-binding protein calmodulin and the calmodulin-binding peptide M13. When calcium is present, conformational changes through calmodulin-M13 interactions lead to an increase in emitted fluorescence (Nakai et al., 2001). Since their introduction, GCaMP proteins have undergone several improvements through genetic engineering, leading to ever-increasing signal-to-noise ratio, response kinetics, and dynamic range (Chen et al., 2013; Dana et al., 2019). Meanwhile, researchers have also introduced GECIs with red-shifted excitation and emission spectra. Red light can penetrate deeper into brain tissue and may lead to less phototoxicity (Dana et al., 2016).

GECIs are most commonly expressed in target cell populations via viral transduction or by generating transgenic mouse lines. Viral transduction involves stereotaxically injecting the viral construct into target brain areas. Most constructs are based on the backbones of either lentiviruses (LV) or adeno-associated viruses (AAV). Expression in specific cell types can be achieved through viral tropisms and cell-type-specific gene promoters. In transgenic mouse lines, cell-specificity is commonly conferred through Cre recombinase driver lines (Grienberger and Konnerth, 2012).

1.3.2 *Two-photon microscopy*

In two-photon microscopy, two low-energy near-infrared photons may jointly excite a fluorescent molecule from its ground state. This effect occurs only when the two photons arrive at their target within a femtosecond time-window (Denk et al., 1990). The rate of two-photon absorption increases with the square of light intensity. This implies that fluorophores can be almost exclusively excited within a tiny focal volume, minimizing out-of-focus excitation and bleaching (Denk et al., 1990). Another useful attribute is that infrared light can achieve much deeper tissue penetration than visible light. Due to all these properties, two-photon microscopy has become one of the most widely used methods for imaging the emitted fluorescence of calcium indicators, especially when deep tissue penetration is desired (Helmchen and Denk, 2005; Svoboda and Yasuda, 2006). The combination of recent advances in GECIs and two-photon microscopy have enabled incredible feats in modern neuroscience, such as the simultaneous recording of >10.000 neurons in the visual cortex of awake behaving mice (Pachitariu et al., 2017; Stringer et al., 2019). This laser-powered technology is not yet at the level of the fictional laser-encephalogram, but it represents a step in that direction.

1.4 STUDY SUMMARIES

1.4.1 *Study A: Chapter 2*

Temporal stability of fMRI measurements in medetomidine-anesthetized rats. This study builds upon work done for my Master's project, during which I had developed the required setup for performing fMRI in rats and had acquired the first proof-of-principle fMRI data using medetomidine anesthesia. During my PhD, we aimed to optimize the protocol for

medetomidine administration in a way that would lead to long-lasting imaging sessions, stable physiology, and reproducible BOLD fMRI measures of stimulus-evoked and task-free activity. We surveyed the literature for commonly used administration protocols and discovered a lack of consensus with regards to recommended timing, dose, and route of administration. Therefore, we set out to systematically evaluate four administration protocols that varied with regards to the aforementioned parameters. We anesthetized rats for long periods of time and assessed the achieved duration of anesthesia, as well as aspects of cardiovascular and respiratory physiology. Throughout the anesthetic episodes, we repeatedly evaluated somatosensory stimulus-evoked BOLD responses and fMRI measures of task-free functional connectivity. The results confirmed that medetomidine is a suitable choice for rat fMRI experiments. Anesthesia duration exceeded five hours in most sessions, heart and respiratory rates were mostly stable after the first hour of anesthesia, and the majority of performed fMRI experiments led to a significant and selective activation of the expected brain areas. However, both stimulus-evoked activity and task-free functional connectivity exhibited varying temporal trends depending on the protocol of medetomidine administration. Intravenous administration of a medetomidine bolus (0.05 mg/kg), combined with a subsequent continuous infusion (0.1 mg/kg/h), led to temporally stable measures of stimulus-evoked activity and functional connectivity throughout the anesthesia. Deviating from the above protocol—by omitting the bolus, lowering the medetomidine dose, or using the subcutaneous route—compromised the stability of these measures in the initial two-hour period. We concluded that both an appropriate protocol of medetomidine administration and a suitable timing of fMRI experiments are crucial for obtaining consistent results. We hope that these factors will be considered for the design and interpretation of future rat fMRI studies, in the interest of increasing standardization within the field. This study has been already published (Sirmpilatze et al., 2019) and the reprint is attached in Chapter 2. We have also made all the raw data publicly available at https://openneuro.org/datasets/ds001981/.

1.4.2 *Study B: Chapter 3*

Brains areas involved in anesthesia-induced burst-suppression differ significantly between primates and rodents. This study was motivated by puzzling reports about the effects of isoflurane anesthesia on fMRI measures of functional connectivity. Specifically, animals anesthetized with isoflurane exhibit widespread synchronization of BOLD signal time-courses across multiple brain areas—an effect we had also reproduced in pilot experiments. Several researchers have proposed that this effect may be attributed to burst-suppression activity, which is induced by moderate-to-high doses of isoflurane. Burst-suppression is an electroencephalographic (EEG) pattern that consists of high amplitude slow waves, quasi-periodically interrupted by periods of electrical quiescence. Apart from isoflurane, burst-suppression also appears with many other anesthetics, in comatose states of various etiologies, and in some metabolic encephalopathies. However, the spatial properties of bursts are still unexplored: where they originate, how they propagate and which brain areas they cover. We could identify the brain areas engaged in burst-suppression through the reported synchronizing effect on BOLD fMRI time-courses. Therefore, we used already existing animal fMRI data to address a relevant question about burst-suppression. We

first developed a systematic way of assessing whether burst-suppression was present in any given fMRI recording, using an existing EEG-fMRI dataset acquired in human participants during sevoflurane anesthesia. We found that burst-suppression could be reliably detected based on its fMRI pattern alone, using a simple heuristic algorithm. We then applied this algorithm to animal fMRI datasets from multiple species—long-tailed macaques, marmosets, and rats, and identified instances of isoflurane-induced burst-suppression. We subsequently used these instances to map the extent of burst-suppression in each animal species. We discovered an unexpected but robust difference between primates and rodents: in rats the entire neocortex engaged in burst-suppression, while in primates certain cortical areas were excluded—most notably the primary visual cortex. We discussed several possible mechanisms but concluded that addressing the cause of this difference would necessitate direct recordings of neural activity in the visual cortex of both primates and rodents. This study has been prepared for submission to a journal and is provided in Chapter 3 in the form of a research article.

1.4.3 *Study C: Chapter 4*

In vivo two-photon calcium imaging of the rat cortex during isoflurane-induced burst-suppression. This study was motivated by the results of Study B and the identified need for direct recordings of neural activity in the visual cortex during burst-suppression. We decided to approach this goal by establishing a working method for *in vivo* two-photon calcium imaging in isoflurane-anesthetized animals. This study comprises a series of pilot experiments in rats, through which we developed and tested the various components required by this method. We evaluated several viral constructs for expressing genetically-encoded calcium indicators in somatosensory and visual areas. We also developed the surgical expertise for implanting chronically stable cranial windows and fiber-optic cannulas in the rat cortex. In two animals, we successfully recorded from hundreds of layer 2/3 neurons across multiple imaging sessions, for up to 3 months. These recordings captured burst-suppression activity across a range of isoflurane doses in both the somatosensory and the visual cortex. We were also able to evoke bursts through flashes of light and electrical stimulation of the forepaw. These preliminary data were in line with our previous fMRI findings about the pancortical distribution of burst-suppression in rats and reproduced several known properties of burst-suppression based on the existing rodent literature. In conclusion, we have demonstrated the feasibility of longitudinal *in vivo* two-photon calcium imaging in isoflurane-anesthetized rats. The developed expertise and the acquired data will enable us to design hypothesis-driven studies of burst-suppression in both rats and marmosets, to ultimately address the question raised by the results of Chapter 3.

2

TEMPORAL STABILITY OF FMRI MEASUREMENTS IN MEDETOMIDINE-ANESTHETIZED RATS.

AUTHORS

Nikoloz Sirmpilatze[1,2,3,4], Jürgen Baudewig[1], and Susann Boretius[1,2,3,4].

1. Functional Imaging Laboratory, German Primate Center—Leibniz Institute for Primate Research, Göttingen, Germany
2. Georg-August University of Göttingen, Göttingen, Germany
3. International Max Planck Research School for Neurosciences, Göttingen, Germany
4. DFG Research Center for Nanoscale Microscopy and Molecular Physiology of the Brain (CNMPB), Göttingen, Germany

OWN CONTRIBUTIONS

- Data collection
- Data analysis
- Data interpretation (together with JB and SB)
- Data visualization
- Writing of original draft
- Editing (together with JB and SB)

SCIENTIFIC REPORTS
nature research

OPEN

Temporal stability of fMRI in medetomidine-anesthetized rats

Nikoloz Sirmpilatze[1,2,3,4*], Jürgen Baudewig[1] & Susann Boretius[1,2,3,4*]

Medetomidine has become a popular choice for anesthetizing rats during long-lasting sessions of blood-oxygen-level dependent (BOLD) functional magnetic resonance imaging (fMRI). Despite this, it has not yet been thoroughly established how commonly reported fMRI readouts evolve over several hours of medetomidine anesthesia and how they are affected by the precise timing, dose, and route of administration. We used four different protocols of medetomidine administration to anesthetize rats for up to six hours and repeatedly evaluated somatosensory stimulus-evoked BOLD responses and resting state functional connectivity. We found that the temporal evolution of fMRI readouts strongly depended on the method of administration. Intravenous administration of a medetomidine bolus (0.05 mg/kg), combined with a subsequent continuous infusion (0.1 mg/kg/h), led to temporally stable measures of stimulus-evoked activity and functional connectivity throughout the anesthesia. Deviating from the above protocol—by omitting the bolus, lowering the medetomidine dose, or using the subcutaneous route—compromised the stability of these measures in the initial two-hour period. We conclude that both an appropriate protocol of medetomidine administration and a suitable timing of fMRI experiments are crucial for obtaining consistent results. These factors should be considered for the design and interpretation of future rat fMRI studies.

Functional magnetic resonance imaging (fMRI), relying on blood-oxygen-level dependent (BOLD) contrast[1], is being widely used for the non-invasive mapping of human brain function. Classically, fMRI has focused on the brain's response to a task or stimulus, but more recent task-free (resting state fMRI) approaches have explored spontaneous low frequency fluctuations in the BOLD signal[2,3], and their role in the functional connectivity of healthy and diseased brains[4]. Since the advent of dedicated high-field MR systems, fMRI applications have expanded to experimental animals, especially rodents[5]. This is a promising development for translational preclinical research, since the same technique can be applied to both human patients and animal models. Additionally, the expanding capacity of small animal fMRI to be combined with genetic, pharmacological and surgical manipulations, as well as with electrophysiological and optical recordings, allows the exploration of increasingly complex neuroscientific questions[6–9].

Nevertheless, small animal fMRI poses a methodological challenge: it necessitates the subject's immobility for long imaging times. Animals can be restrained and habituated to head fixation and MR scanner noise, but this is laborious for the researcher, and often stressful for the animal[10–12]. Thus, ethical and practical considerations mandate the use of anesthesia in the majority of small animal fMRI studies. Unfortunately, anesthetics confound fMRI measurements in multiple ways: they may alter neural activity, affect systemic cardiorespiratory physiology, and interfere with cerebral vasculature and neurovascular coupling—the very mechanism giving rise to the BOLD contrast[13,14]. Therefore, there is a need for an anesthetic protocol that ideally provides sufficient, long-lasting sedation, while maintaining neural activity and neurovascular coupling. In pursuit of the above properties, researchers have tried multiple anesthetic agents, including α-chloralose, medetomidine, isoflurane, propofol, urethane, and ketamine-xylazine. These agents have varying effects on the neurovascular system, with each of them presenting a unique set of benefits and drawbacks for fMRI applications[12–18]. This has led to a substantial diversity in anesthetic protocols used for rodent fMRI, compromising the comparability and reproducibility of results.

Of the above anesthetics, the sedative agent medetomidine—a highly selective α_2-adrenergic agonist—holds perhaps the most promise for becoming a routine choice for fMRI applications in rats. Medetomidine comes as an equal mixture of two enantiomers, with the dextro-isomer, dexmedetomidine, being the active component[19,20]. Dexmedetomidine decreases the activity of noradrenergic neurons in the locus coeruleus, producing a state that

[1]Functional Imaging Laboratory, German Primate Center - Leibniz Institute for Primate Research, Göttingen, Germany. [2]Georg-August University of Göttingen, Göttingen, Germany. [3]International Max Planck Research School for Neurosciences, Göttingen, Germany. [4]DFG Research Center for Nanoscale Microscopy and Molecular Physiology of the Brain (CNMPB), Göttingen, Germany. *email: NSirmpilatze@dpz.eu; SBoretius@dpz.eu

	Name	Route	Bolus	Bolus dose (mg/kg)	Infusion rate (mg/kg/h)
1	SC with bolus	SC	yes	0.05	0.1
2	IV with bolus	IV	yes	0.05	0.1
3	IV no bolus	IV	no	—	0.1
4	IV lower dose	IV	yes	0.035	0.07

Table 1. Medetomidine administration protocols used in this study. SC: subcutaneous; IV: intravenous.

mimics non-REM sleep[21]. Conveniently, the drug's effects are reversible by a specific α_2-adrenergic antagonist—atipamezole[19,20]. A protocol based on the continuous infusion of medetomidine, first introduced by Weber *et al.*[22], presents several advantages for fMRI studies: it sedates rats for several hours, leads to robust stimulus-evoked BOLD responses, allows for easy subcutaneous (SC) administration, avoids the need for intubation, and can be used for longitudinal studies with multiple fMRI sessions[23]. Other research groups have since confirmed the benefits of medetomidine infusion and expanded its usage to resting state fMRI[24–27]. Medetomidine anesthesia is currently an established practice for rat fMRI, with at least 40 published articles reporting the use of the original medetomidine protocol, or variations of it (Supplementary Table S1). Its use is expected to rise, owing to the practical advantages and to the increasing availability of techniques that can be combined with rat fMRI.

However, there are several concerns revolving around the duration and stability of medetomidine anesthesia. Medetomidine administration is always preceded by an inhalable gas anesthetic, usually isoflurane, which is used for anesthesia induction and animal preparation. Isoflurane alters brain metabolism[28], strongly suppresses stimulus-evoked hemodynamic responses[29–31], and may introduce widespread correlations in functional connectivity metrics[12,27,32]. The possibility of these effects lingering long after isoflurane discontinuation cannot be excluded[33]. Then there is the issue of medetomidine itself, which is usually given in two steps: first as a bolus loading dose and then as a continuous infusion. The drug exerts strong effects on cardio-respiratory physiology, including severe bradycardia, peripheral vasoconstriction, transient hypertension, hypoxia and hypocapnia[20,23]. Since these parameters are expected to influence the BOLD mechanism, time-varying effects on physiology could translate into unstable BOLD-based readouts. Another important concern is the restricted duration of anesthesia, with animals reported to spontaneously wake up despite the continuous infusion of medetomidine. Tolerance to the drug's sedative effects has been blamed for this, with researchers proposing to counter it by stepping up the infusion rate[25]. All the above issues are further compounded by the lack of consensus regarding the exact administration scheme; protocols vary in administration route and dose, while some researchers choose to omit the bolus (see Supplementary Table S1).

These concerns imply that commonly reported fMRI readouts, namely stimulus-evoked BOLD responses and resting state functional connectivity (RSFC), might not be stable over long-lasting imaging sessions. It is unclear when a steady state is reached by these readouts, for how long it is maintained, and how it is affected by various medetomidine administration choices. An answer to these questions would enable researchers to design rat fMRI experiments in a way that maximizes the duration of the steady state. This would increase the available experimental time, decrease variance, and ultimately reduce the total number of required animals, all the while promoting comparability among studies.

To achieve the above goals, we examined how stimulus-evoked BOLD responses and RSFC evolve over time during medetomidine anesthesia. We tested four different protocols for medetomidine administration (Table 1, Fig. 1a) on two separate sessions: first on a laboratory bench and then inside a small animal MR-system. During the latter session, we performed multiple repeated fMRI measurements (runs), with consecutive runs being alternated between somatosensory stimulus-evoked fMRI with electrical forepaw stimulation (EFS-fMRI) and resting state fMRI (RS-fMRI) (see Fig. 1b,c). The acquired runs, 283 EFS-fMRI and 295 RS-fMRI in total, spanned a period of 0.5–6 hours relative to the start of medetomidine administration. For each medetomidine protocol, we report the achieved duration of anesthesia and the following measures across time: heart and respiratory rates (HR and RR); localization and amplitude of stimulus-evoked responses; strength and structure of RSFC. Based on our findings, we make recommendations regarding the administration protocol of medetomidine and the timing of fMRI experiments within the protocol.

Results

Anesthesia duration and physiology. Out of all 48 anesthesia sessions, 27 lasted for the full six hours, while 21 ended with a spontaneous wake-up (spontaneous movement for bench sessions; rapid rise in RR for fMRI sessions). These wake-up incidents occurred across session types (8/24 bench; 13/24 fMRI) and medetomidine protocols (4, 6, 7, and 4 out of 12, for protocols 1–4 respectively). However, only a few of those occurred early, with 35/48 sessions (72.9%) exceeding five hours in duration (Fig. 2a). The HR and RR followed similar temporal trends across all four medetomidine protocols (Fig. 2b). HR decreased rapidly after the introduction of medetomidine, dropping by approximately 50% within the first hour of anesthesia. After that it showed only a slight tendency to gradually recover over time. The RR also underwent rapid changes in the first hour: it started at 40–70 bpm under isoflurane, decreased in response to medetomidine introduction, and gradually recovered following the discontinuation of isoflurane. As was the case with HR, it remained mostly stable after the first hour. HR and RR traces for individual anesthesia sessions can be found in Supplementary Figs S3 and S4 respectively.

Areas activated by the stimulus. For each EFS-fMRI run we identified the active areas using a first-level general linear model analysis. The thresholded statistical maps (cluster threshold, $z > 3.1$, $p = 0.05$) were binarized

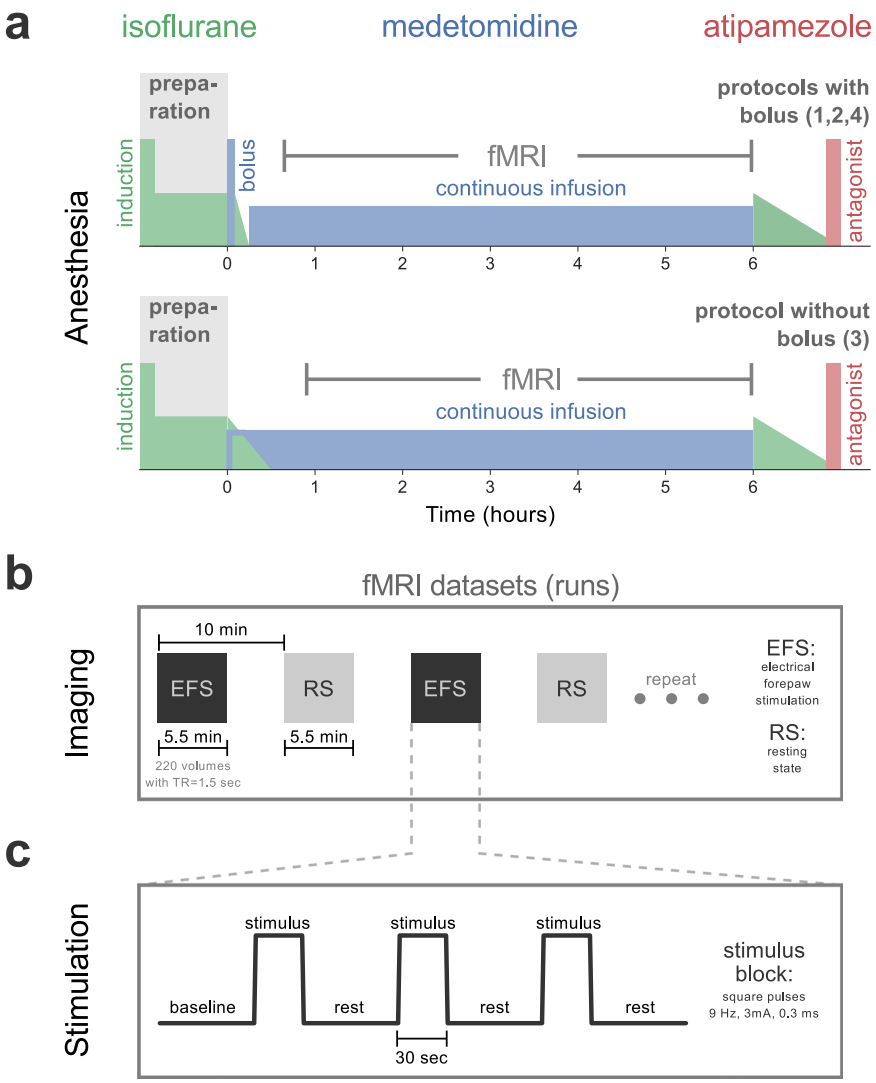

Figure 1. Anesthetic protocols and fMRI acquisition. **(a)** The general outline of the applied anesthetic protocols. For all four protocols (see Table 1), isoflurane was used to induce unconsciousness (5%) and during animal preparation (2–3%). For protocols 1, 2, and 4, a bolus of medetomidine was given after the preparation phase, followed by a gradual reduction of isoflurane and its eventual discontinuation 10 min later; continuous infusion of medetomidine commenced 15 min after the bolus. The bolus was omitted for protocol 3, with continuous infusion starting directly after preparation, and isoflurane being gradually reduced to zero over the course of 20–25 min. Anesthesia was maintained for a maximum of six hours since the start of medetomidine administration (time = 0). In the end, animals were provided with 2% isoflurane and freed from all equipment. Atipamezole was injected SC to antagonize medetomidine effects and to facilitate a smooth recovery. **(b)** Multiple fMRI runs were acquired per anesthesia session, with consecutive runs being alternated between somatosensory fMRI with electrical forepaw stimulation (EFS-fMRI) and resting state fMRI (RS-fMRI) with no stimulus. The stimulation paradigm applied during EFS-fMRI runs is shown in **(c)**.

(1 for active voxels, 0 elsewhere) and averaged across all EFS-fMRI runs to produce an activation probability map. The probability map revealed a consistently active cluster, anatomically corresponding to the left (contralateral to the stimulus) forelimb region of the primary somatosensory cortex—abbreviated as S1FL (Fig. 3a1). This cluster's center was active in 85.16% of all EFS-fMRI runs, whereas no other area was active in more than 7% of runs. To ensure that there was no systematic shift in the location of the active S1FL cluster, the 283 first-level activation maps were split into 12 groups according to the applied medetomidine protocol and the time-window since the start of medetomidine administration (early: 0–2 h; middle: 2–4 h; late: 4–6 h). Examination of activation probability maps from all groups (Fig. 3a2) verified that the active cluster's location remained stable across time and medetomidine protocols.

Shape and strength of stimulus-evoked responses. The portion of the S1FL that was significantly active in at least 30% of all 283 EFS-fMRI runs was taken as a functionally-defined region-of-interest (ROI). For each EFS-fMRI run, this ROI's mean BOLD time course was extracted, normalized to the pre-stimulus baseline,

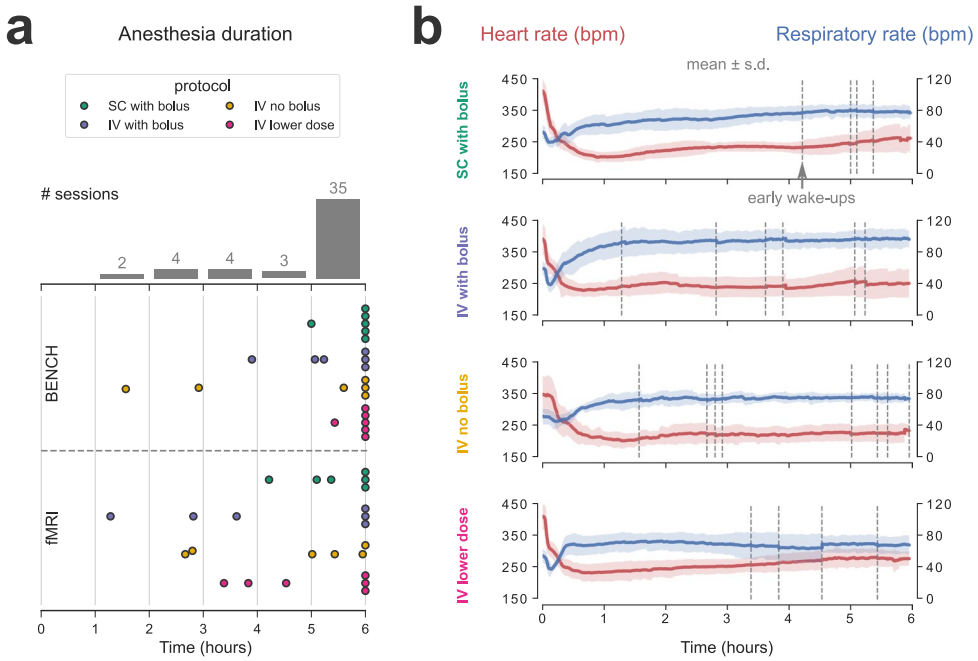

Figure 2. Anesthesia duration and physiology. **(a)** Anesthesia duration is plotted (dots) separately for bench and fMRI sessions, across all four medetomidine protocols. The bars represent a histogram of anesthesia durations, with all 48 anesthesia sessions binned into one-hour intervals. **(b)** Heart and respiratory rates (in beats/breaths per minute—bpm), pooled from both bench and fMRI sessions of each medetomidine protocol, are plotted as an across-session mean (solid line) ± s.d. (shaded area). Each of the four medetomidine protocol groups consists of twelve sessions—six animals with two sessions each. The time-points of early wake-ups are indicated with vertical dashed lines. Heart and respiratory rate traces for individual sessions can be found in Supplementary Figs S3 and S4 respectively.

and averaged across stimulation blocks to produce an event-related average. This was used to extract the peak % signal change (peak ΔBOLD), as a measure of stimulus-evoked BOLD response strength (Fig. 3b). The examination of event-related averages revealed that the shape of S1FL BOLD responses was very similar across the four medetomidine protocols (Fig. 3c). The signal exhibited a sharp peak about 3 s after stimulus onset, followed by a plateau lasting till the end of the 30 s stimulation.

We tested the dependence of peak ΔBOLD on time (early, middle and late two-hour-long time-windows), medetomidine protocol, and their interaction. The medetomidine protocol alone had no effect (ANOVA: $F = 1.01$, $p = 0.38$), but we found a strong time dependence ($F = 37.65$, $p < 0.001$) and a significant interaction between medetomidine protocol and time-window ($F = 4.35$, $p < 0.001$). Post-hoc pair-wise t-tests with p-value adjustment for multiple comparisons (Holm method) revealed varying temporal trends depending on the medetomidine protocol (Fig. 4a,b). Protocol 2 (IV with bolus) led to temporally stable BOLD responses (mean peak ΔBOLD of about 2.3% across time-windows), while the other three protocols led to a significant decrease in response strength between the early and the middle time-windows. Despite their differing temporal trends, all four protocols converged to a mean peak ΔBOLD of 2–3% after the initial two hours of medetomidine anesthesia (Fig. 4c). The results of all statistical comparisons can be found in Supplementary Tables S9–S11.

Resting state functional connectivity. RSFC was probed by examining the pair-wise correlations between the BOLD time courses of 28 anatomically defined ROIs (Fig. 5a). Examination of the pair-wise correlation matrices (Fig. 5b1), and of their network representations (Fig. 5c), showed that the hierarchical structure of the network, i.e. the strength of individual connections relative to each other, was consistent over time for all medetomidine protocols. The network's global RSFC—the mean correlation (Fisher's Z-score) across all unique ROI pairs—was computed for all RS-fMRI runs, and tested for its dependence on time (early, middle and late time-windows), medetomidine protocol, and their interaction. All three factors were found to have a significant effect on global RSFC, according to the results of ANOVA (medetomidine protocol: $F = 7.24$, $p = 0.001$; time-window: $F = 5.15$, $p = 0.006$; protocol-time interaction: $F = 3.41$, $p = 0.003$). Post-hoc pair-wise t-tests followed with p-value adjustment for multiple comparisons (Holm method). Bolus-based medetomidine administration (protocols 1, 2 and 4) was found to sustain stable global RSFC throughout the three time-windows. Omitting the bolus (protocol 3, IV no bolus) led to global RSFC values that were stronger in the early period ($p = 0.002$ compared to protocol 2; $p < 0.001$ compared to protocol 4) but decreased significantly between the early and the middle time-windows ($p = 0.017$). The results of all statistical comparisons can be found in Supplementary Tables S9,S10,S12.

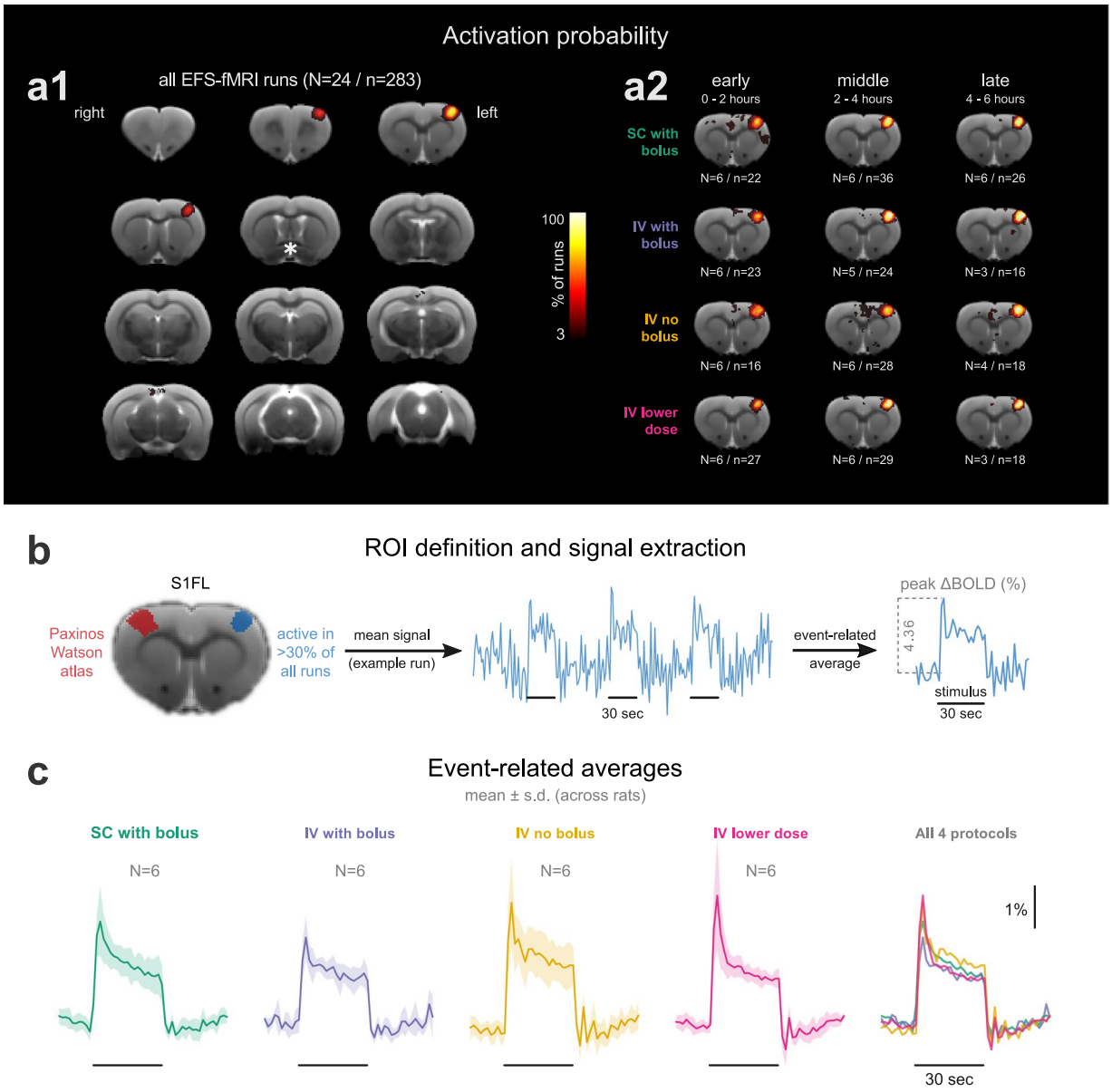

Figure 3. Areas activated by electrical forepaw stimulation (EFS). **(a1)** An activation probability map produced by pooling significantly active clusters from first-level analyses of 283 EFS-fMRI runs. The asterisk marks the crossing of the anterior commissure (AC, −0.36 mm relative to the bregma, according to the Paxinos-Watson rat brain atlas). The rest of the slices are taken at 1 mm intervals from the AC slice. In **(a2)**, the EFS-fMRI runs are grouped according to the applied medetomidine protocol and to the time-window since the start of medetomidine administration (early: 0–2 h; middle: 2–4 h; late: 4–6 h), to produce separate activation probability maps for each group. Only the slice containing the peak activation, 2 mm rostral to AC, is shown for each group. All maps in **(a1,a2)** are thresholded at 3% and overlaid on a T2-weighted structural study template. **(b)** The only consistently active cluster across all runs corresponds to the forelimb region of the left primary somatosensory cortex (S1FL). The location of this cluster is shown alongside the anatomical delineation of the same area from the Paxinos-Watson rat brain atlas. The functionally defined S1FL (area active in >30% of all EFS-fMRI runs) is set as a region-of-interest (ROI) for the extraction of BOLD signal time courses. Such a time course is shown for one example EFS-fMRI run, with the stimulation blocks marked by horizontal lines. Averaging the three stimulation blocks results in an event-related average, from which the peak % signal change (peak ΔBOLD) can be extracted. Event-related average responses (mean ± s.d. across rats) are plotted for all four medetomidine protocols **(c)**. N: number of rats; n: number of fMRI runs.

Discussion

In the present study we evaluated the capacity of medetomidine—administered through four different protocols—to anesthetize rats for up to six hours and sustain temporally stable fMRI measures of stimulus-evoked activity and functional connectivity. We found that anesthesia duration exceeded five hours in most sessions

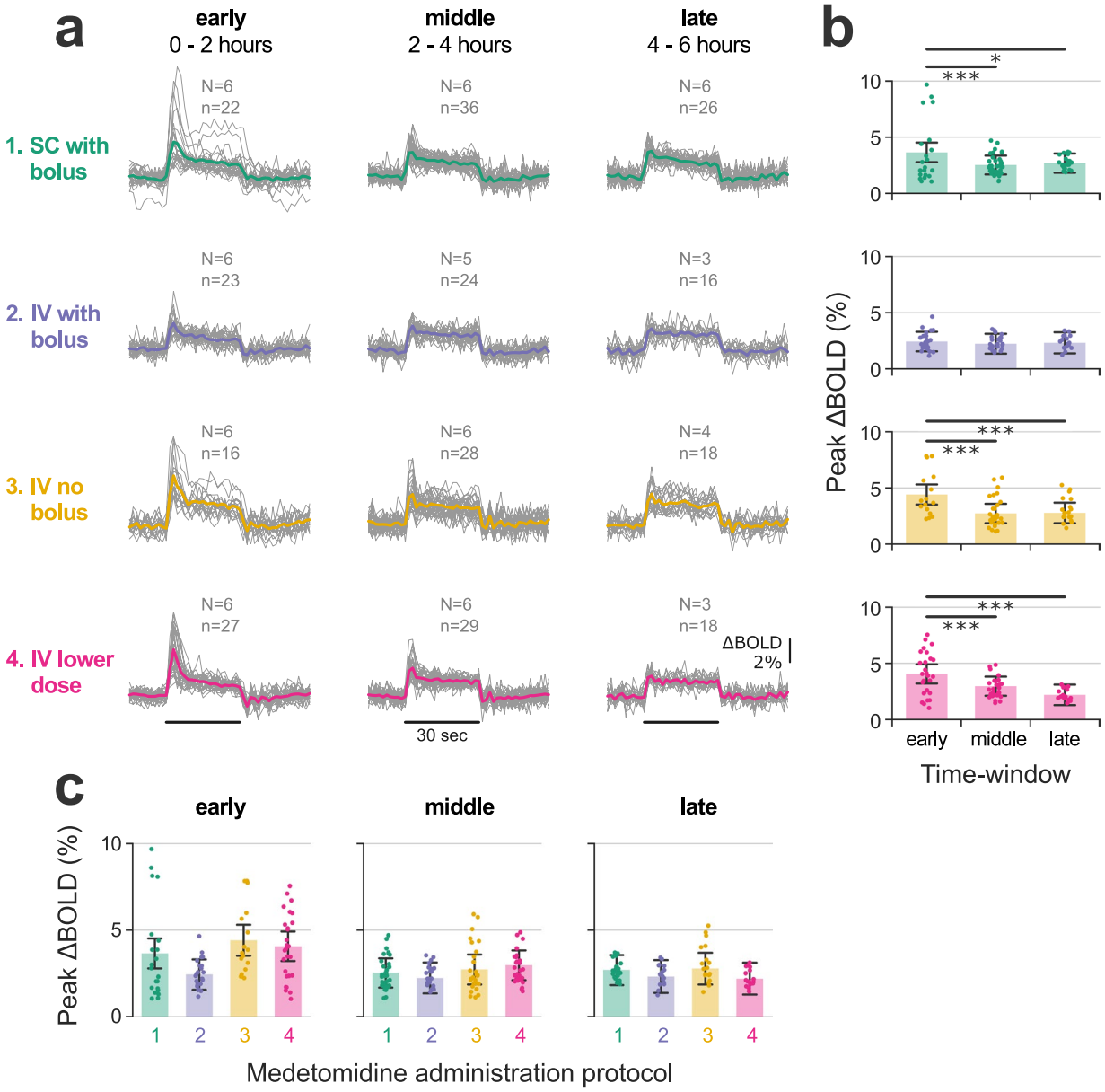

Figure 4. Temporal stability of stimulus-evoked responses. **(a)** Event-related averages produced by averaging the three electrical forepaw stimulation (EFS) blocks of each fMRI run. Single run traces are grouped according to the applied medetomidine protocol and the time-window since the start of medetomidine administration (early: 0–2 h; middle: 2–4 h; late: 4–6 h); each group's mean event-related average is plotted as a thicker trace; EFS duration is represented by horizontal lines. N: number of rats; n: number of fMRI runs. The peak stimulus-evoked signal change (peak ΔBOLD) is extracted from the event-related averages and plotted in **(b,c)**: in **(b)** peak ΔBOLD values are plotted across time-windows for each of the medetomidine protocols, while in **(c)** they are plotted across medetomidine protocols for each of the time-windows. Dots represent single run values, bars show the estimated Least Squares Means, while error margins correspond to the estimated 95% confidence intervals. Asterisks indicate the significance of pair-wise t-tests, after adjusting for multiple comparisons ($p < 0.05$: *, $p < 0.01$: **, $p < 0.001$: ***). Peak ΔBOLD time courses for individual rats are provided in Supplementary Fig. S7a. A complete list of Least Square Means, confidence intervals and pair-wise comparisons can be found in Supplementary Tables S10 and S11.

(35/48 or 72.9%; Fig. 2a), heart and respiratory rates were mostly stable after the first hour of anesthesia (Fig. 2b), and the majority of performed EFS-fMRI runs (241/283 or 85.16%) led to a significant and selective activation of the expected cortical area (Fig. 3a). However, both stimulus-evoked activity and functional connectivity exhibited varying temporal trends depending on the protocol of medetomidine administration (Figs 4 and 5).

Limited anesthesia duration has been referred to as a drawback of medetomidine protocols[34], even though the exact duration is not reported in most papers. According to a study that has addressed this issue, rats anesthetized by constant IV infusion woke up spontaneously 3.5–4 hours into the experiment[25]. However, the rats in that study

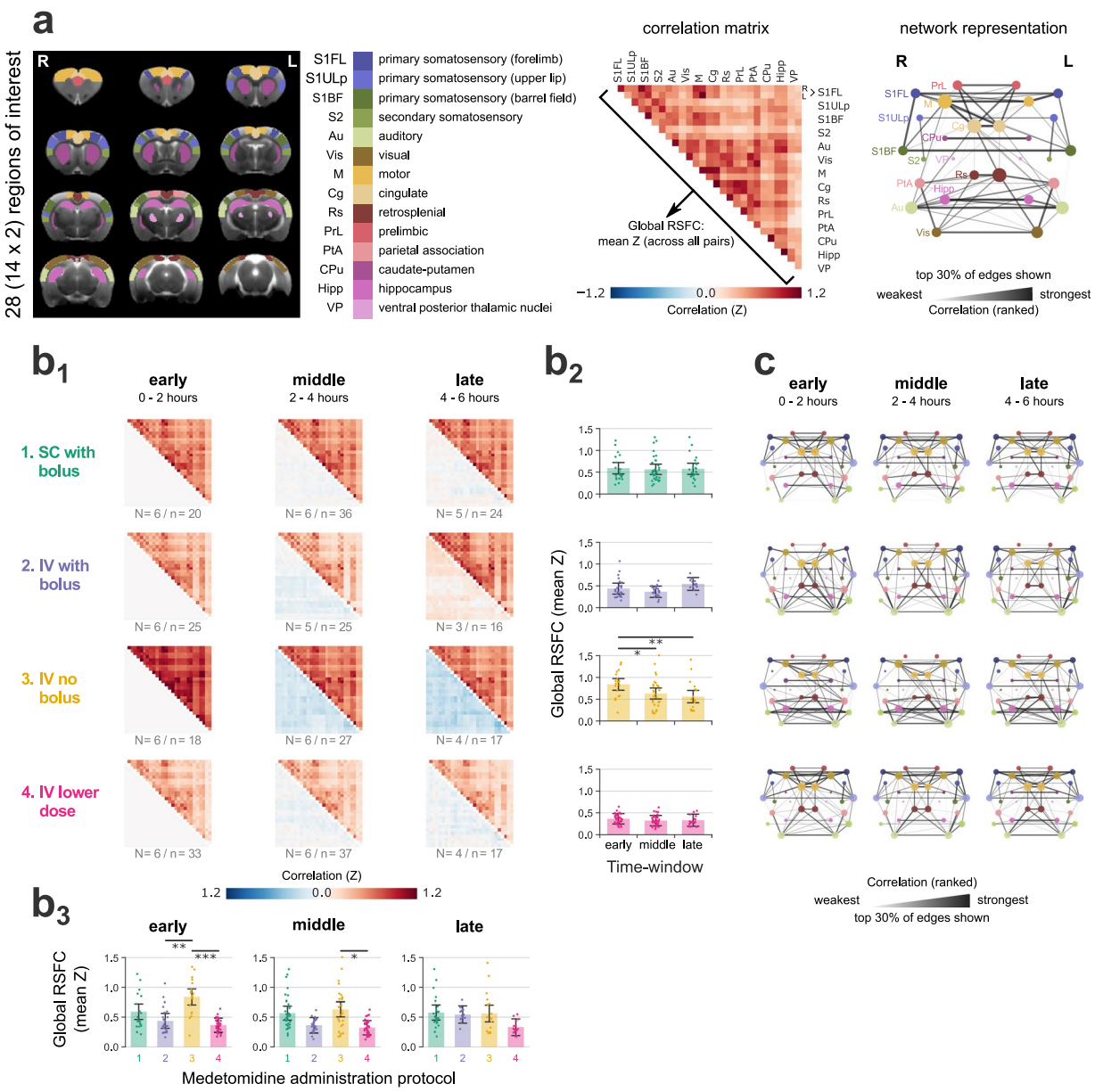

Figure 5. Resting state functional connectivity (RSFC). **(a)** To calculate pair-wise RSFC, 28 regions-of-interest (ROIs) were defined based on the Paxinos-Watson rat brain atlas—14 on each hemisphere. Pearson's correlations were calculated between the BOLD time courses of all unique ROI pairs and transformed into Fisher's Z-scores. A pair-wise correlation matrix is shown for one example RS-fMRI run; the mean correlation (Z-score) across all ROI pairs constitutes the global RSFC. The matrix is also represented as a weighted network graph, with the ROIs as nodes and their pairs as edges. For visualization clarity, only the strongest 30% of edges are shown; edge thickness and opacity scale linearly with the relative rank of the correlation value (the highest Z-score corresponds to the thickest edge); node radius scales with the weighted degree (weighted sum of edges passing through the node). **(b)** The 295 RS-fMRI runs are split into twelve groups according to the applied medetomidine protocol and the time-window since the start of medetomidine administration (early: 0–2 h; middle: 2–4 h; late: 4–6 h). **(b1)** For each group, the upper triangular matrix represents the mean (across runs) pair-wise correlation, while the lower triangular matrix shows the change in correlation compared to each protocol's early period. N: number of rats; n: number of fMRI runs. In **(b2)** global RSFC values are plotted across time-windows for each of the medetomidine protocols, while in **(b3)** they are plotted across medetomidine protocols for each of the time-windows. Dots represent single run values, bars show the estimated Least Squares Means, while error margins correspond to the estimated 95% confidence intervals. Asterisks indicate the significance of pair-wise t-tests, after adjusting for multiple comparisons ($p < 0.05$: *, $p < 0.01$: **, $p < 0.001$: ***). Global RSFC time courses for individual rats are provided in Supplementary Fig. S7b. A complete list of Least Square Means, confidence intervals and pair-wise comparisons can be found in Supplementary Tables S10 and S12. **(c)** The mean correlation matrices (upper triangles of **(b1)**) are also visualized as network graphs, similarly to the example graph in **(a)**.

were tracheotomized and mechanically ventilated, while most rat fMRI experiments—including ours—are conducted in freely breathing animals. The anesthesia durations achieved in our experiments should satisfy the needs of most researchers. That said, the risk of spontaneous wake-ups must be taken into consideration. In our study, these wake-ups occurred more often in fMRI than in bench sessions (13/24 versus 8/24)—a possible effect of the scanner's acoustic noise—and were typically preceded by an increase in RR and arrhythmic breathing. A timely identification of such an RR increase allows the researcher to promptly supply isoflurane through the mask in order to mitigate an un-controlled wake-up, and the associated animal stress. If early wake-ups must be avoided altogether, other administration practices may be warranted, such as stepping up the infusion rate[25], or adding a constant low dose of isoflurane throughout the imaging session[35]. The latter strategy has gained popularity in recent years, on the basis that it provides near-normal physiological conditions[35] and protects against epileptic seizures—which have been reported in animals with medetomidine-only anesthesia[36]. However, this might require mechanical ventilation, since even low doses of isoflurane, when combined with medetomidine, have been shown to suppress the amplitude of stimulus-evoked BOLD responses in spontaneously breathing rats[37].

The recorded cardiorespiratory parameters (HR and RR) underwent rapid changes in the first hour of anesthesia but stabilized thereafter (Fig. 2b). The observed changes agree with medetomidine pharmacology and with previous rat fMRI studies[20,23,38]. The decrease in HR immediately after medetomidine injection can be attributed to its well-described α_2-adrenergic effects. The activation of central nervous system α_2-adrenoreceptors causes bradycardia due to a decrease in central sympathetic tone, while α_2-adrenoreceptors in the peripheral vasculature mediate vasoconstriction. The latter mechanism leads to a transient elevation in blood pressure, which in turn exacerbates the bradycardia through a baroreceptor-mediated reflex[20]. The respiratory effects of medetomidine alone are considered to be minor[38]. However, medetomidine enhances the potency of isoflurane, and can thus amplify isoflurane-induced respiratory depression[20,39]. This is the most likely explanation for the observed sharp drop in RR right after medetomidine injection, as well as for its gradual recovery following isoflurane discontinuation. This effect necessitates the careful monitoring of animal physiology, especially in the transition period between isoflurane and medetomidine. In order to avoid severe respiratory depression, the speed with which isoflurane is faded out needs to be adapted to each individual animal.

The EFS-evoked activation of the contralateral S1FL (Fig. 3) is described by numerous other rat fMRI studies using the same stimulus[23–25]. For a subset of trials, these studies have also reported activations in the secondary somatosensory area and in sensory thalamic nuclei. If we increase statistical power by grouping multiple fMRI runs in a second-level analysis, we also find the same areas being responsive to EFS (see Supplementary Fig. S8). The shape of the EFS-evoked BOLD response in the S1FL (sharp peak at about 3 s after the onset of stimulation, followed by a plateau sustained till the end of EFS period; see Fig. 3c) is consistent with previous rat fMRI studies[24,40], and the time-to-peak is close to the one reported in rats anesthetized with α-chloralose (2.49 ± 0.31 s)[41]. It is worth noting that this is considerably shorter than the 4–8 s delay commonly assumed in modelling the human hemodynamic response, which could be attributed to a species difference in vascular anatomy and dynamics[41].

The temporal evolution of stimulus-evoked responses exhibited an interesting dependence on the medetomidine administration protocol (Fig. 4). All four protocols converged to steady-state peak ΔBOLD of 2–3% after the first two hours of medetomidine administration, but arrived there through different temporal trajectories. An IV bolus of 0.05 mg/kg followed by a continuous infusion of 0.1 mg/kg/h (protocol 2) had already achieved the steady-state since the early time-window. Deviating from the above dosage, either by omitting the bolus (protocol 3) or by downscaling both bolus and infusion doses (protocol 4), resulted in a time-dependent decrease from the early to the middle time-windows. This implies that early responses under protocols 3 and 4 were stronger than under protocol 2—an effect that appears in the data (Fig. 4c) but does not survive the multiple comparisons correction (see Supplementary Table S11). Omitting the bolus (protocol 3) also led to a time-dependent decrease in global RSFC: the overall pair-wise correlation strength dropped significantly between the early and middle time-windows. This time-dependent attenuation of BOLD readouts in sessions that lacked the bolus could reflect a negative relationship between the strength of these readouts and the concentration of medetomidine. Drug levels in the central nervous system might take hours to stabilize under the continuous infusion regime, given that the pharmacokinetics of medetomidine is characterized by a long terminal half-life of about 57 min, and a hysteresis between plasma and cerebrospinal fluid concentrations[38,42]. Bolus administration likely mediates a faster wash-in of the drug and an earlier establishment of the steady state. For this interpretation, we need to accept that medetomidine dose-dependently suppresses stimulus-evoked BOLD responses and RSFC, at least up to a certain level. Previous studies have in fact found such a dose-dependency for RSFC, but not for stimulus-evoked responses[40,43]. That said, the relevant experiments were restricted to a higher infusion rate range of 0.1–0.3 mg/kg/h (always preceded by a bolus), within which any effects on stimulus-evoked responses could have been saturated.

The case of protocol 1—the SC variant of protocol 2 and the most widely used administration scheme (see Supplementary Table 1)—is a peculiar one. Like protocols 3 and 4, it also exhibited a decrease in peak BOLD between the early and middle time-windows. However, a closer examination of individual rat trajectories (see Supplementary Fig. S7) reveals that this effect was driven by only two rats with exceptionally strong responses within the first 90 minutes; the other four rats produced temporally stable responses. This observation can be interpreted within the framework of dose-dependent response attenuation that was proposed above. Small variations in the injection site and/or the skin temperature may have delayed the drug's absorption into the blood-stream, leading to the observed stronger responses in a sub-set of rats. However, this interpretation cannot be verified without measuring blood concentrations of medetomidine, which we have not performed.

At this point, we would like to emphasize several limitations of the present study. We have no way of dissecting the vascular and neuronal contributions to the observed effects on BOLD readouts: we lack electrophysiological recordings of neural activity and important measures of vascular physiology, such as cerebral blood flow and arterial blood gas concentrations. We also lack fMRI data for very early time points: the earliest fMRI runs

were acquired 30–50 minutes after the onset of medetomidine administration, due to the time spent for animal positioning, structural image acquisition and shimming, and the required overlap between medetomidine administration and isoflurane anesthesia. This delay was most pronounced for protocol 3, during which the said overlap was necessarily prolonged. To put our results into proper context, we would also like to point out the main methodological differences between our study and the existing rat fMRI literature. We used female rats, contrary to almost all other similar studies (Supplementary Table S1). Sex can affect drug metabolism through multiple potential mechanisms[44], so the optimal dosing scheme may differ between males and females. Moreover, the rats in our study were lying supinely in the custom-built rat bed (Supplementary Fig. S2), as opposed to the conventional prone position. In our experience, the supine position reduces respiration-related head motion, to a degree that allows us to avoid using ear bars (See Supplementary Fig. S6). The unconventional position and the absence of ear bars, which are a potentially painful stimulus, could have influenced physiological parameters and the duration of anesthesia.

Despite these limitations, our study does provide an empirical answer to the question of how BOLD readouts evolve over long-lasting medetomidine anesthesia sessions, allowing us to recommend best practices for fMRI studies in rats. Protocols 1 (SC with bolus) and 2 (IV with bolus), which follow the dosage of the originally published protocol[23], are both well-suited for long-lasting fMRI sessions. The choice between them depends on the priorities of the researchers. Whenever maximizing the duration of the steady-state is deemed crucial, protocol 2 is the optimal choice. The main advantage of this protocol lies within the early two hours of anesthesia, since all four protocols converge to a similar steady-state after this time. This is however an important benefit: because the probability of spontaneous wake-ups increases over time, an earlier establishment of the steady-state can significantly prolong the useful experimental time. That said, we recommend always allowing a waiting period of 60 minutes between the bolus injection and the start of functional experiments. The first hour is characterized by rapid changes in cardio-respiratory physiology and is thus best reserved for structural image acquisition. If researchers prefer the practicality of the SC route, they should consider extending this waiting period to 90–120 minutes. We do not claim that these protocols (1 and 2) are necessarily the best choice for rat fMRI, since our study did not include all existing (see Supplementary Table S1) or possible administration protocols. It is however reasonable to consider them as the current 'default' choice, in light of the wealth of available data, and in the interest of promoting comparability among studies.

Methods

Experimental animals. All experiments followed the standards of the German Federal Law on Care and Use of Laboratory Animals and were approved by the local government authorities (Lower Saxony State Office for Consumer Protection and Food Safety, approval number 33.19-42502-04-15/2042). A total number of 24 female adult Wistar rats (Charles Rivers Laboratories, Sulzfeld Germany) with a median body weight of 308 g (interquartile range 285–350 g) were used for this study. Rats were group-housed in cages with environmental enrichment, at a 12/12-hour light/dark cycle, with 20–24 °C temperature and 45–55% humidity. Water and standard chow were provided ad libitum. The 24 rats were split into four equally sized groups, each assigned to a different protocol of medetomidine administration (see Table 1). No animal was excluded from the experiments or from the analysis. The investigators were not blind to the group allocation.

Anesthesia and monitoring. Each animal was anesthetized on two sessions separated by a minimum of two weeks. The first session took place on a laboratory bench-top to accommodate unrestricted access to the animal and close monitoring of anesthesia duration and cardio-respiratory physiology (bench session). The functional imaging took place during the second session, performed inside a dedicated small animal MR system (fMRI session). All applied anesthetic protocols followed the same general outline, with isoflurane being used during preparation, and medetomidine during data acquisition (Fig. 1a).

Unconsciousness was induced in a chamber filled with 5% isoflurane and maintained throughout preparation with 2–3% isoflurane in medical air, supplied through a nose cone. The animal was placed in a supine position for both bench and fMRI sessions. The eyes were covered with ophthalmic ointment to prevent them from drying. A cannula was inserted in the SC tissue of the left flank (protocol 1) or in a tail vein (protocols 2–4). Two subdermal needle electrodes were placed in the right forepaw, between the 2nd and the 4th digit. Monitoring equipment was attached, consisting of a rectal temperature probe, a pneumatic pressure sensor placed on the chest, and three SC needle electrodes for electrocardiogram (ECG). After fixing the equipment with adhesive tape, the animal was transferred to a custom-built MRI-compatible rat bed.

Four different protocols of medetomidine administration were used: 1) SC with bolus; 2) IV with bolus; 3) IV no bolus; 4) IV lower dose. The detailed dosing for all protocols is given in Table 1. For protocols 1, 2, and 4, medetomidine (Dorbene vet, Zoetis Deutschland GmbH, Germany) was initially given as a bolus loading dose, followed by a gradual reduction of isoflurane and its eventual discontinuation 10 min later. To mitigate the risk of respiratory depression during this transition period, we tailored the speed of the gradual isoflurane reduction to each individual animal—aiming for a RR range of 40–70 bpm. Continuous infusion of medetomidine commenced 15 min after the bolus. The bolus was omitted for protocol 3, with continuous infusion starting directly after the preparation phase, and isoflurane being gradually reduced to zero over the course of 20–25 min. Attempts to shut off isoflurane earlier led to fast breathing, indicative of an imminent wake-up (bench sessions). All doses were delivered using an MRI-compatible infusion pump (PHD 2000 Infuse/Withdraw; Harvard apparatus, Holliston, Massachusetts, USA), which was loaded with the medetomidine solution diluted 1/20 in saline (final concentration of 0.05 mg/ml). From the start of medetomidine administration, heart rate (HR), respiratory rate (RR), and rectal temperature were monitored using the MR-compatible Model 1030 monitoring and gating system (Small Animal Instruments Inc., Stony Brook, NY 11790, USA). Rectal temperature was kept at 36.5 ± 1 °C using a pad heated by circulating water. Anesthesia was maintained for six hours since the start of

medetomidine administration, except for sessions in which the rat spontaneously woke up earlier. For bench sessions, such wake-ups were identified as spontaneous movements of the rat and were found to be always preceded by the RR getting progressively faster and irregular. Since the animal is not visible during fMRI, the endpoint for fMRI sessions was set based on respiration (RR > 90/min, irregular, and continuously rising for at least 2 min). Anesthesia duration was defined as the time from the start of medetomidine administration (time = 0) till one of the aforementioned endpoints: spontaneous movement, rapid rise in RR, or passage of six hours. Upon reaching an endpoint, the animal was provided with 2% isoflurane through the nose cone and was disconnected from all electrodes, cannulas, and monitoring equipment. Finally, isoflurane was shut off and atipamezole (Atipazole, Prodivet pharmaceuticals, Belgium) was injected SC (0.25 mg/kg for protocols 1–3; 0.175 mg/kg for protocol 4) to facilitate a smooth wake-up.

The monitoring data (HR and RR traces) were recorded at a temporal resolution of 1 s and further processed with in-house python scripts as follows. Firstly, physiologically implausible values—corresponding to data acquisition errors—were dropped. Secondly, fMRI acquisition periods were removed from HR traces, since the rapidly switching magnetic gradients had introduced electrical noise in the ECG recording. Lastly, the traces were smoothed with an exponentially weighted moving average filter (smoothing factor $\alpha = 0.02$). The processed HR and RR traces from bench and fMRI sessions closely resembled each other and were therefore pooled together. For each of the four medetomidine protocols the mean ($\pm$ s.d.) HR/RR trace was calculated across all anesthesia sessions.

MRI acquisition. The fMRI sessions were performed inside a 9.4 Tesla Bruker BioSpec MR system, equipped with the BGA12 gradient, and operated via ParaVision 6.0.1 software. Signal was transmitted via a volume resonator (inner diameter 86 mm) and received by a rat brain 4-channel coil array (all equipment and software from Bruker BioSpin MRI GmbH, Ettlingen, Germany). Approximately 10 min after the discontinuation of isoflurane, the rat was positioned in the isocenter of the MR system, with its body lying supinely and its head fixed with the help of a bite bar. After obtaining low-resolution images for animal localization, a T2-weighted structural image was acquired using a TurboRARE sequence (repetition time 5.225 s, effective echo time 33 ms; 2 averages; RARE factor 8; 30–50 axial slices with a thickness of 0.5 mm; in-plane resolution 0.137×0.137 mm^2; matrix size 256×256). A field map was measured, and shims were adjusted to ensure homogeneity in an ellipsoidal volume encompassing the rat brain (MAPSHIM). This was followed by multiple 330-second-long BOLD fMRI runs, repeated approximately every 10 min, until the experimental endpoint was reached. All fMRI runs were acquired with a single-shot gradient-echo echo planar imaging sequence (220 repetitions; repetition time 1.5 s; echo time 15 ms; flip angle 90°; 30 axial slices with a thickness of 0.5 mm, ascending interleaved slice order with no slice gap; in-plane resolution 0.2×0.2 mm^2; matrix size 128×96; 4 dummy scans; bandwidth 375 kHz). The fMRI slices covered the entire rat brain, excluding the olfactory bulbs and the caudal 3/4 of the cerebellum. Consecutive fMRI runs were alternated between somatosensory fMRI with electrical forepaw stimulation (EFS-fMRI) and resting state fMRI (RS-fMRI) with no stimulus (Fig. 1b). This resulted in a total number of 283 EFS-fMRI and 295 RS-fMRI runs across all rats, spanning from 0.5 up to 6 hours since the start of medetomidine administration. EFS-fMRI runs included a baseline period of 60 s, followed by stimulation of the right forepaw in three 30 s blocks—each paired with 60 s of rest (Fig. 1c). Each stimulus block comprised square unipolar pulses with 3 mA amplitude and 0.3 ms pulse width, delivered at 9 Hz (Stimulus Generator 4002, Multi Channel Systems MCS GmbH, Reutlingen, Germany). The above parameters were chosen based on previous EFS studies in medetomidine-anesthetized rats[24,25,45].

MRI preprocessing. All MR images were first exported from ParaVision to DICOM format and then converted to NIfTI (Neuroimaging Informatics Technology Initiative; http://nifti.nimh.nih.gov) using the dcm2nii (https://www.nitrc.org/projects/dcm2nii/) tool. The structural T2-weighted images were used to construct a study template with the help of the Advanced Normalization Tools software—ANTs (http://stnava.github.io/ANTs/). The structural image of one of the rats was chosen as the target reference space. Every other structural image was registered to the target in two steps. First a linear rigid (3 translations and 3 rotations) registration was used to bring each structural image to the same origin and orientation as the reference image. This was followed by a non-linear symmetric diffeomorphic (SyN) registration to account for differences in brain size and shape[46]. All 24 structural images were averaged in the reference space to produce a mean anatomical image. A down-sampled ($0.2 \times 0.2 \times 0.5$ mm^3) version of this image was used to create a brain mask and served as the study template to which all functional datasets were eventually registered. The fMRI image series were preprocessed using functions from multiple neuroimaging toolkits, combined into a pipeline with python's Nipype library[47]. Images were corrected for slice timing with FSL (FMRIB Software Library, https://fsl.fmrib.ox.ac.uk/fsl/fslwiki/) and temporally filtered with AFNI (https://afni.nimh.nih.gov/). A high-pass filter of 0.01 Hz was used to remove slow temporal drifts, with an additional low-pass filter of 0.15 Hz being applied to RS-fMRI datasets only. Spatial smoothing (FSL) was performed using a 0.5 mm 3D Gaussian kernel. We chose to skip motion correction and regression of nuisance variables, as these preprocessing steps were shown to have little effect in anesthetized and head-fixed rodents[48]. Besides, a quantification of motion parameters showed that motion was minimal across all fMRI runs (see Supplementary Fig. S6). A rigid transformation matrix was calculated between the mean image of each functional run and the native structural image. This matrix was combined with the previously calculated linear and non-linear transforms into a composite warp file, which was used to transform the preprocessed fMRI datasets into the study template space (ANTs).

fMRI analysis and statistics. Areas activated during each EFS-fMRI run were identified via a first-level general linear model analysis carried out using FEAT (FMRI Expert Analysis Tool) Version 6.00, part of FSL[49].

The stimulus time course (1 during stimulation, 0 elsewhere) was convolved with a standard double-gamma hemodynamic response function to generate the model predictor. The resulting statistical maps were masked for brain, thresholded non-parametrically using clusters determined by $z > 3.1$ and a corrected cluster significance threshold of $p = 0.05$[50,51], binarized, and averaged across all 283 EFS-fMRI runs to construct an overall activation probability map. The region active in at least 30% of all EFS-fMRI runs (contralateral S1FL; see Fig. 3a) was taken as a region-of-interest (ROI). This ROI's mean BOLD time course was extracted from each EFS-fMRI run, normalized to the pre-stimulus baseline, and averaged across the three stimulation blocks to produce an event-related average. The peak % signal change (peak ΔBOLD) was extracted from the event-related average, as a measure of BOLD response strength (Fig. 3b). We also performed a second-level fixed-effects analysis (FEAT) for each medetomidine protocol, by pooling the corresponding EFS-fMRI runs and computing the mean group effect. The resulting statistical maps were masked for brain and thresholded non-parametrically using maximum height thresholding based on Gaussian random field theory, with a (corrected) significance threshold of $P = 0.05$[50,51].

Resting state functional connectivity (RSFC) analysis was performed using in-house python scripts. All 295 preprocessed RS-fMRI datasets were normalized by subtracting the temporal mean and dividing by the standard deviation. Normalized BOLD signal time courses were extracted from 28 ROIs (14 on each hemisphere), manually delineated based on the Paxinos-Watson rat brain atlas[52] (see Fig. 5a, left). Pearson's correlation coefficients were calculated for all ROI pairs, transformed into Fisher's Z-scores, and stored as a pair-wise correlation matrix. The mean Z-score across all 378 unique ROI pairs served as a measure of global RSFC. To visualize the hierarchical structure of the functional connectome, each correlation matrix was also represented as a weighted graph, with the ROIs as nodes and the ROI pairs as edges. The edges were ranked by ascending correlation strength, and the rank was assigned as the numerical weight of the edge (strongest correlation to highest weight). Figure 5a (right) depicts a pair-wise correlation matrix and its graph representation for an example RS-fMRI run.

Statistical analysis was performed in R, version 3.6.1 (https://www.r-project.org/). We used the lmer function of the lme4 package[53] to design a linear mixed effects model, separately for each of two response variables: the EFS-evoked response strength (peak ΔBOLD) and the global RSFC (mean Z-score). This model can account for the repeated-measures design of the study and for missing data points (e.g. due to spontaneous earlier wake-ups). The fMRI runs were grouped into three two-hour-long time-windows (early: 0–2 h; middle: 2–4 h; late: 4–6 h), based on the onset time of their acquisition. The time-window, the medetomidine administration protocol, and their interaction were modeled as fixed effects, while individual rat intercepts were included as random effects. This approach treats the time-window as a within-subject repeated-measures factor and the medetomidine protocol as a between-subject factor. Model inference and statistical tests were carried out using the lmerTest package[54]. Specifically, Satterthwaite's method was used to create Type III Analysis of Variance (ANOVA) tables, and the ls_means function was used to estimate Least Squares Means for all sub-classes (levels of protocol, time-window, and their combinations). Finally, the difflsmeans function was applied to estimate pair-wise differences between the sub-class means; the resulting p-values were adjusted for multiple comparisons according to the Holm method[55]. The ANOVA tables and the outputs of ls_means and difflsmeans functions can be found in the Supplementary Material (Supplementary Tables S9–S12).

Data availability

The unprocessed anatomical and functional MRI data are publicly available through the OpenNeuro repository (https://openneuro.org/datasets/ds001981/). They are provided in NIfTI format and organized according to the BIDS specification (Brain Imaging Data Structure, https://bids.neuroimaging.io/). The preprocessing scripts (python) can be shared upon request.

Received: 18 June 2019; Accepted: 29 October 2019;
Published online: 13 November 2019

References

1. Ogawa, S., Lee, T. M., Kay, A. R. & Tank, D. W. Brain magnetic resonance imaging with contrast dependent on blood oxygenation. *Proc. Natl. Acad. Sci.* **87**, 9868–9872 (1990).
2. Biswal, B., Zerrin Yetkin, F., Haughton, V. M. & Hyde, J. S. Functional connectivity in the motor cortex of resting human brain using echo-planar mri. *Magn. Reson. Med.* **34**, 537–541 (1995).
3. Fox, M. D. & Raichle, M. E. Spontaneous fluctuations in brain activity observed with functional magnetic resonance imaging. *Nat. Rev. Neurosci.* **8**, 700–711 (2007).
4. Greicius, M. Resting-state functional connectivity in neuropsychiatric disorders. *Curr. Opin. Neurol.* **24**, 424–430 (2008).
5. Jonckers, E., Shah, D., Hamaide, J., Verhoye, M. & van der Linden, A. The power of using functional fMRI on small rodents to study brain pharmacology and disease. *Front. Pharmacol.* **6**, 231 (2015).
6. Albers, F., Wachsmuth, L., van Alst, T. M. & Faber, C. Multimodal Functional Neuroimaging by Simultaneous BOLD fMRI and Fiber-Optic Calcium Recordings and Optogenetic Control. *Mol. Imaging Biol.* **20**, 171–182 (2018).
7. Schulz, K. *et al.* Simultaneous BOLD fMRI and fiber-optic calcium recording in rat neocortex. *Nat. Methods* **9**, 597–602 (2012).
8. Yu, X. *et al.* Sensory and optogenetically driven single-vessel fMRI. *Nat. Methods* **13**, 337 EP- (2016).
9. Wang, M., He, Y., Sejnowski, T. J. & Yu, X. Brain-state dependent astrocytic Ca^{2+} signals are coupled to both positive and negative BOLD-fMRI signals. *Proc. Natl. Acad. Sci. USA* **115**, E1647–E1656 (2018).
10. Gao, Y. R. *et al.* Time to wake up: Studying neurovascular coupling and brain-wide circuit function in the un-anesthetized animal. *Neuroimage* **153**, 382–398 (2017).
11. Liang, Z., Liu, X. & Zhang, N. Dynamic resting state functional connectivity in awake and anesthetized rodents. *Neuroimage* **104**, 89–99 (2015).
12. Paasonen, J., Stenroos, P., Salo, R. A., Kiviniemi, V. & Gröhn, O. Functional connectivity under six anesthesia protocols and the awake condition in rat brain. *Neuroimage* **172**, 9–20 (2018).
13. Masamoto, K. & Kanno, I. Anesthesia and the quantitative evaluation of neurovascular coupling. *J. Cereb. Blood Flow Metab.* **32**, 1233–1247 (2012).

14. Pan, W.-J., Billings, J. C. W., Grooms, J. K., Shakil, S. & Keilholz, S. D. Considerations for resting state functional MRI and functional connectivity studies in rodents. *Front. Neurosci.* **9**, 269 (2015).
15. Schroeter, A., Schlegel, F., Seuwen, A., Grandjean, J. & Rudin, M. Specificity of stimulus-evoked fMRI responses in the mouse: the influence of systemic physiological changes associated with innocuous stimulation under four different anesthetics. *Neuroimage* **94**, 372–384 (2014).
16. Grandjean, J., Schroeter, A., Batata, I. & Rudin, M. Optimization of anesthesia protocol for resting-state fMRI in mice based on differential effects of anesthetics on functional connectivity patterns. *Neuroimage* **102**(Pt 2), 838–847 (2014).
17. Schlegel, F., Schroeter, A. & Rudin, M. The hemodynamic response to somatosensory stimulation in mice depends on the anesthetic used: Implications on analysis of mouse fMRI data. *Neuroimage* **116**, 40–49 (2015).
18. Shim, H.-J. *et al*. Mouse fMRI under ketamine and xylazine anesthesia: Robust contralateral somatosensory cortex activation in response to forepaw stimulation. *Neuroimage* **177**, 30–44 (2018).
19. Scheinin, H., Virtanen, R., Macdonald, E., Lammintausta, R. & Scheinin, M. Medetomidine — a novel α2-adrenoceptor agonist: A review of its pharmacodynamic effects. *Prog. Neuro-Psychopharmacology Biol. Psychiatry* **13**, 635–651 (1989).
20. Sinclair, M. D. A review of the physiological effects of alpha2-agonists related to the clinical use of medetomidine in small animal practice. *Can. Vet. J.* **44**, 885–897 (2003).
21. Brown, E. N., Purdon, P. L. & van Dort, C. J. General anesthesia and altered states of arousal: a systems neuroscience analysis. *Annu. Rev. Neurosci.* **34**, 601–628 (2011).
22. Weber, R., Ramos-Cabrer, P., Wiedermann, D. & Hoehn, M. A longitudinal and totally noninvasive fMRI protocol in rats. *J. Cereb. Blood Flow Metab.* **25**, S361–S361 (2005).
23. Weber, R., Ramos-Cabrer, P., Wiedermann, D., Van Camp, N. & Hoehn, M. A fully noninvasive and robust experimental protocol for longitudinal fMRI studies in the rat. *Neuroimage* **29**, 1303–1310 (2006).
24. Zhao, F., Zhao, T., Zhou, L., Wu, Q. & Hu, X. BOLD study of stimulation-induced neural activity and resting-state connectivity in medetomidine-sedated rat. *Neuroimage* **39**, 248–260 (2008).
25. Pawela, C. P. *et al*. A protocol for use of medetomidine anesthesia in rats for extended studies using task-induced BOLD contrast and resting-state functional connectivity. *Neuroimage* **46**, 1137–1147 (2009).
26. Williams, K. A. *et al*. Comparison of alpha-chloralose, medetomidine and isoflurane anesthesia for functional connectivity mapping in the rat. *Magn. Reson. Imaging* **28**, 995–1003 (2010).
27. Kalthoff, D., Po, C., Wiedermann, D. & Hoehn, M. Reliability and spatial specificity of rat brain sensorimotor functional connectivity networks are superior under sedation compared with general anesthesia. *NMR Biomed.* **26**, 638–650 (2013).
28. Boretius, S., Tammer, R., Michaelis, T., Brockmoller, J. & Frahm, J. Halogenated volatile anesthetics alter brain metabolism as revealed by proton magnetic resonance spectroscopy of mice *in vivo*. *Neuroimage* **69**, 244–255 (2013).
29. Masamoto, K., Kim, T., Fukuda, M., Wang, P. & Kim, S.-G. Relationship between neural, vascular, and BOLD signals in isoflurane-anesthetized rat somatosensory cortex. *Cereb. Cortex* **17**, 942–950 (2007).
30. Pisauro, M. A., Dhruv, N. T., Carandini, M. & Benucci, A. Fast Hemodynamic Responses in the Visual Cortex of the Awake Mouse. *J. Neurosci.* **33**, 18343 LP–18351 (2013).
31. Aksenov, D. P., Li, L., Miller, M. J., Iordanescu, G. & Wyrwicz, A. M. Effects of anesthesia on BOLD signal and neuronal activity in the somatosensory cortex. *J. Cereb. Blood Flow Metab.* **35**, 1819–26 (2015).
32. Liu, X., Zhu, X.-H., Zhang, Y. & Chen, W. The change of functional connectivity specificity in rats under various anesthesia levels and its neural origin. *Brain Topogr.* **26**, 363–377 (2013).
33. Magnuson, M. E., Thompson, G. J., Pan, W. J. & Keilholz, S. D. Time-dependent effects of isoflurane and dexmedetomidine on functional connectivity, spectral characteristics, and spatial distribution of spontaneous BOLD fluctuations. *NMR Biomed.* **27**, 291–303 (2014).
34. Chuang, K.-H. & Nasrallah, F. A. Functional networks and network perturbations in rodents. *Neuroimage* **163**, 419–436 (2017).
35. Brynildsen, J. K. *et al*. Physiological characterization of a robust survival rodent fMRI method. *Magn. Reson. Imaging* **35**, 54–60 (2017).
36. Fukuda, M., Vazquez, A. L., Zong, X. & Kim, S.-G. G. Effects of the alpha(2)-adrenergic receptor agonist dexmedetomidine on neural, vascular and BOLD fMRI responses in the somatosensory cortex. *Eur. J. Neurosci.* **37**, 80–95 (2013).
37. van Alst, T. M. *et al*. Anesthesia differentially modulates neuronal and vascular contributions to the BOLD signal. *Neuroimage* **195**, 89–103 (2019).
38. Bol, C. J. J. G., Danhof, M., Stanski, D. R. & Mandema, J. W. Pharmacokinetic-Pharmacodynamic Characterization of the Cardiovascular, Hypnotic, EEG and Ventilatory Responses to Dexmedetomidine in the Rat. *J. Pharmacol. Exp. Ther.* **283**, 1051–1058 (1997).
39. Ewing, K. K., Mohammed, H. O., Scarlett, J. M. & Short, C. E. Reduction of isoflurane anesthetic requirement by medetomidine and its restoration by atipamezole in dogs. *Am. J. Vet. Res.* **54**, 294–9 (1993).
40. Nasrallah, F. A., Lew, S. K., Low, A. S.-M. & Chuang, K.-H. Neural correlate of resting-state functional connectivity under α2 adrenergic receptor agonist, medetomidine. *Neuroimage* **84**, 27–34 (2014).
41. Silva, A. C., Koretsky, A. P. & Duyn, J. H. Functional MRI impulse response for BOLD and CBV contrast in rat somatosensory cortex. *Magn. Reson. Med.* **57**, 1110–1118 (2007).
42. Bol, C. J. J. G., Vogelaar, J. P. W. & Mandema, J. W. Anesthetic profile of dexmedetomidine identified by stimulus-response and continuous measurements in rats. *J. Pharmacol. Exp. Ther.* **291**, 153–60 (1999).
43. Nasrallah, F. A., Tan, J. & Chuang, K.-H. H. Pharmacological modulation of functional connectivity: α2-adrenergic receptor agonist alters synchrony but not neural activation. *Neuroimage* **60**, 436–446 (2012).
44. Czerniak, R. Gender-Based Differences in Pharmacokinetics in Laboratory Animal Models. *Int. J. Toxicol.* **20**, 161–163 (2001).
45. Li, N., Van Zijl, P., Thakor, N. & Pelled, G. Study of the spatial correlation between neuronal activity and BOLD fMRI responses evoked by sensory and channelrhodopsin-2 stimulation in the rat somatosensory cortex. *J. Mol. Neurosci.* **53**, 553–561 (2014).
46. Avants, B. B., Epstein, C. L., Gossman, M. & Gee, J. C. Symmetric diffeomorphic image registration with cross-correlation: Evaluating automated labeling of elderly and neurodegenerative brain. *Med. Image Anal.* **12**, 26–41 (2008).
47. Gorgolewski, K. *et al*. Nipype: A Flexible, Lightweight and Extensible Neuroimaging Data Processing Framework in Python. *Front. Neuroinform.* **5**, 13 (2011).
48. Chuang, K. H. *et al*. Evaluation of nuisance removal for functional MRI of rodent brain. *Neuroimage* **188**, 694–709 (2019).
49. Woolrich, M. W., Ripley, B. D., Brady, M. & Smith, S. M. Temporal Autocorrelation in Univariate Linear Modeling of FMRI Data. *Neuroimage* **14**, 1370–1386 (2001).
50. Smith, S. M. Overview of fMRI analysis. in *Functional Magnetic Resonance Imaging* 216–230 (Oxford University Press, 2001).
51. Worsley, K. J. Statistical analysis of activation images. in *Functional Magnetic Resonance Imaging* 251–270 (Oxford University Press, 2001).
52. Paxinos, G. & Watson, C. *The rat brain in stereotaxic coordinates*. (Elsevier, 2007).
53. Bates, D., Mächler, M., Bolker, B. & Walker, S. Fitting Linear Mixed-Effects Models Using lme4. *J. Stat. Softw.* **67**, 1–48 (2015).
54. Kuznetsova, A., Brockhoff, P. & Christensen, R. lmerTest Package: Tests in Linear Mixed Effects Models. *J. Stat. Software, Artic.* **82**, 1–26 (2017).
55. Holm, S. A Simple Sequentially Rejective Multiple Test Procedure. *Scand. J. Stat.* **6**, 65–70 (1979).

Acknowledgements
This work was supported by the DFG (Deutsche Forschungsgemeinschaft) Research Center for Nanoscale Microscopy and Molecular Physiology of the Brain (CNMPB), and a DAAD (German Academic Exchange Service) stipend to N.S. We wish to thank Kristin Kötz, Kerstin Fuhrmann, and Luzia Hintz for their excellent technical assistance.

Author contributions
The study was devised by J.B. and S.B. Experiments and data analysis were performed by N.S. Results were discussed and interpreted by all co-authors. The manuscript was written by N.S., in consultation with S.B. and J.B. All authors reviewed the manuscript.

Competing interests
The authors declare no competing interests.

Additional information
Supplementary information is available for this paper at https://doi.org/10.1038/s41598-019-53144-y.

Correspondence and requests for materials should be addressed to N.S.

Reprints and permissions information is available at www.nature.com/reprints.

Publisher's note Springer Nature remains neutral with regard to jurisdictional claims in published maps and institutional affiliations.

3

BRAINS AREAS INVOLVED IN ANESTHESIA-INDUCED BURST-SUPPRESSION DIFFER SIGNIFICANTLY BETWEEN PRIMATES AND RODENTS

AUTHORS

Nikoloz Sirmpilatze[1,2,3], Jürgen Baudewig[1], Judith Mylius[1], Daniel Golkowski[4], Andreas Ranft[4], Rüdiger Ilg[4], Jaakko Paasonen[5], Olli Gröhn[5], and Susann Boretius[1,2,3,6].

1. Functional Imaging Laboratory, German Primate Center—Leibniz Institute for Primate Research, Göttingen, Germany
2. Georg-August University of Göttingen, Göttingen, Germany
3. International Max Planck Research School for Neurosciences, Göttingen, Germany
4. Klinikum Rechts der Isar der Technischen Universität München, Munich, Germany
5. A.I.V. Institute for Molecular Sciences, University of Eastern Finland, Kuopio, Finland
6. Leibniz Science Campus Primate Cognition, Göttingen, Germany

OWN CONTRIBUTIONS

- Conceptualization and study design (together with SB)
- Data collection: rat anesthesia and MRI
- Data analysis
- Data interpretation (together with SB)
- Data visualization
- Writing of original draft
- Editing (together with SB)

This study has been prepared for submission to a journal and is provided below in the form of a research article.

ABSTRACT

In many deeply anesthetized and comatose states the brain's electroencephalographic (EEG) signal alternates between bursts of slow waves and periods of suppressed activity. The origin of this burst-suppression pattern and its distribution across the brain are debated. In this work, we used functional magnetic resonance imaging (fMRI) to map the brain areas involved in burst-suppression across four mammalian species: humans, long-tailed macaques, common marmosets, and rats. We achieved this by first determining the fMRI signatures of burst-suppression based on human EEG-fMRI data and then identifying these signatures in fMRI datasets from anesthetized animals. The burst-suppression maps revealed a marked inter-species difference: in rats the entire neocortex engaged in burst-suppression, while in primates certain cortical areas were excluded—most notably the primary visual cortex. We expect the identified fMRI signatures and whole-brain maps to guide future invasive studies and facilitate translational research on the role of burst-suppression in anesthesia and coma.

3.1 INTRODUCTION

Despite a long-standing and successful practice of general anesthesia, an understanding of its underlying mechanisms remains elusive. Yet, most anesthetics lead to a dose-dependent transition from mild sedation to deep coma, accompanied by an orderly progression of distinct electroencephalographic (EEG) patterns (Brown et al., 2010, 2011). This progression is well characterized for halogenated volatile agents, like isoflurane (Kroeger et al., 2013). Low isoflurane concentrations lead to a pattern of high-amplitude slow waves, whereas at higher doses, the ongoing activity is quasi-periodically interrupted by quiescent periods that can last from seconds to minutes. This alternation between bursts of slow waves and gaps of suppressed activity is termed burst-suppression (Swank, 1949; Swank and Watson, 1949). As anesthesia deepens, periods of suppression become longer and ultimately culminate in complete electrical silence. The same sequence unfolds for many other anesthetics (e.g. propofol, barbiturates, etomidate) and even during deep hypothermia, with suppression periods becoming longer as temperature decreases (Akrawi et al., 1996; Fleischmann et al., 2018; Westover et al., 2015; Zhang et al., 2010). Burst-suppression also appears in comas of various etiologies (e.g. hypoxia, intoxication, metabolic encephalopathies), for which it holds diagnostic and prognostic value (Brenner, 1985; Brown et al., 2010; Cloostermans et al., 2012; Hofmeijer et al., 2014; Young, 2000). In medically-induced comas, burst-suppression is often used as the target EEG activity, indicating a neuroprotective depth of anesthesia (An et al., 2015; Westover et al., 2015).

The ubiquitous presence of burst-suppression in a variety of unconscious conditions has led some researchers to propose that it represents a common low-order "attractor" state—a hallmark of a profoundly inactive brain operating at a low metabolic regime (Ching et al., 2012). Several models have attempted to explain how the observed bistable temporal pattern could arise in such a regime (Bojak et al., 2015; Ching et al., 2012; Kroeger and Amzica, 2007; Liley and Walsh, 2013). Meanwhile, many open questions surround the spatial properties of bursts—namely, their origin and propagation across brain areas. Bursts have traditionally been viewed as globally synchronous events, based on their

simultaneous occurrence across EEG electrodes (Clark and Rosner, 1973; Swank, 1949). More recent data, coming from electrocorticograms in humans (Lewis et al., 2013) and widefield calcium imaging in rats (Ming et al., 2021), have challenged this view by demonstrating considerable spatial variation in burst origin and propagation. Furthermore, it is yet unclear whether burst-suppression is intrinsically cortical or is controlled by some subcortical input. According to one hypothesis, the cortex spontaneously falls into burst-suppression upon anatomical or functional disconnection from other brain areas. This view is supported by observations of burst-suppression in isolated neocortical slice preparations (Lukatch et al., 2005; Lukatch and MacIver, 1996), but contradicted by the ability of sensory stimuli to evoke bursts that are indistinguishable from the spontaneously-occurring ones (Hartikainen et al., 1995; Hudetz and Imas, 2007; Kroeger and Amzica, 2007; Land et al., 2012).

Incorporating detailed spatial information into burst-suppression models could reduce the pool of possible mechanisms. Such information, in the form of 3D whole-brain maps, can be provided by blood-oxygen-level-dependent (BOLD) functional Magnetic Resonance Imaging (fMRI, Ogawa et al., 1990). The two distinct phases of burst-suppression correspond to different levels of energy consumption, which should—through neurovascular coupling—translate to discernable changes in blood flow and oxygenation (Hillman, 2014). This premise has been confirmed in several species. In rats, a combination of EEG with optical imaging of cerebral blood flow revealed that bursts are coupled with strong hemodynamic responses (Liu et al., 2011). The same effect was demonstrated in macaques (Zhang et al., 2019) and humans (Golkowski et al., 2017) using simultaneous EEG-fMRI. The same studies have shown that the burst timing from EEG can be used for fMRI mapping of burst-suppression.

While the preservation of neurovascular coupling during burst-suppression holds promise for anesthesia and coma research, it creates pitfalls for the increasingly popular animal fMRI studies. About 4/5 of such studies are conducted under anesthesia, most commonly with isoflurane (Mandino et al., 2020). Given that medium-to-high doses of isoflurane lead to burst-suppression (Kroeger et al., 2013), we can assume that some animal fMRI measurements have been acquired during this state. This assumption is supported by reports of global BOLD signal synchronization in isoflurane-anesthetized animals (Kalthoff et al., 2013; Liu et al., 2013; Paasonen et al., 2018), as is expected during burst-suppression (Zhang et al., 2019). Animal fMRI researchers typically try to avoid this confounding effect by using low doses of isoflurane (Liu et al., 2013), opting for different anesthetic regimes (Kalthoff et al., 2013; Paasonen et al., 2018), or applying global signal regression during fMRI preprocessing (Kalthoff et al., 2013; Liu et al., 2013; Zhang et al., 2019).

However, burst-suppression is not a nuisance variable, but a biologically and clinically significant neural phenomenon. In this work, we set out to exploit its 'confounding' effects on fMRI to generate directly comparable maps of burst-suppression across multiple mammalian species. For this purpose, we combined data acquired under anesthesia from humans, long-tailed macaques, common marmosets, and rats (see Table 3.1 for a full dataset list). We first used an existing human EEG-fMRI dataset (Golkowski et al., 2017; Ranft et al., 2016) to identify the fMRI signatures of burst-suppression. We found that this state can be reliably detected based on its fMRI pattern alone, using a simple

	HUMAN	MACAQUE	MARMOSET	RAT 1	RAT 2
Species/Strain		*M. fascicularis*	*C. jacchus*	Wistar	Wistar
Site	Munich	Göttingen	Göttingen	Göttingen	Kuopio
Field strength	3T	3T	9.4T	9.4T	7T
Subjects (N)	20	13	20	11	6
Sex	M	F	10F	F	M
Age (years)	26 (20 – 36)	13.7 (6.8 – 19.8)	6.1 (1.9 – 14.2)		
BW (kg)		5.4 (3.6 – 8.1)	0.41 (0.34 – 0.52)	0.40 (0.35 – 0.45)	0.31 (0.27 – 0.35)
Anesthetic	sevoflurane	isoflurane	isoflurane	isoflurane	isoflurane
Dose (%)	2.0 – 4.6	0.95 – 1.5	0.6 – 1.1	1.5 – 2.5	1.3

Table 3.1: Datasets analyzed in this study. For age and body weight (BW), mean and range values are reported. Anesthetic dose refers to the range of concentrations used during fMRI acquisition. In humans and macaques, the measured end-tidal concentration of the anesthetic gas is reported; in marmosets and rats, the output concentration of the vaporizer.

heuristic algorithm. We then applied this algorithm to the animal fMRI data, identified instances of burst-suppression, and constructed species-specific, burst-suppression maps. These maps provide a detailed and comparative spatial account of burst-suppression in some of the most widely used animal models. We hope that they will serve as a guide for targeted invasive studies and facilitate translational research into the mechanisms of burst-suppression and its role in brain (patho)physiology

3.2 RESULTS

3.2.1 *fMRI signatures of EEG-defined burst-suppression in humans*

Simultaneous EEG-fMRI recordings offer a straightforward way of constructing a whole-brain map of burst-suppression: EEG supplies the timing of burst and suppression phases, which is convolved with a hemodynamic response function (HRF) and correlated with the fMRI timeseries to produce voxel-wise statistical parametric maps (Golkowski et al., 2017; Zhang et al., 2019). However, simultaneous EEG-fMRI recordings are challenging, particularly at high magnetic field strengths. Knowing the exact hemodynamic correlates of burst-suppression may circumvent the need for concurrent EEG, especially if these correlates are specific enough to serve as a unique fMRI signature.

To explore this approach, we analyzed data acquired in human subjects across a range of anesthetic depths. Specifically, we revisited an existing EEG-fMRI dataset (Ranft et al., 2016), which contains task-free measurements acquired at three different doses of the anesthetic sevoflurane—high (3.9–4.6%), intermediate (3%) and low (2%). Importantly, this dose range spans across EEG states, allowing us to examine how they differ in their fMRI manifestations. We categorized the EEG recordings as one of two states—burst-suppression or continuous slow wave activity (uninterrupted by suppressions). The high sevoflurane dose had been intentionally chosen in the initial study (Ranft et al., 2016) to induce burst-suppression, and indeed 19/20 subjects exhibited the typical bistable EEG al-

ternation at this dose (Figure 3.1a). The same applied to 4/20 subjects at the intermediate dose, albeit with shorter suppression phases. The remaining intermediate-dose recordings as well as all low-dose recordings showed uninterrupted slow wave EEG activity. These results are consistent with the known dose-dependency of burst-suppression.

To examine potential effects of the two aforementioned EEG states on fMRI timeseries, we used the so-called 'grayplot' or 'carpet plot'—a 2D representation of fMRI data suited for detecting global signal fluctuations (Aquino et al., 2020; Power, 2017). The carpet plot is a heatmap of BOLD signal intensity, where each row represents a normalized (z-score) voxel timeseries. Upon examining carpet plots from fMRI runs with EEG-defined burst-suppression, we identified pronounced signal fluctuations that spanned almost the entire cortex (Figure 3.1c). Conversely, fMRI runs with continuous slow wave EEG activity showed no such cortex-wide fluctuations (see supplementary Figure A.1a).

We next sought to quantify the exact correspondence between these widespread BOLD fluctuations and EEG burst-suppression. We performed principal component analysis (PCA) on the 2D matrix of cortical voxel timeseries and extracted the first five temporal components. In fMRI runs with cortex-wide fluctuations, the bistable pattern visible on the carpet plot was captured by one of the principal components (PCs)—in most cases the first PC (Figure 3.1d). This component was strongly correlated with most cortical voxel timeseries (Figure 3.1e), which shifted the histogram of Pearson's correlation coefficients (r) away from zero—unlike the symmetric zero-centered histograms of other PCs (Figure 3.1f). Due to this property, we will hereafter refer to such components as 'asymmetric' PCs and use the median of the cortex-wide r values as a measure of asymmetry. The presence of asymmetric PCs proved to be a reliable signature of burst-suppression. We demonstrate this in Figure 3.1g, showing the cortex-wide median r values for the first five PCs across all fMRI runs. The two EEG-defined states (burst-suppression vs continuous slow waves) were linearly separable based on the median r value alone: every run with EEG burst-suppression had a single PC with median $r > 0.45$, which was not the case for any of the runs with continuous slow waves. Only a single recording was an exception to this rule (subject 15 at high sevoflurane dose, see Figure 3.1g), exhibiting no asymmetric PC. The EEG of this recording showed near-constant suppression, interrupted by only one short burst.

So far, we have seen that burst-suppression is uniquely associated with an asymmetric PC that captures a widespread fluctuation in the cortical BOLD signal. Notably, this asymmetric PC closely follows the alternating burst-suppression pattern of EEG (Figure 3.1a-d) and likely is its direct hemodynamic correlate. To verify this last observation, we compared each asymmetric PC with a neurovascular model derived from the concurrent EEG recording. For constructing the model, we convolved the EEG pattern (1 for burst, 0 for suppression) with a canonical HRF (Glover, 1999) and passed the resulting timeseries through the bandpass filter used for fMRI preprocessing (Figure 3.1b). The BOLD signal of the asymmetric PCs was indeed strongly correlated with the EEG-derived model (Pearson's $r = 0.73 \pm 0.11$, mean $\pm$ SD), but with a notable time-lag between the two. A cross-correlation analysis (Figure 3.1h) showed that the asymmetric PC was delayed by 3.71 ± 2.22s (mean $\pm$ SD) compared to the neurovascular model. This lag can be probably attributed to a slowing of the HRF, which is an expected effect of anesthesia (Gao et al., 2017). To account for this, we also compared the asymmetric PCs to the EEG-derived mod-

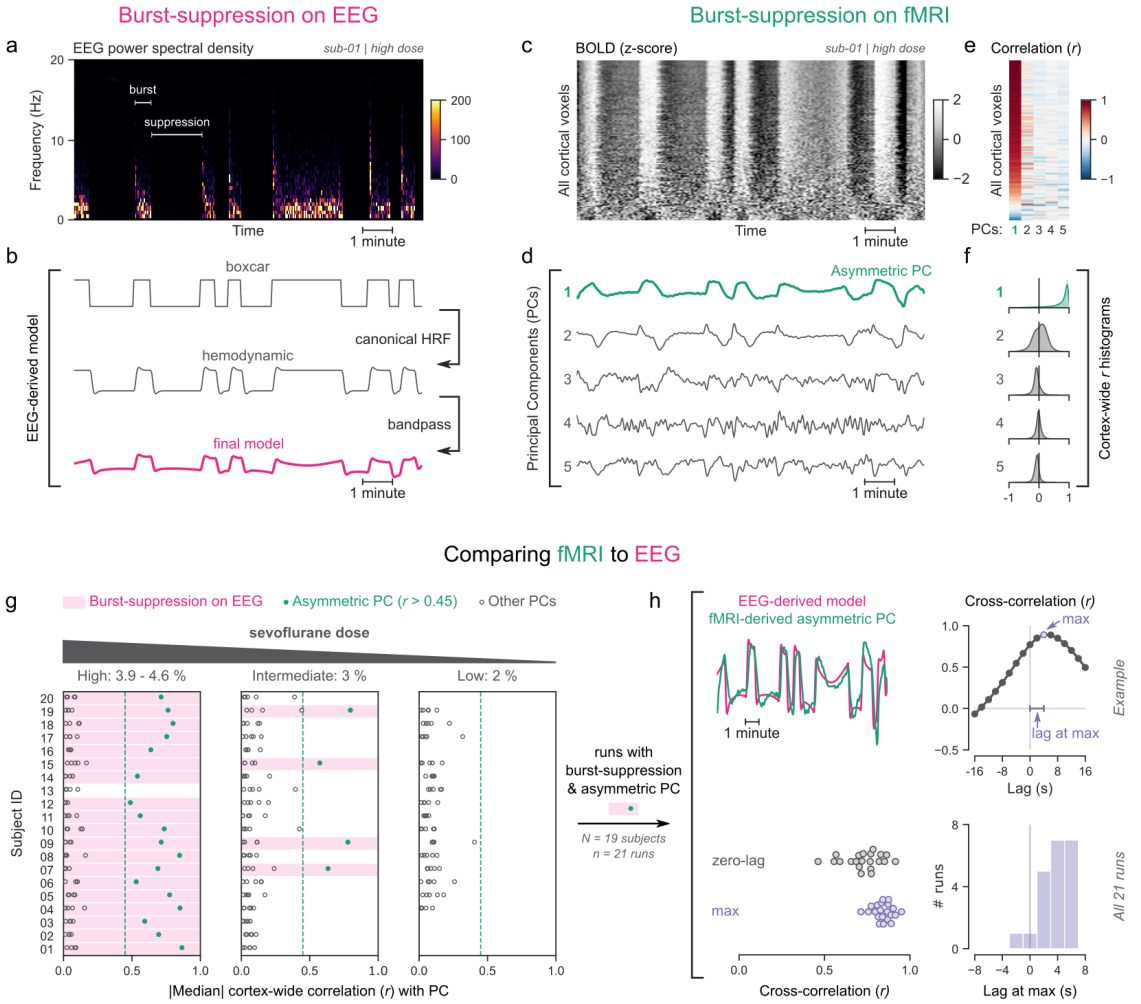

Figure 3.1: fMRI signatures of human burst-suppression. **a.** Burst and suppression phases are marked on an EEG spectrogram of a human participant under sevoflurane anesthesia. **b.** To derive the hemodynamic model of burst-suppression, the above phases (boxcar function) are convolved with a hemodynamic response function (HRF) and bandpass filtered (0.005—0.12 Hz). **c.** The cortical BOLD signal from the concurrent fMRI is represented as a 2D matrix (carpet plot). The rows (voxels) are ordered according to their correlation with the mean cortical signal. **d.** The first five temporal principal components (PCs) of the shown matrix are plotted. Pearson's correlation coefficients (r) between all cortical voxels and the first five PCs are shown both as a heatmap (**e**) and as histograms for each PC (**f**). Taken together, panels **c–f** demonstrate that burst-suppression manifests as a widespread cortical BOLD signal fluctuation, captured by the first PC. This component (PC1), unlike the rest, is positively correlated with most cortical voxels and is referred to as an 'asymmetric PC'. **g.** To demonstrate the correspondence between burst-suppression on EEG and asymmetric PCs on fMRI across the entire human dataset (20 participants, each with 2—3 EEG-fMRI runs at different sevoflurane doses), median cortex-wide r values of the first five PCs are plotted as dots for each run. The runs that exhibit burst-suppression on EEG also have a single prominent asymmetric PC with median cortex-wide $r > 0.45$ (except for subject 15 at high dose). For these runs, the cross-correlation between EEG-derived hemodynamic models and asymmetric PCs is shown (**h**). The cross-correlation at zero-lag, the maximum cross-correlation, and the time-lag at the maximum are extracted for each run (see example in top row) and plotted across all runs (bottom row).

els at the time lags that maximized their cross-correlation and found that the correlation increased at $r = 0.84 \pm 0.06$.

3.2.2 *Mapping burst-suppression in humans without EEG*

Since asymmetric PCs are the hemodynamic correlates of burst-suppression, their spatial distribution should give us a whole-brain map of burst-suppression. The map should be equivalent to the one obtained via the existing approach—i.e. using the EEG-derived models as regressors in a general linear model (GLM, as in Golkowski et al., 2017). We verified this by performing two GLM analyses for each fMRI run with burst-suppression—one with the asymmetric PC and one with the EEG-derived model (without time lag correction). As expected, the spatial patterns of the resulting Z statistical maps were nearly identical between the two analyses: neighborhood cross-correlation $r = 0.96 \pm 0.03$ (Figure 3.2a).

In order to map the brain regions involved in burst-suppression across subjects, we performed a second-level group GLM using the asymmetric PCs as regressors. The group statistics were carried out in the MNI152 template space (Grabner et al., 2006) with the FSL (FMRIB's Software Library) tool randomise (Winkler et al., 2014). The resulting T statistic maps were thresholded using Threshold-Free Cluster Enhancement (TFCE, Smith and Nichols, 2009) and a corrected $P < 0.05$ (Figure 3.2b). The group map revealed significant correlation with asymmetric PCs (burst-suppression) in the striatum and across most of the cortex, with the prominent exception of occipital areas in and around the calcarine sulcus—the location of primary visual cortex (V1). In addition to V1, several other cortical patches were non-correlated with burst-suppression. We have visualized these patches on an inflated representation of the cortical surface (Figure 3.2c–d). Some of them overlapped with primary cortices: somatosensory and motor areas around the central sulcus, and auditory areas on the dorsal bank of superior temporal gyrus—including Heschl's gyrus (Figure 3.2d). Additional patches included the subcallosal cortex (subgenual cingulate), the parahippocampal gyrus, and the border between the insula and the frontoparietal operculum. Supplementary Figure A.2a provides a closer look at subcortical structures. Anterior and midline parts of the thalamus were significantly correlated with burst-suppression, whereas posterior thalamic nuclei, the cerebellar cortex, the hippocampus, and the amygdala were (for the most part) not.

Intriguingly, we observed significant anticorrelation with burst-suppression at the ventricular borders. After a closer examination of this effect (see supplementary Figure A.4), we believe this to be an artifact caused by a shrinkage of the ventricles during bursts and their re-expansion during suppressions. Widespread hemodynamic fluctuations may exert a 'pumping' effect on the ventricles—an explanation consistent with recent reports of cerebrospinal fluid oscillations during sleep (Fultz et al., 2019).

3.2.3 *Burst-suppression maps in nonhuman primates resemble the human map*

Having identified an fMRI signature of burst-suppression in the human data, we moved on to look for similar signatures in animal fMRI data. We first explored an fMRI dataset of female long-tailed macaques (*Macaca fascicularis*), acquired with a 3 T MRI system.

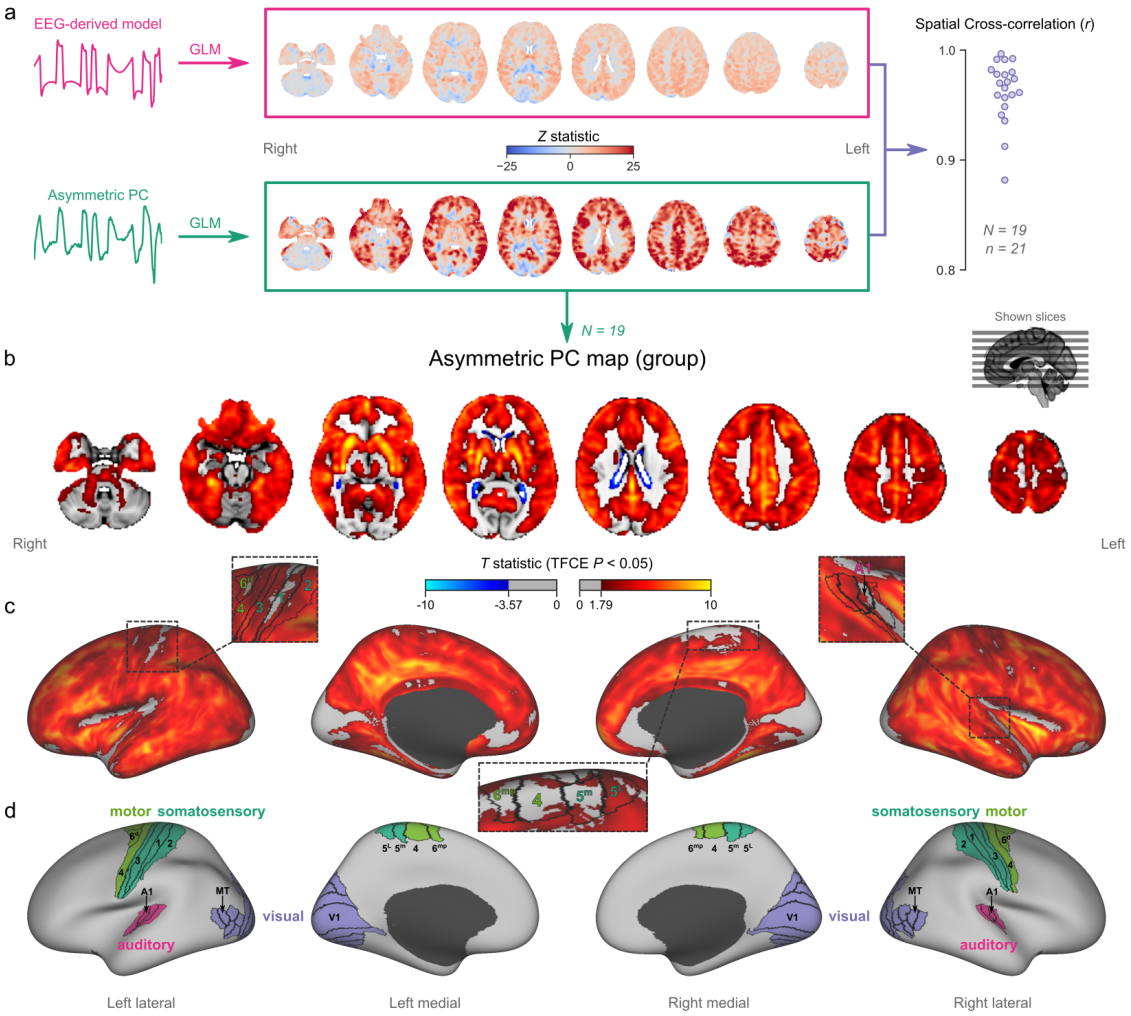

Figure 3.2: Human map of burst-suppression. **a.** Maps of burst-suppression are computed via general linear model (GLM) analysis, using one of two regressors—either the EEG-derived hemodynamic model or the fMRI-derived asymmetric PC. The resulting Z statistic maps for an example subject are shown here in the MNI152 template space. Neighborhood cross-correlation values between the two types of Z statistic maps are plotted on the right, across all runs with asymmetric PCs (N = 19 subjects, n = 21 EEG-fMRI runs). **b.** The group burst-suppression map, computed via a second-level analysis of the single-subject asymmetric PC GLMs, is shown here overlaid on the MNI152 volumetric template. The group statistics were carried out with FSL randomise; the resulting T statistic maps were thresholded using Threshold-Free Cluster Enhancement (TFCE) and a corrected $P < 0.05$. The same group map is shown in fsaverage surface space (**c**). Non-cortical areas on the medial surface are shown in dark gray. The locations of several sensory and motor cortical areas, based on the HCP multimodal parcellation, are indicated on the surface (**d**): primary motor (area 4), premotor (areas 6d and 6mp), primary somatosensory (areas 3a-b, 1, 2), higher somatosensory (areas 5m and 5L), primary auditory, higher auditory (medial and lateral belt, parabelt), primary visual, and higher-order visual (V2, V3, V3A, V3B, V4, V4t, V6, V6A, V7, V8, MT, MST, and lateral occipital areas 1–3).

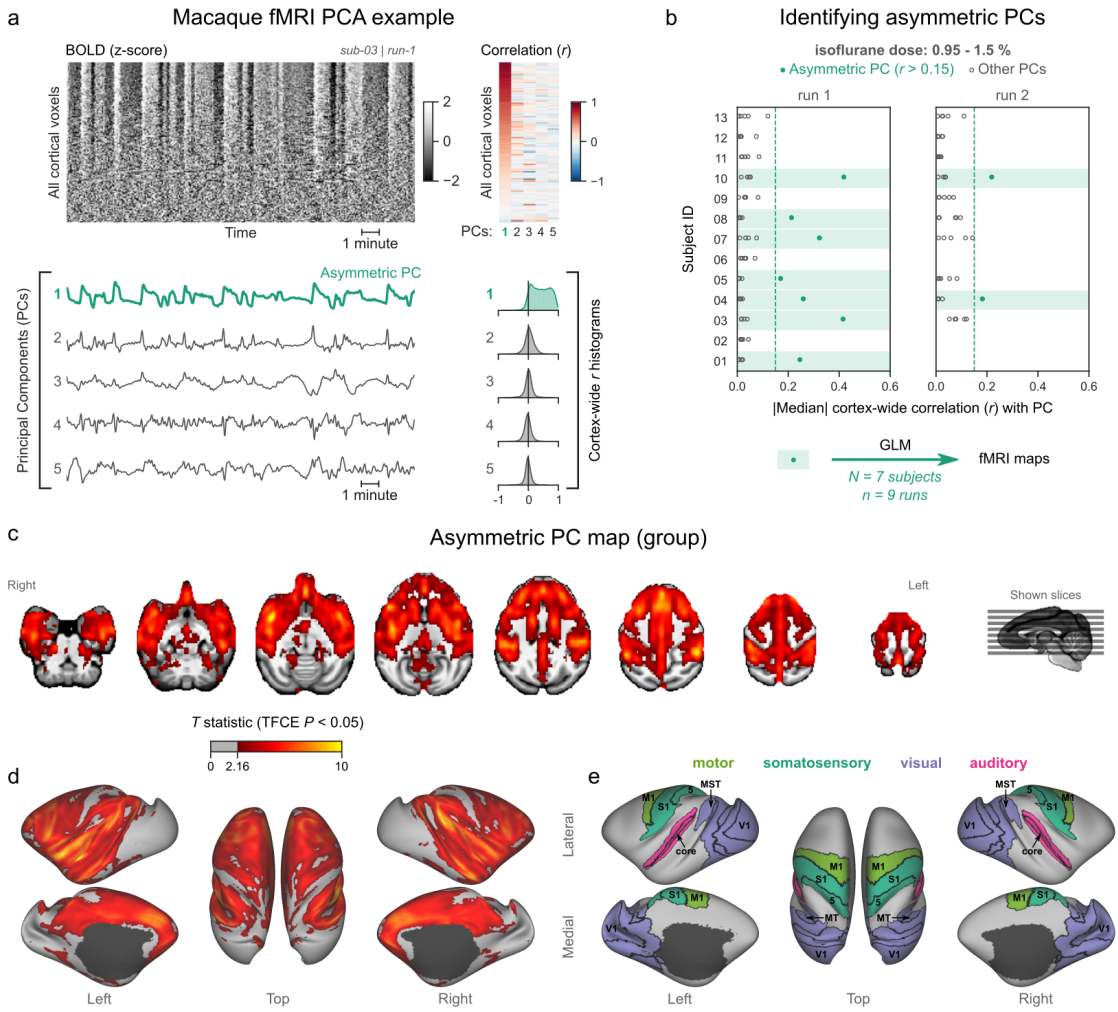

Figure 3.3: Identifying and mapping burst-suppression in macaques. **a.** The cortical BOLD fMRI signal of a long-tailed macaque during isoflurane anesthesia is represented as a carpet plot. The rows (voxels) are ordered according to their correlation with the mean cortical signal. The first five temporal principal components (PCs) of the signal are plotted below the carpet plot. The Pearson's correlation coefficients (r) between the PCs and all cortical voxels are represented both as a heatmap and as histograms for each PC. The first PC captures the widespread fluctuation that is visible on the carpet plot and has an asymmetric r histogram. **b.** Cortex-wide median r values for the first five PCs are plotted as dots across the entire macaque dataset (13 subjects, 1–2 fMRI runs each). The fMRI runs with a single prominent asymmetric PC ($r > 0.15$, highlighted in green) are selected for general linear model (GLM) analysis. **c.** The group asymmetric PC map, computed via a second-level analysis of single-subject GLMs, is shown here overlaid on a study-specific volumetric template. The group statistics were carried out with FSL randomise; the resulting T statistic maps were thresholded using Threshold-Free Cluster Enhancement (TFCE) and a corrected $P < 0.05$. The same group map is shown on a cortical surface representation of the template (**d**). Non-cortical areas on the medial surface are shown in dark gray. The locations of several sensory and motor cortical areas, based on the Cortical Hierarchical Atlas of the Rhesus Macaque (CHARM), are indicated on the surface (**e**): primary visual (V1), higher-order visual (V2, V3, V4, V6, MT, MST, FST), primary somatosensory (S1), higher somatosensory (area 5), primary motor (M1), and auditory cortices (auditory core, belt and parabelt).

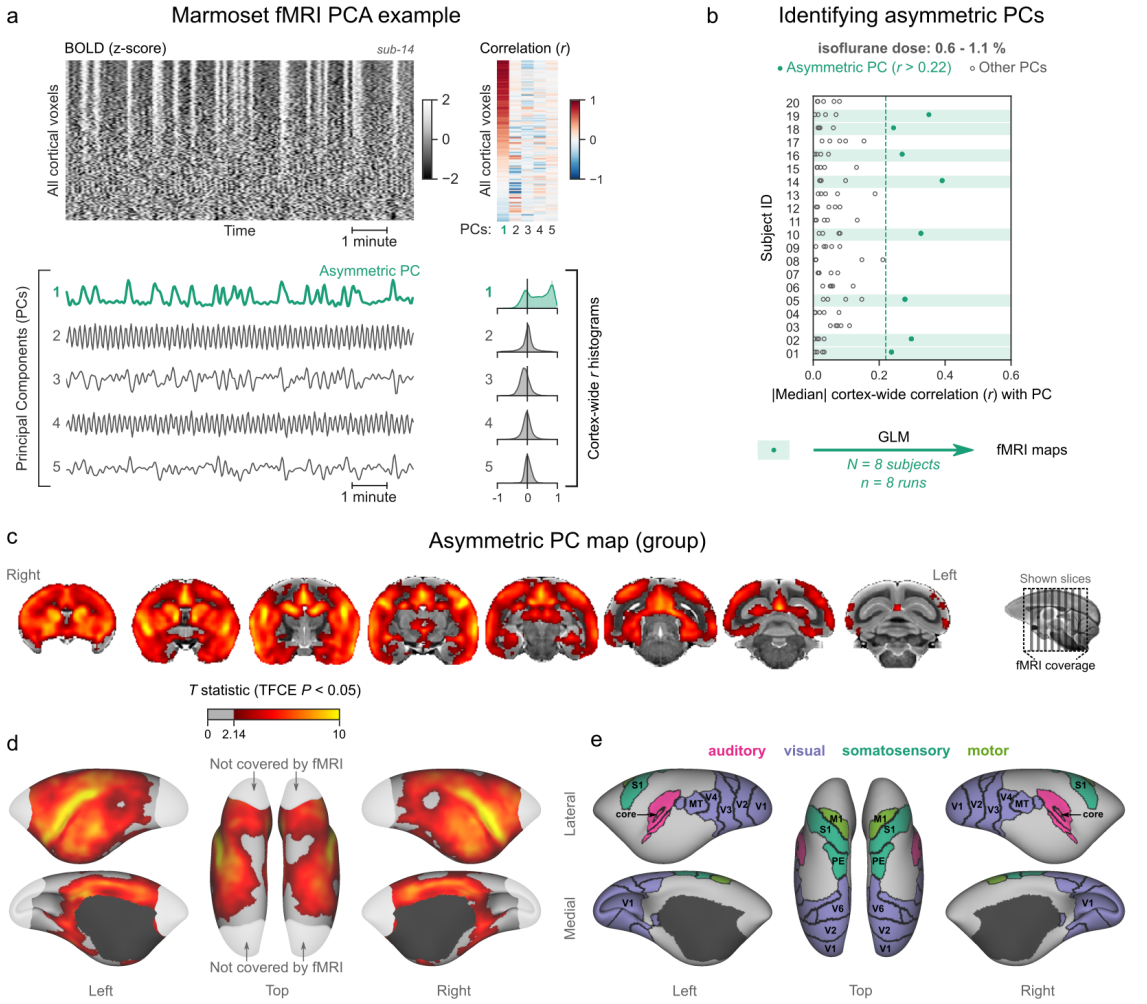

Figure 3.4: Identifying and mapping burst-suppression in marmosets. **a.** The cortical BOLD fMRI signal of a common marmoset during isoflurane anesthesia is represented as a carpet plot, with rows (voxels) ordered according to their correlation with the mean cortical signal. The first five temporal principal components (PCs) of the signal are plotted below the carpet plot. The Pearson's correlation coefficients (r) between the PCs and all cortical voxels are represented both as a heatmap and as histograms for each PC. The first PC captures the widespread fluctuation that is visible on the carpet plot and has an asymmetric r histogram. **b.** Cortex-wide median r values for the first five PCs are plotted as dots across the entire marmoset dataset (20 subjects, one fMRI run each). The fMRI runs with a single prominent asymmetric PC ($r > 0.22$, highlighted in green) are selected for general linear model (GLM) analysis. **c.** The group asymmetric PC map, computed via a second-level analysis of single-subject GLMs, is shown here overlaid on the NIH v3.0 population template (T2-weighted image). The group statistics were carried out with FSL randomise; the resulting T statistic maps were thresholded using Threshold-Free Cluster Enhancement (TFCE) and a corrected $P < 0.05$. The same group map is shown on a cortical surface representation of the template (**d**). Non-cortical areas on the medial surface are shown in dark gray. Areas not covered by the fMRI imaging volume are overlaid with white transparency. The locations of several sensory and motor cortical areas, according to the NIH MRI-based cortical parcellation, are indicated on the surface (**e**): primary visual (V1), higher-order visual (V2, V3, V4, V6, MT, MST, Brodmann area 19), primary somatosensory (S1), higher somatosensory (area PE), primary motor (M1), and auditory cortices (auditory core, belt, parabelt, and superior temporal rostral area).

Macaques are phylogenetically close to humans, have a long tradition of being used for neuroscientific research, and account for most fMRI studies in nonhuman primates (Milham et al., 2020). The macaques included in our study (N = 13, aged 6.8–19.8 years) were endotracheally intubated, mechanically ventilated, and anesthetized with isoflurane (end-tidal dose range 0.95–1.5%). For each macaque, one or two fMRI runs (each 10–20 min in duration) were acquired within a single imaging session.

We analyzed each fMRI run using the same approach as for human fMRI data—carpet plots and PCA. Several fMRI runs clearly exhibited the burst-suppression signature: a widespread bistable fluctuation on the carpet plot that was always captured by an asymmetric PC (see example in Figure 3.3a, counterexample in supplementary Figure A.1b). Figure 3.3b shows the cortex-wide median r value for the first five PCs across all fMRI runs. We selected nine runs (from 7/13 subjects) with a single prominent asymmetric PC (median $r > 0.15$) and used these PCs as regressors for GLM. The group statistical map—shown here overlaid on a study-specific structural template (Figure 3.3c–e)—exhibited striking similarities with the human burst-suppression map. Significantly correlated areas included the striatum and most of the cortex, with the following exceptions: V1, extrastriate visual areas, parts of somatosensory and motor cortices on either side of the central sulcus, the subcallosal cortex and the parahippocampal gyrus. The only notable difference to the human map was the auditory cortex, the entirety of which was among the positively correlated areas. Supplementary Figure A.2b provides a closer look at macaque subcortical structures. The cerebellar cortex was not correlated with burst-suppression, unlike some parts of the thalamus (anterior and midline), hippocampus, and amygdala which were. No significant anti-correlations were found around the ventricles or elsewhere.

We next sought to reproduce these findings in the common marmoset (*Callithrix jacchus*). The layout of areas in the marmoset brain closely resembles that of other primates (Liu et al., 2018), including macaques and humans. Yet, the animal's small body size—comparable to rats—allows it to fit into high-field small animal MRI systems that are routinely used for imaging rodents. These properties make the marmoset an ideal model for bridging neuroimaging results between larger primates and rodents. For this study we used fMRI data from 20 common marmosets (aged 1.9–14.2 years, 10/20 females), imaged on a 9.4 T MRI system. The anesthesia protocol resembled the one used for macaques: i.e. intubation, mechanical ventilation, and isoflurane anesthesia (dose range 0.6–1.1%). One fMRI run (10 min in duration) was acquired per animal.

We analyzed the data using the same approach as for humans and macaques. Here too we discovered a subset of fMRI runs that exhibited the burst-suppression signature (see example in Figure 3.4a, counterexample in supplementary Figure A.1c). Out of 20 subjects, we selected 8 in which a single asymmetric PC (median cortex-wide $r > 0.22$) was present and used these PCs as GLM regressors (Figure 3.4b). The group statistical map is shown overlaid on the NIH population template (Figure 3.4c–e). The result was functionally similar to the macaque map. Positively correlated areas comprised the striatum and a large part of the cortex—including auditory areas, but excluding V1, extrastriate visual areas, parts of somatosensory and motor cortices, and most of the parahippocampal gyrus. The cerebellar cortex and the thalamus (except for a small anterior part) were not correlated with burst-suppression, but parts of the hippocampus and the amygdala were (supplementary Figure A.3a). No significant anti-correlations were found.

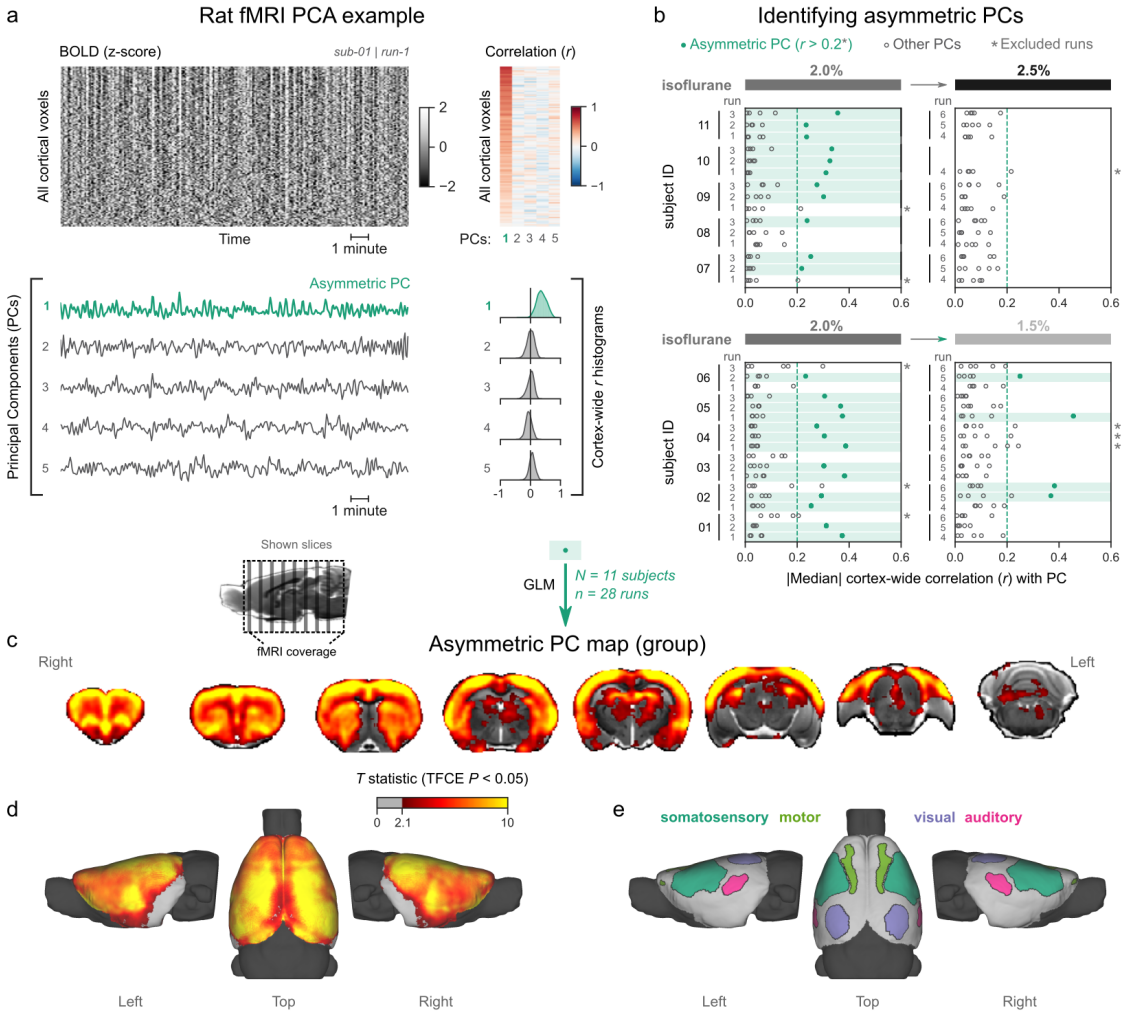

Figure 3.5: Identifying and mapping burst-suppression in rats. **a.** The cortical BOLD fMRI signal of a rat during isoflurane anesthesia is represented as a carpet plot, with rows (voxels) ordered according to their correlation with the mean cortical signal. The first five temporal principal components (PCs) of the signal are plotted below the carpet plot. The Pearson's correlation coefficients (r) between the PCs and all cortical voxels are represented both as a heatmap and as histograms for each PC. The first PC captures the widespread fluctuation that is visible on the carpet plot and has an asymmetric r histogram. **b.** Cortex-wide median r values for the first five PCs are plotted as dots across the entire rat dataset (11 animals, six fMRI runs each; except for rat 10 with only four runs). fMRI runs with a single prominent asymmetric PC ($r > 0.2$, highlighted in green) are selected, excluding runs that had a second PC within $r = 0.15$ of the most asymmetric PC (marked with an asterisk). The selected 28 runs serve as inputs for general linear model (GLM) analysis. **c.** The group asymmetric PC map, computed via a second-level analysis of single-subject GLMs, is shown here overlaid on a study-specific volumetric template. The group statistics were carried out with FSL randomise; the resulting T statistic maps were thresholded using Threshold-Free Cluster Enhancement (TFCE) and a corrected $P < 0.05$. The same group map is shown on a cortical surface representation of the template (**d**). The cerebellum and the olfactory bulb are shown in dark gray. The locations of primary motor, somatosensory, auditory, and visual cortices—based on the SIGMA rat brain atlas—are indicated on the surface (**e**).

3.2.4 *Burst-suppression in rats is pancortical*

Finally, we asked how our observations translate to rodents, specifically rats—the most popular animal model in preclinical fMRI (Mandino et al., 2020). Several studies have identified burst-suppression in electrophysiological recordings of rats anesthetized with isoflurane, mostly at doses between 1.3–2% (Detsch et al., 2002; Hudetz and Imas, 2007; Liu et al., 2011; Masamoto et al., 2009; Stenroos et al., 2021). One of these studies also described the potential fMRI correlate of burst-suppression in rats: widespread BOLD synchrony across the cortex and the striatum (Liu et al., 2011). Owing to this existing body of literature, we already anticipated at which isoflurane doses burst-suppression might occur, and how its map might look like. That said, we wondered whether our approach would lead to the same results. For this purpose, we acquired a rat fMRI dataset covering the dose range between 1.5–2.5% isoflurane. The animals (adult female Wistar rats, $N = 11$) were intubated, mechanically ventilated, and imaged at a 9.4 T MRI system. We first acquired three fMRI runs at 2% isoflurane—each covering 12 min, and then switched to either a lower (1.5%, in 6/11 rats) or a higher (2.5%, in 5/11 rats) dose before acquiring three additional fMRI runs.

We followed the same exploration and analysis procedure as in primates. Figure 3.5a shows an example fMRI run with an asymmetric PC (a counterexample can be found in supplementary Figure A.1d). We found multiple asymmetric PCs across all fMRI runs (Figure 3.5b). To select the ones that most resembled burst-suppression, we focused on the subset of runs containing at least one asymmetric PC with median cortex-wide $r > 0.2$ (37/64) but excluded nine runs that had a second PC with relatively high median r value (within $r = 0.15$ of the most asymmetric PC). We were left with 28 runs, 24 of which were acquired at 2% isoflurane, and four at 1.5%. We used the 28 asymmetric PCs as regressors in a GLM and constructed the group-level statistical map. The map is shown overlaid on a study-specific structural template (Figure 3.5c–e). The striatum and the entire neocortex were significantly correlated with the asymmetric PCs. In contrast to the primates, this included all primary sensory and motor cortices. The cerebellar cortex and the amygdala did not correlate with burst-suppression, while parts of the thalamus (medial) and the hippocampus did (see supplementary Figure A.3b). No significant anti-correlations were found.

The burst-suppression map shown in Figure 3.5, resembles a unified cortico-striatal network often found by BOLD fMRI studies in isoflurane-anesthetized rats (Kalthoff et al., 2013; Liu et al., 2011, 2013; Paasonen et al., 2018; Williams et al., 2010), suggesting that these studies may have been incidentally conducted during burst-suppression. To reinforce this claim, we revisited the data from one such study (Rat 2 dataset: six rats, anesthetized with 1.3% isoflurane, Paasonen et al., 2018) and subjected it to our preprocessing and analysis pipeline. As shown in supplementary Figure A.5, we found a single asymmetric PC (median cortex-wide $r > 0.2$) in all rats, with spatial distribution that exactly matched both the unified network described in the original study (Paasonen et al., 2018) and the rat burst-suppression map in this manuscript. This strongly suggests that the apparent unification of cortex and striatum into a single functional network was a direct effect of burst-suppression.

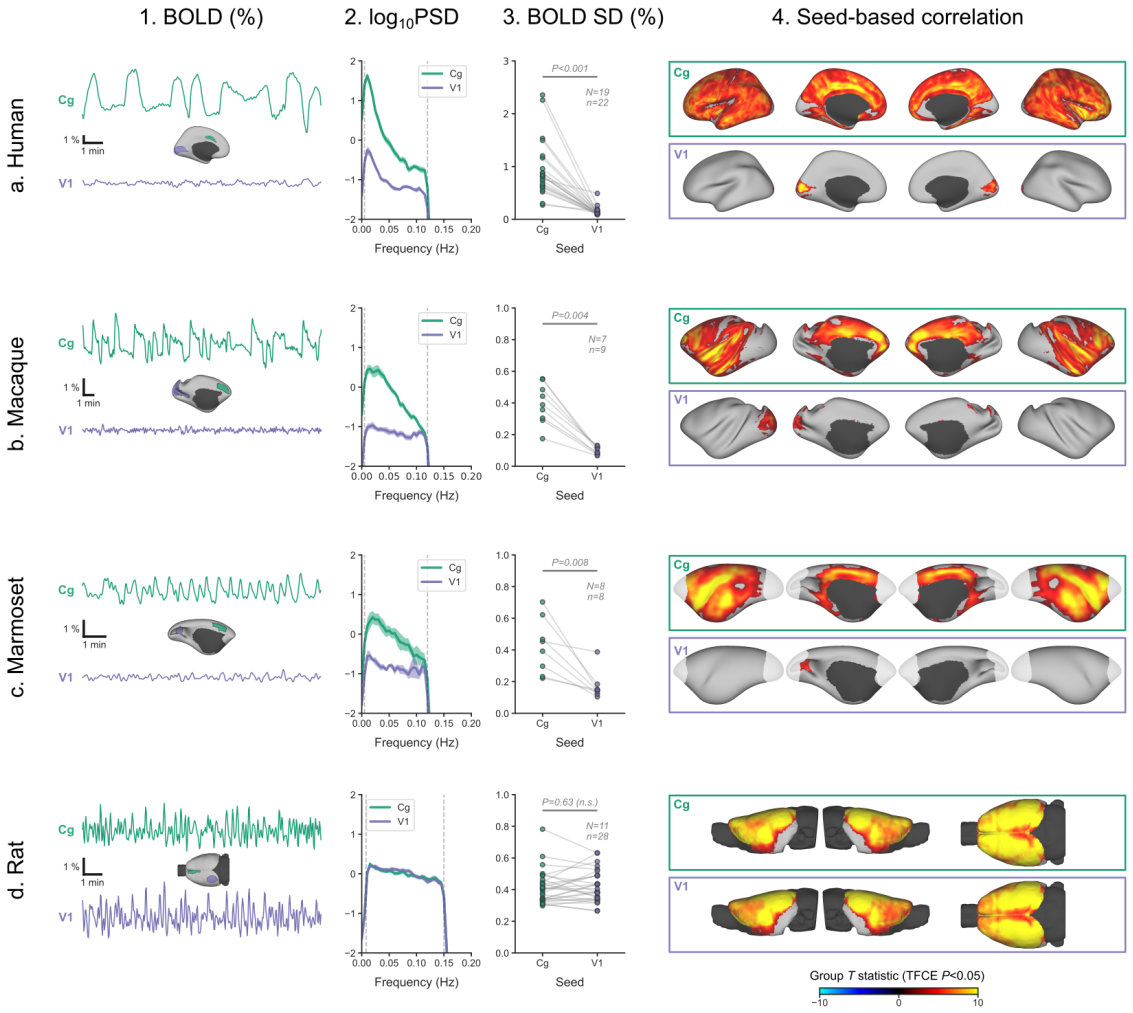

Figure 3.6: The primate V1 is uncoupled from the rest of the cortex during burst-suppression. **a.** BOLD signal timeseries extracted from two regions-of-interest, the cingulate (Cg) area 24cd and the primary visual cortex (V1), are shown for an example human subject during burst-suppression (**a1**). The power spectral density (PSD) of the two regions' timeseries is plotted as mean ± SEM across all fMRI runs with burst-suppression (**a2**). The SD of the timeseries is plotted for the same fMRI runs, as a measure of BOLD signal amplitude (**a3**). The SDs of the two regions are compared using a paired samples two-tailed Wilcoxon rank-sum test (P values given). Panel **a4** shows the results of seed-based correlation analysis—performed for each of the two regions—overlaid on the cortical surface. The group statistics were carried out with FSL randomise; the resulting T statistic maps were thresholded using Threshold-Free Cluster Enhancement (TFCE) and a corrected $P < 0.05$. Panels **b**, **c**, and **d** show the exact same plots as in **a**, but for macaques, marmosets, and rats, respectively. The cingulate (Cg) seed corresponds to the macaque area 24c, the marmoset area 24, and the rat primary cingulate cortex. Marmoset brain areas not covered by the fMRI imaging volume are overlaid with white transparency. The fMRI runs included in the analysis are the ones with an asymmetric PC, as in Figures 3.2, 3.3, 3.4, and 3.5. N: number of subjects; n: number of fMRI runs.

3.2.5 *The primate V1 is uncoupled from the rest of the cortex during burst-suppression*

Our results so far point to a striking difference between primates and rodents: burst-suppression in rats engaged the entire neocortex, while in the three primate species it appeared to leave out certain cortical areas. The most prominent and unambiguous example is V1, which in primates showed no correlation to the asymmetric PCs. This finding cannot be attributed to a fluke of thresholding (see unthresholded T statistic maps in supplementary Figure A.6), or to local signal drop-outs (see temporal signal-to-noise ratio maps in supplementary Figure A.7).

The above prompted us to look more closely at V1 activity and to compare it with an area strongly engaged in burst-suppression. In each of the four species we defined two regions-of-interest—one in V1 and another in the cingulate cortex (Brodmann area 24 in primates, primary cingulate cortex in rats)—and extracted their mean BOLD signal timeseries from fMRI runs previously identified as burst-suppression. We then computed the standard deviation (SD) of the timeseries, as a measure of BOLD signal amplitude, and its power spectral density (PSD). We also performed seed-based correlation analysis using the extracted timeseries as GLM regressors. The results are shown in Figure 3.6 across species. As expected, the chosen cingulate area exhibited the same bistable fluctuation as the asymmetric PCs and its seed-based correlation map was identical to the asymmetric PC maps reported above. The rat V1 activity was indistinguishable from that of the rat cingulate area across all metrics: BOLD signal amplitude ($P = 0.63$, paired samples two-sided Wilcoxon rank-sum test), PSD, and seed-based correlation map. Conversely, the primate V1 activity was very different from the cingulate: BOLD signal amplitude was reduced ($P < 0.001$ in humans, $P = 0.004$ in macaques, $P = 0.008$ in marmosets; paired samples two-sided Wilcoxon rank-sum test), PSD was lower across all frequencies, and seed-based correlation maps were confined to the V1 itself, barely extending beyond the seed borders.

We can conceive three possible mechanisms for the apparent uncoupling of V1 from the rest of the cortex: V1 is engaged in continuous slow waves without suppressions, it is in constant suppression, or there is a local change in neurovascular coupling. Lacking invasive neural recordings, we cannot dissect these possibilities with certainty. Nevertheless, we tried to get a hint from the human data, by examining whether V1 activity differs between the EEG-defined states of burst-suppression and continuous slow waves. We focused on 12 human subjects, in which the EEG showed clear burst-suppression at the high sevoflurane dose (3.9–4.6%), and continuous slow waves at both the intermediate (3%) and the low (2%) sevoflurane doses. For each of the V1 and cingulate seeds, we examined the effects of sevoflurane dose on BOLD signal amplitude and PSD. The detailed results are presented in supplementary Figure A.8 and supplementary Tables A.1 and A.2. In summary, V1 activity during the high (burst-suppression) and intermediate doses was identical in terms of BOLD signal amplitude and low-frequency power (0.005–0.05 Hz), but the high-frequency power (0.05–0.12 Hz) was slightly reduced for the high dose. We deem these results inconclusive: if we assume the presence of continuous slow waves in V1 during the intermediate dose, the small reduction in high-frequency power could represent either a change in slow wave content or a complete suppression of slow-wave

activity. Moreover, a localized change in neurovascular coupling cannot be ruled out with the current data.

3.3 DISCUSSION

In this study we identified the fMRI signatures of anesthesia-induced burst-suppression (Figure 3.1) and constructed comparable maps of this activity in four mammalian species: humans (Figure 3.2), macaques (Figure 3.3), marmosets (Figure 3.4), and rats (Figure 3.5). The resulting burst-suppression maps were functionally similar for the three primate species: they involved the striatum and a large part of the neocortex, with some exceptions mostly at unimodal primary areas. The primary visual area (V1) was the most overt exception, appearing entirely decoupled from the rest of the cortex (Figure 3.6). Contrary to primates, burst-suppression in rats was pancortical, including all sensory and motor areas. To put these findings in context, we will expand the discussion in two directions. Firstly, we will examine our method for identifying the fMRI signatures of burst-suppression, considering its limitations, but also its potential applications. Secondly, we will explore the implications of inter-species differences for existing models of burst-suppression and for future translational efforts.

From our analysis of the human EEG-fMRI data, we determined that EEG-defined burst-suppression manifests on fMRI as an 'asymmetric PC', which can be used as this state's fMRI signature (Figure 3.1). The asymmetry here refers to the distribution of correlation coefficients between the PC and cortical voxels and reflects profound cortical synchrony. The threshold for PC asymmetry (median cortex-wide r) is arbitrarily defined, which constitutes a weakness, since the appropriate value is expected to vary depending on animal species, anesthetic agent, and the parameters used for MRI acquisition and preprocessing. To create the animal burst-suppression maps, we conservatively selected only fMRI runs that presented a single clear asymmetric PC candidate (see Figures 3.3, 3.4, and 3.5). We have several reasons to be confident in our selection, despite the manually chosen thresholds. Firstly, the isoflurane dose range at which these asymmetric PCs were detected closely matches previous EEG reports of burst-suppression in macaques (Vincent et al., 2007; Zhang et al., 2019) and rats (Detsch et al., 2002; Liu et al., 2011; Masamoto et al., 2009; Stenroos et al., 2021). In this regard, our findings in rats are especially encouraging, because almost all asymmetric PCs were found at a dose of 2%, less so at 1.5%, and none at 2.5% (Figure 3.5). Secondly, the detected widespread fluctuations cannot be attributed to known non-neural sources, such as physiology or motion. The asymmetric PCs displayed quasi-periodicity (see supplementary Figure A.9) and were overwhelmingly correlated with gray matter areas. Physiological noise related to mechanical ventilation or heartbeat would have been strictly periodic, while motion artifacts are known to distribute along image edges. In summary, all evidence points towards burst-suppression as the underlying cause of the selected asymmetric PCs in the investigated animals, as was the case for humans.

Given the arbitrary threshold limitation, our method should not be viewed as an automated fMRI-based classification of burst-suppression but instead as a heuristic algorithm for identifying this state. Nevertheless, such an algorithm can find applications within the growing animal fMRI community (Mandino et al., 2020; Milham et al., 2020) and

potentially also in clinical settings. Animal fMRI researchers could use the algorithm to screen both existing and new datasets for the presence of burst-suppression—as we did in supplementary Figure A.5. Nonetheless, the generalization of the method to other animal species and anesthetic agents should be done with caution, keeping in mind that the amplitude and duration of bursts vary across anesthetics (Akrawi et al., 1996; Fleischmann et al., 2018). One potential clinical application concerns the management of comatose patients, where burst-suppression is often present—either transiently or throughout (Brenner, 1985; Brown et al., 2010; Cloostermans et al., 2012; Hofmeijer et al., 2014; Young, 2000). After appropriate validation, our method could allow for the mapping of burst-suppression in these patients, even at centers lacking the capacity for simultaneous EEG-fMRI recordings. An fMRI readout of burst-suppression, with its high spatial resolution and whole-brain coverage, could provide clinicians with information inaccessible by EEG. That said, the interpretation of the additional information and its implications for the prognosis and management of comatose patients are yet to be examined.

How do our maps fit what we know about the spatial distribution of burst-suppression? The apparent exclusion of V1 replicates the previous analysis of the human dataset (Golkowski et al., 2017) and corroborates an existing report in macaques (Zhang et al., 2019). Still, our macaque map constitutes an important generalization, as it is based on seven long-tailed macaques—compared to only two Rhesus individuals in the previous study. The marmoset burst-suppression map is, to our knowledge, the first of its kind and suggests that V1 exclusion may be a general primate feature. The pancortical distribution of burst-suppression in rats agrees with all previous findings in this species, by fMRI (Aedo-Jury et al., 2020; Liu et al., 2011; Paasonen et al., 2020; Schwalm et al., 2017) or calcium imaging (Ming et al., 2021). The strength of our approach lies in computing all maps with the same data-driven approach, thus allowing us to make direct cross-species comparisons.

The main inter-species difference is the exclusion of visual areas (and parts of other unimodal cortices) in primates, but not in rats. While bursts were traditionally viewed as synchronous cortex-wide events, recent work rather describes them as complex waves (Bojak et al., 2015) emerging from a spatially shifting focus and rapidly spreading through the cortex (Ming et al., 2021). Electrocortical recordings in propofol-anesthetized human patients revealed that some electrode channels could display continuous slow waves while others engaged in burst-suppression (Lewis et al., 2013). Taken together with our results, this implies that brain areas may vary in their propensity for generating and/or propagating bursts. Regional metabolic differences could be a potential source of such variability, according to a proposed neurophysiological-metabolic model of burst-suppression (Ching et al., 2012). This model posits that suppressions occur when metabolic resources can no longer sustain neuronal firing, whereas bursts constitute transient recoveries of activity—enabled by slow metabolic replenishment. The primate visual cortex could impose special metabolic demands and thus find itself at an extreme end of the spectrum for burst propensity. Such special demands could arise from its many distinctive characteristics—including cytoarchitecture, neurotransmitter receptor expression (Froudist-Walsh et al., 2021), functional connectivity profile (Margulies et al., 2016), and cortical myelin density (Van Essen et al., 2019). Cortical myelin in particular is suspected to play a role, considering that many areas excluded from our primate burst-suppression maps—V1, MT,

primary motor, and somatosensory cortices—are among the richest in myelin (Van Essen et al., 2019). Conversely, rodents exhibit a more uniform myelin distribution (Fulcher et al., 2019), which could translate in a likewise uniform propensity for bursting.

Whatever the cause, the non-correlation of V1 and other primary sensory areas with burst-suppression challenges existing ideas about the origin of bursts. Studies in isoflurane-anesthetized humans, cats, rats, and mice showed that bursts can be evoked by incoming sensory stimuli, including flashes of light (Hartikainen et al., 1995; Hudetz and Imas, 2007; Kroeger and Amzica, 2007; Land et al., 2012). Consequently, burst-suppression has been thought of as a state of cortical hypersensitivity, during which even subliminal sensory stimuli can trigger a burst excitation (Kroeger and Amzica, 2007). In that case, bursts would be expected to originate at the stimulated sensory area and then spread throughout the cortex indiscriminately, like ripples on a pond (Muller et al., 2018; Sanchez-Vives et al., 2017; Schwalm et al., 2017; Stroh et al., 2013). The pancortical rodent map is fully compatible with this view, but the exclusion of sensory areas in primates seems paradoxical: why would the areas of origin not partake in the ripple? A possible explanation is that the bursts captured in our data were internally generated or evoked through a non-excluded sensory modality (e.g., the bursts in nonhuman primates could be auditorily evoked, given the inclusion of A1 in the map). Nevertheless, a closer investigation of sensory-evoked bursts in primates would be warranted—especially with visual stimuli.

So far, we have focused on cortical aspects of burst-suppression, but fMRI also offers access to subcortical structures (see supplementary Figures A.2 and A.3). Among these, the striatum displayed the strongest correlation with burst-suppression across all four species—showing that the cortex does not act in isolation. Cortico-striatal loops may play an important—but yet unexplored—role in burst propagation. The thalamus, on the contrary, was only partly correlated with burst-suppression, and to a varying extent across species. As a general trend, anteromedial parts were more likely to be involved than posterolateral parts. This may reflect a differential role played by thalamic primary relay centers and higher-order nuclei, as previously hypothesized (Ming et al., 2021). Regional variations in thalamic activity could even shape cortical differences, since the thalamus has been shown to be important for driving burst onsets (Ming et al., 2021; Steriade et al., 1994). Similar to the thalamus, the hippocampus and amygdala were only in parts correlated with burst-suppression. That said, we will refrain from conclusions, since these structures in primates are located in low signal-to-noise areas and often suffer from susceptibility-induced distortions (see supplementary Figure A.7). The cerebellum also suffered from low signal-to-noise in our nonhuman primate data and was only partly captured in marmosets and rats. Nevertheless, the non-correlation of the cerebellar cortex with burst-suppression is likely a true effect, given its consistency across all four species.

Before closing, we wish to address a potentially confusing issue of terminology. We employ the term 'burst-suppression', which is preferred by clinical anesthesiologists. It has been pointed out (Ming et al., 2021) that several rodent studies may refer to the same phenomenon as 'slow oscillation' (Aedo-Jury et al., 2020; Sanchez-Vives et al., 2017; Schwalm et al., 2017; Stroh et al., 2013)—meaning a < 1 Hz alternation between a depolarized 'UP' state of persistent neural activity and a hyperpolarized 'DOWN' state of neural silence (Steriade et al., 1993). In the 'slow oscillation' context, suppressions can be viewed as prolonged DOWN states (Ching et al., 2012; Kroeger and Amzica, 2007). However,

the line between the two is blurry—given the gradual dose-dependent lengthening of quiescent periods. This distinction is even harder if one considers potential inter-species differences in the timescale of burst-suppression. We noticed that bursts and suppressions alternate faster when moving from humans to nonhuman primates to rats (supplementary Figure A.9). Within the framework of the aforementioned neurophysiological-metabolic model of burst-suppression (Ching et al., 2012), such differences in timescale could reflect the faster metabolic rate of smaller animals. Verifying this hypothesis would require further studies involving direct neural recordings.

Summing up, our findings in primates oppose the view of bursts as global cortical events and imply a varying propensity of brain regions to generate and/or propagate bursts. By contrast, burst-suppression in rats appears to be pancortical—prompting an investigation into the cause of this primate-rodent difference and raising questions about the validity of rodent models for anesthesia and coma. Addressing these issues will necessitate invasive neural recordings during burst-suppression, in both primates and rodents, with V1 being the most interesting target area. Our findings also point towards several other promising research directions: clarifying the exact relationship between spontaneous and sensory-evoked bursts, investigating the role of the striatum and thalamus, and examining inter-species differences in the timescale of burst-suppression.

3.4 METHODS

3.4.1 *Experimental subjects and anesthesia*

Five datasets from three research sites were used for this manuscript (see Table 3.1). The human data were obtained from a previous study and have been described in two other articles (Golkowski et al., 2017; Ranft et al., 2016). Experimental details on the second rat dataset have also been presented elsewhere (Rat 2, Paasonen et al., 2016, 2018). All other experiments were carried out at the German Primate Center (Deutsches Primatenzentrum GmbH, Göttingen, Germany) with the approval of the ethics committee of the Lower Saxony State Office for Consumer Protection and Food Safety and in accordance with the guidelines from Directive 2010/63/EU of the European Parliament on the protection of animals used for scientific purposes. The relevant approval numbers are: 33.19-42502-04-16/2278 (Macaque), 33.19-42502-04-17/2496 (Marmoset), 33.19-42502-04-15/2042 (Rat 1).

HUMAN The human EEG-fMRI data were acquired in 20 healthy adult men aged 20–36 years (mean 26). Anesthesia was induced by delivering a gradually increasing concentration of sevoflurane through a tight-fitting face mask. When clinically indicated, a laryngeal mask was inserted, and mechanical ventilation was started. Following that, sevoflurane concentration was increased until the EEG showed suppression about 50% of the time, with suppression periods lasting at least 1 s (reached at end-tidal concentrations of 3.9–4.6%). At this point, 700 s of simultaneous EEG-fMRI were recorded. This recording was repeated at two lower fixed doses, 3% and 2%, each following an equilibration period of 15 min. The lowest dose recording was only acquired in 15/20 participants.

MACAQUE The macaque study included 15 female long-tailed macaques (*Macaca fascicularis*) in total, but fMRI data of sufficient duration (minimum 10 min) and quality were obtained only in 13/15. The macaques varied widely in age (6.8–19.8 years, mean 13.7) and weight (3.6–8.1 kg, mean 5.4). Prior to the imaging session, the animals were given no food for six hours and no water for two hours. Anesthesia was induced with an i.m. injection of ketamine (3–10 mg/kg, Ketamin 10%, Medistar) and medetomidine (0.015–0.03 mg/kg, Dorbene vet 1 mg/ml, Zoetis). The animals were intubated using an endotracheal tube and placed in a sphinx position inside a custom-made MRI-compatible stereotaxic frame to minimize movement artifacts. The ear bars also served as hearing protection and were dabbed with a lidocaine-containing ointment (EMLA 5%, AstraZeneca) for local anesthesia. Temperature was maintained constant at 37°C ± 1°C with the help of a circulating water system. Monitoring equipment was attached, including a pulse oximeter (NONIN model 7500FO, SANIMED GmbH, Germany), a respiratory belt, MRI-compatible surface electrodes for electrocardiogram (CONMED Deutschland GmbH, Germany), and an anesthetic gas analyzer (Philips M1026A Anesthesia Gas Module) for measuring CO_2 and isoflurane concentrations. Throughout the imaging session, the animals were mechanically ventilated with a respirator (Siemens-Elema AB SV 900C Servo Ventilator) at a rate of 8–14 bpm, and anesthesia was maintained with isoflurane, with the dose being continually adjusted to ensure physiological stability. The goal was to sustain an anesthetized depth that would ensure endotracheal tube toleration. The needed end-tidal isoflurane concentrations varied between 0.9–2% across animals. Each imaging session lasted for up to five hours, during which multiple structural MRI contrasts were acquired, as well as task-free BOLD fMRI (one or two runs per animal, each lasting 600–1200 s). During fMRI acquisition, end-tidal isoflurane doses ranged 0.95–1.5% across animals. At the end of the imaging session isoflurane was stopped and the macaques were extubated as soon as spontaneous breathing was safely established.

MARMOSET The marmoset study included a total of 35 common marmosets (*Callithrix jacchus*) of both sexes, but BOLD fMRI data was only obtained in 20 of those (10 females). The animals varied widely in age (1.9–14.2 years, mean 6.1) and weight (337–517 g, mean 407). Anesthesia was induced with a mixture of alfaxalone (12 mg/kg) and diazepam (3 mg/kg) injected i.m. This was followed by 0.05 ml glycopyrronium bromide per animal (Robinul 0.2 mg/ml, Riemser Biosyn) to prevent secretions, maropitant (1 mg/kg, Cerenia, Pfizer) as an antiemetic, and meloxicam (0.2 mg/kg, Metacam, Boehringer Ingelheim) as an anti-inflammatory analgesic. The animals were intubated using a custom-made flexible endotracheal tube and mechanically ventilated at a rate of 35–37 bpm (Animal Respirator Advanced 4601-2; TSE Systems GmbH, Bad Homburg, Germany). The marmosets were placed in a prone position inside a custom-built MRI-compatible bed equipped with a bite bar and ear bars. The ear bars also served as hearing protection and were dabbed with a lidocaine-containing ointment (EMLA 5%, AstraZeneca) for local anesthesia. Eye ointment (Bepanthen, Bayer) was applied for corneal protection. Monitoring equipment consisted of a rectal temperature probe, a pneumatic pressure sensor placed on the chest, and three surface electrodes for ECG (MR-compatible Model 1030 monitoring and gating system; Small Animal Instruments Inc., Stony Brook, NY 11790, USA). Rectal temperature was kept within 36.5 ± 1°C using a pad heated by circulating water. Anesthesia was main-

tained with isoflurane delivered via the respirator, using a mixture of medical air/O_2 (1:1 ratio) as the carrier gas. The isoflurane concentration was adjusted individually for each animal, ranging 0.6–1.1%, in order to maintain stable anesthesia and physiology. Each imaging session lasted for up to five hours, during which multiple structural MRI contrasts were acquired, as well as one task-free fMRI run lasting 600 s. At the end of the session isoflurane was stopped, and the marmosets were extubated as soon as spontaneous breathing was safely established.

RAT 1 The Rat 1 dataset included 11 female adult Wistar rats (Charles Rivers Laboratories, Sulzfeld, Germany), weighing 350–450 g (mean 398). The rats were group-housed in cages with environmental enrichment, at a 12/12-hour light/dark cycle, with 20–24 °C temperature and 45–55% humidity. Water and standard chow were provided ad libitum. Anesthesia was induced in a chamber with 5% isoflurane in 100% O_2. After the loss of the righting reflex, isoflurane was reduced to 2–3% and delivered through a nose cone. The rats were then intubated using a custom-made flexible tracheal tube and mechanically ventilated at a rate of 30 bpm (Animal Respirator Advanced 4601-2; TSE Systems GmbH, Bad Homburg, Germany). Isoflurane was stabilized at 2%, using medical air/O_2 mixture (1:1 ratio) as the carrier gas. The animals were fixed inside a custom-built MRI-compatible rat holder in a supine position (Sirmpilatze et al., 2019) and eye ointment (Bepanthen, Bayer) was applied for corneal protection. Monitoring equipment was attached, consisting of a rectal temperature probe, a pneumatic pressure sensor placed on the chest, and three subcutaneous needle electrodes for ECG (MR-compatible Model 1030 monitoring and gating system; Small Animal Instruments Inc., Stony Brook, NY 11790, USA). Rectal temperature was kept within 36.5 ± 1°C using a pad heated by circulating water. The rat was placed at the isocenter of the MRI system and structural MRI data were acquired. These were followed by three task-free fMRI runs, each 360 s long. After that, isoflurane was either decreased to 1.5% (6/11 animals) or increased to 2.5% (5/11 animals). Following an equilibration period of 30 min, three additional task-free fMRI runs were acquired (six runs per animal in total). In one rat only four fMRI runs could be obtained, due to an early interruption of the imaging session (disconnection of the endotracheal tube). At the end of the imaging session isoflurane was stopped and the rats were extubated as soon as spontaneous breathing had recovered.

RAT 2 The six adult male Wistar rats included in the Rat 2 dataset weighed 265–350 g (mean 307). Briefly, anesthesia was induced with isoflurane 5%, maintained at 2% during animal preparation, and at 1.3% during imaging. The rats were endotracheally intubated and mechanically ventilated, with N_2:O_2 70:30 mixture being used as the carrier gas. The data analyzed for this study comprised a single 300 s run of task-free fMRI per animal.

3.4.2 *MRI acquisition*

HUMAN Human data were acquired on a 3 T whole-body MRI system (Achieva Quasar Dual 3.0 T 16CH, Amsterdam, Netherlands) with an 8-channel phased-array head coil. fMRI data were collected using a gradient-echo echo planar imaging (EPI) sequence with the following parameters: repetition time 2 s, echo time 30 ms, flip angle 75°, field of view

220 x 220 mm^2, matrix size 96 x 96 (in-plane resolution of 2.3 x 2.3 mm^2), 35 axial slices with 3 mm thickness and 1 mm interslice gap, acquisition time 700 s (350 volumes). A 1 mm isotropic T1-weighted image was acquired before the fMRI runs to serve as each subject's anatomical reference.

MACAQUE Macaque data were acquired on a 3 T whole-body MRI system (Siemens MAGNETOM Prisma 3 T, Siemens Healthcare GmbH, Erlangen, Germany). The body coil was used for signal transmission and the 70 mm loop coil for reception. fMRI data were collected using a gradient-echo EPI sequence with the following parameters: repetition time 2 s, echo time 27 ms, flip angle 90°, field of view 96 x 96 mm^2, matrix size 80 x 80 (in-plane resolution of 1.2 x 1.2 mm^2), 33 contiguous axial slices with 1.2 mm thickness, acquisition time 600–1200 s (300–600 volumes). For anatomical reference, a 0.5 mm isotropic T1-weighted image was collected using the MPRAGE sequence with the following parameters: 2 averages, repetition time 2.7 s, inversion time 850 ms, echo time 2.76 ms, flip angle 8°, field of view 12.8 x 10.8 cm^2, matrix size 256 x 216, 192 contiguous axial slices with 0.5 mm thickness.

MARMOSET Marmoset data were acquired on a 9.4 T Bruker BioSpec MRI system, equipped with the B-GA 20S gradient, and operated via ParaVision 6.0.1 software (Bruker BioSpin MRI GmbH, Ettlingen, Germany). Signal was transmitted with a volume resonator (inner diameter 154 mm, Bruker BioSpin MRI GmbH) and received with a 40 mm loop coil (Rapid Biomedical GmbH, Rimpar, Germany). A field map was measured, and shims were adjusted to ensure homogeneity in an ellipsoidal volume within the marmoset brain (MAPSHIM). fMRI data were collected using a gradient-echo EPI sequence with the following parameters: repetition time 2 s, echo time 18 ms, flip angle 90°, field of view 62.4 x 25.6 mm^2, matrix size 156 x 64 (in-plane resolution of 0.4 x 0.4 mm^2), 30 contiguous coronal slices with 0.8 mm thickness, acquisition time 600 s (300 volumes). The slices did not cover the entire brain in the rostro-caudal direction: they extended approximately from the anterior end of the corpus callosum to the middle of the cerebellum (see fMRI coverage in Figure 3.4). For anatomical reference, we used a 0.21 mm isotropic magnetization transfer (MT)-weighted image, acquired using a 3D Fast Low Angle Shot (FLASH) sequence with the following parameters: 2 averages, repetition time 16.1 ms, echo time 3.8 ms, flip angle 5°, field of view 37.8 x 37.8 x 37.8 mm^3, matrix size 180 x 180 x 180.

RAT 1 Rat data were acquired on a 9.4 T Bruker BioSpec MRI system, equipped with the B-GA 12S2 gradient, and operated via ParaVision 6.0.1 software (Bruker BioSpin MRI GmbH, Ettlingen, Germany). Signal was transmitted with a volume resonator (inner diameter 86 mm) and received with a rat brain 4-channel quadrature surface coil (both from Bruker BioSpin). A field map was measured, and shims were adjusted to ensure homogeneity in an ellipsoidal volume within the rat brain (MAPSHIM). fMRI data were collected using a gradient-echo EPI sequence with the following parameters: repetition time 2 s, echo time 15 ms, flip angle 70°, field of view 25.6 x 19.2 mm^2, matrix size 128 x 96 (in-plane resolution of 0.2 x 0.2 mm^2), 40 contiguous coronal slices with 0.5 mm thickness, acquisition time 720 s (360 volumes). The fMRI slices covered the entire rat brain, excluding the olfactory bulbs and the caudal 1/4 of the cerebellum (see fMRI coverage

in Figure 3.5). For anatomical reference, a T2-weighted image was acquired using the TurboRARE (rapid acquisition with relaxation enhancement) sequence with the following parameters: 2 averages, RARE factor 8, repetition time 6.275 s, effective echo time 40 ms, flip angle 90°, field of view 32 x 32 mm^2, matrix size 256 x 256 (in-plane resolution 0.125 x 0.125 mm^2), 50 contiguous coronal slices with 0.5 mm thickness.

RAT 2 Data were acquired on a 7 T Bruker Pharmascan MRI system, operated via ParaVision 5.1 software (Bruker BioSpin MRI GmbH, Ettlingen, Germany). Signal was transmitted with a volume resonator (inner diameter 72 mm) and received with a rat brain 4-channel quadrature surface coil (both from Bruker BioSpin). fMRI data were collected using a spin-echo EPI sequence with the following parameters: repetition time 2 s, echo time 45 ms, field of view 25 x 25 mm^2, matrix size 64 x 64 (in-plane resolution of 0.39 x 0.39 mm^2), 9 contiguous coronal slices with 1.5 mm thickness, acquisition time 600 s (300 volumes). The fMRI slices were placed from the posterior end of the olfactory bulb to the anterior end of the cerebellum (see fMRI coverage in supplementary Figure A.5).

3.4.3 *MRI preprocessing*

To facilitate inter-species comparability, we aimed for harmonizing preprocessing across datasets. The fMRI preprocessing steps were kept the same, but their parameters were adapted to each dataset. We used functions from multiple freely available neuroimaging toolkits, including ANTs v2.1.0 (Advanced Normalization Tools, Avants et al., 2011), FSL v5.0.1 (FMRIB Software Library, Jenkinson et al., 2012), AFNI v18.2.06 (Cox, 1996), Freesurfer v6.0.0 (Fischl, 2012), and Connectome Workbench v1.4.2 (Marcus et al., 2011). Functions from these toolkits were combined into pipelines using the Nipype v1.2 framework (Gorgolewski et al., 2011). The exact steps and functions used will be presented in detail for each dataset. We will also describe the species-specific standard coordinate spaces (templates) and atlases (parcellations) that were used for group analysis and data visualization.

TEMPLATES & ATLASES For human data, we used the MNI152 template (MNI-ICBM average of 152 T1-weighted MRI scans, nonlinear 6^{th} generation, distributed with FSL v5.0.1, Grabner et al., 2006) as the standard coordinate system. For visualization purposes, results were resampled from the MNI152 volumetric space to the fsaverage surface template (part of Freesurfer v6.0.0, Fischl et al., 1999) using the registration-fusion approach (RF-ANTS, Wu et al., 2018). Cortical regions-of-interest were taken from the Human Connectome Project multi-modal parcellation 1.0 (Glasser et al., 2016) and transformed to the MNI152 and fsaverage spaces. Subcortical regions were defined based on the Harvard-Oxford subcortical structural atlas (distributed with FSL v5.0.1). For marmoset data, we used the NIH v3.0 population template as a standard coordinate system (Liu et al., 2021). The volumetric results were visualized on the template's cortical surface (Connectome Workbench *volume-to-surface-mapping*, ribbon-constrained method). Regions-of-interest were taken from the Marmoset Brain Mapping V1 MRI-based parcellation (Liu et al., 2018). For the macaque and rat data, we built our own study-specific volumetric templates, using a validated template creation process implemented in ANTs (Avants et

al., 2010). This process relies on iterative nonlinear registration to produce an unbiased average of the population. Our workflow was constructed similarly to the NMT template of the rhesus macaque (Seidlitz et al., 2018). For each species, the anatomical images (T1-weighted for macaques, T2-weighted for rats) were corrected for variations in image intensity (ANTs *N4BiasFieldCorrection*, Tustison et al., 2010) and rigidly aligned using ANTs (*antsRegistration*). The voxel-wise average of the rigidly aligned images served as the initial target for the iterative template creation process (ANTs *buildtemplateparallel.sh*). The resulting template images were segmented semi-manually with ITK-SNAP (Yushkevich et al., 2006) to create masks for brain and cortex. Macaque regions-of-interest were defined based on the cortical hierarchical (CHARM, Jung et al., 2021) and subcortical (SARM, Hartig et al., 2021) atlases of the rhesus macaque, which were transformed from the NMT v2 space to our macaque template space. Rat regions-of-interest were based on the SIGMA rat brain atlas (Barrière et al., 2019) and were transformed from the SIGMA space. We reconstructed the study-specific macaque template's cortical surface (white matter and pial) using the precon_all pipeline and resampled the volumetric results to it (Connectome Workbench *volume-to-surface-mapping*, ribbon-constrained method). The rat brain surface was reconstructed by extracting the isosurface of the brain mask (Freesurfer) and smoothing it (Connectome Workbench). For representing volumetric results on the rat cortical surface, we adapted a method previously used for the mouse brain (Huntenburg et al., 2021). In short, we first computed the surface normals, i.e. vectors perpendicular to each face of the surface mesh. We then generated line segments along those normals, with each segment stretching from the inner edge of the cortical mask towards the pial surface. Finally, we averaged the cortical voxels overlapping with each of these line segments and assigned their mean value to the corresponding surface point.

HUMAN MRI images were converted from PAR/REC to NIfTI (Neuroimaging Informatics Technology Initiative) format using *dcm2niix* v1.0 (Li et al., 2016). Structural T1-weigthed images were processed using Freesurfer's *recon-all* command, which includes brain extraction and segmentation. The extracted brains were registered to the MNI152 template using linear transforms (*antsRegistration* affine, 12 degrees of freedom), followed by nonlinear symmetric diffeomorphic registration (*antsRegistration* SyN, Avants et al., 2008). The fMRI timeseries were corrected for slice-timing (FSL *slicetimer*) and motion (FSL *MCFLIRT*), and the brain was extracted (FSL *BET*). Polynomial trends were removed up to the 3rd degree, the timeseries were bandpass filtered at 0.005–0.12 Hz, and spatially smoothed using a 3D gaussian kernel with full-width-at-half-maximum (FWHM) of 4 mm (AFNI *3dTProject*). A rigid transformation matrix was calculated between the mean brain-extracted fMRI image and the brain-extracted structural image of the same subject (*antsRegistration*). The matrix was combined with the previously calculated structural-to-template transforms into a composite warp file, which was used to resample the preprocessed fMRI timeseries into the template space, at 2 mm isotropic resolution (*antsApplyTransforms*).

MACAQUE MRI images were converted from DICOM to NIfTI format (*dcm2niix*) and rotated from the sphinx into standard orientation. Structural T1-weighted images were corrected for intensity inhomogeneities (ANTs *N4BiasFieldCorrection*) and registered to

the study-specific macaque template (*antsRegistration* affine, followed by SyN). The template's brain mask was transformed back to the single-subject structural space and the brain was extracted. The fMRI timeseries were corrected for slice-timing (FSL *slicetimer*) and motion (FSL *MCFLIRT*), and the brain was extracted semi-manually with ITK-SNAP. Polynomial trends were removed up to the 3rd degree, the timeseries were bandpass filtered at 0.005–0.12 Hz, and spatially smoothed using a 3D gaussian kernel with FWHM of 2 mm (AFNI *3dTProject*). The mean brain-extracted fMRI image was rigidly registered to the same subject's structural brain image (*antsRegistration*). The resulting transformation matrix was combined with the previously calculated structural-to-template transforms into a composite warp file, which was used to resample the preprocessed fMRI timeseries into the template space, at 1 mm isotropic resolution (*antsApplyTransforms*).

MARMOSET MRI images were exported from ParaVision 6.0.1 to DICOM format, converted from DICOM to NIfTI (*dcm2niix*), and rotated into standard orientation. Structural images (MT-weighted) were corrected for intensity inhomogeneities (ANTs *N4BiasFieldCorrection*) and registered to the T2-weighted image of the NIH v3.0 population template (*antsRegistration* affine, followed by SyN). The fMRI timeseries were corrected for slice-timing (FSL *slicetimer*) and motion (*antsMotionCorr*). Polynomial trends were removed up to the 3rd degree, the timeseries were bandpass filtered at 0.005–0.12 Hz, and spatially smoothed using a 3D gaussian kernel with FWHM of 1 mm (AFNI *3dTProject*). The mean fMRI image was rigidly registered to the subject's structural image (*antsRegistration*). The resulting transformation matrix was combined with the previously calculated structural-to-template transforms into a composite warp file, which was used to resample the preprocessed fMRI timeseries into the template space, at 0.4 mm isotropic resolution (*antsApplyTransforms*).

RAT The rat preprocessing pipeline was identical to the one used for marmosets, with a few differences. The registration target for structural T2-weighted images was our study-specific rat brain template. The 3D gaussian kernel's FWHM was set to 0.6 mm and the preprocessed fMRI timeseries were resampled into the template space at a resolution of 0.2 x 0.2 x 0.5 mm^3. Bandpass temporal filtering was initially applied using the same cutoffs as for the other species (0.005–0.12 Hz). However, we later realized that bursting activity in rats also occurred at faster timescales (see supplementary Figure A.9) and reanalyzed the data using higher bandpass cutoffs (0.008–0.15 Hz). This gave a richer representation of burst-suppression in the temporal domain, without qualitatively altering the resulting maps.

3.4.4 *Carpet plots and PCA*

This part of the analysis was performed using in-house python code, which we have made publicly available at github.com/niksirbi/pcarpet/. We imported the preprocessed fMRI timeseries into python and computed the mean and standard deviation images across time, as well as their ratio (temporal signal-to-noise ratio, or tSNR). Voxels with tSNR < 15 were omitted from further analysis. We then retained only cortical voxels (using the species-specific cortical masks from the aforementioned templates) and reshaped the data

from 4D to a 2D matrix (voxels x frames), with each voxel timeseries (row) normalized to zero mean and unit variance (z-score). To make global signal fluctuations more apparent on the 2D carpet plot, we reordered the voxels according to decreasing correlation with the mean cortical timeseries (Aquino et al., 2020). We then performed PCA on the carpet matrix using singular value decomposition. We extracted the first five temporal PCs and correlated them with all retained cortical voxels (Pearson's r). If a PCs' cortex-wide median r value was negative, we sign-flipped the PC and its correlation values, to force the PC polarity to match the polarity of BOLD signal fluctuations for most voxels. We visualized the correlation values as heatmaps and as histograms per PC (50 bins between $r = -1$ and $r = 1$). The PCs with cortex-wide median r value above a certain species-specific threshold (human 0.45, macaque 0.15, marmoset 0.22, rat 0.2) were classified as 'asymmetric PCs'. The threshold was selected so that at most one prominent PC would exceed them for each fMRI run, with other PCs far below the threshold (see Figures 3.1, 3.3, 3.4, 3.5, and A.5). A few fMRI runs in the Rat 1 dataset had more than one PC close to or above the threshold and were thus excluded from downstream analysis (Figure 3.5b).

3.4.5 *Correspondence to EEG*

The human EEG acquisition and preprocessing has been described in past manuscripts (Golkowski et al., 2017; Ranft et al., 2016). As reported in Golkowski et al., 2017, fMRI volumes with low EEG power across all frequencies were classified as suppressions and assigned value 0. Non-suppression epochs, which displayed high amplitude activity mainly in the delta band, were designated as bursts and assigned value 1 (see example in Figure 3.1a). This process was performed for all anesthetized EEG-fMRI recordings—not just for the ones acquired with the high sevoflurane dose (as in the previous analysis by Golkowski et al., 2017), which led us to discover that four intermediate-dose recordings also contained suppression epochs. Recordings in which no fMRI volume was dominated by suppressed EEG power were classified as being in a continuous slow wave state.

For runs defined as burst-suppression by EEG, we convolved the boxcar envelope (bursts 1, suppression 0) with a canonical two-gamma hemodynamic response function (Glover, 1999) and applied the same bandpass filter as for fMRI preprocessing (0.005–0.12 Hz, see Figure 3.1b). To compare the resulting EEG-derived hemodynamic model of burst-suppression with the asymmetric PC derived from the simultaneous fMRI recording, we computed their cross-correlation. We extracted each pair's correlation at zero lag, their maximum cross-correlation, and the time lag at which the maximum was achieved. Two runs acquired with the high sevoflurane dose were excluded from the cross-correlation analysis: subject 15 (EEG contained only one short burst and fMRI contained no asymmetric PC) and subject 7 (burst-suppression could be seen on EEG, but part of the recording was corrupted).

3.4.6 *Burst suppression maps*

For each fMRI run with an asymmetric PC, we used the PC as a regressor in a first-level general linear model (GLM) analysis to get its distribution across the brain. The GLM was carried out with FEAT (FMRI Expert Analysis Tool Version 6.00, part of FSL),

using local autocorrelation correction (Woolrich et al., 2001). Resulting Z statistic images were masked for the brain and thresholded non-parametrically using clusters determined by $Z > 3.1$ and a corrected cluster significance threshold of $P = 0.05$ (Worsley, 2001). In the case of the human dataset, we also conducted the same analysis using the EEG-derived hemodynamic models as regressors. We compared the unthresholded Z statistic maps resulting from the two analyses by computing their spatial cross-correlation (ANTs *MeasureImageSimilarity*, neighborhood cross-correlation metric within the brain mask).

For each of the four species, we computed group-level burst-suppression maps using the resulting parameter estimate images from first-level GLMs. For subjects having more than one fMRI run with asymmetric PCs, the images were first averaged within each subject. Subsequently, a non-parametric one sample T-test was computed on the list of subject-level images, using FSL randomise (Winkler et al., 2014) with threshold-free cluster enhancement (TFCE, Smith and Nichols, 2009). The permutation-based randomise algorithm allows for control of false positives with minimal assumptions about the data, while TFCE has the sensitivity benefits of cluster-based thresholding—without the need for arbitrary decisions on cluster-forming thresholds. We thought these advantages to be important, given our goal to compare maps across dissimilar datasets, with varying spatial scales and signal-to-noise ratios. The resulting unthresholded group maps are given in supplementary Figure A.6 across species. Areas with a corrected $P < 0.05$ were judged to be significantly correlated with asymmetric PCs. Significant anti-correlations were computed by repeating the above procedure with a flipped contrast. The thresholded maps are shown in Figures 3.2, 3.3, 3.4, and 3.5. All group statistics were carried out in the species-specific volumetric template spaces. The resampling on cortical surfaces was done for purposes of data visualization only, using the methods described in the *Template and atlases* paragraph.

3.4.7 *Region-of-interest analysis*

We defined two regions-of-interest per species—one in the left V1 and another in the left cingulate cortex (Cg: human area 24cd, macaque area 24c, marmoset area 24, rat primary cingulate cortex; see Figure 3.6). The former was chosen because of its exclusion from primate burst-suppression maps; the latter because of its strong correlation with burst-suppression across species. We extracted each region's average BOLD signal timeseries from all preprocessed fMRI runs with asymmetric PCs and normalized them as percent-signal-change relative to the temporal mean. We quantified the standard deviation (SD) of the normalized timeseries as a measure of BOLD signal amplitude. For each species, we compared the BOLD SD between the two regions using a paired samples two-sided Wilcoxon rank-sum test (jamovi v1.8 statistical software). We also computed the power spectral density (PSD) of the normalized timeseries using Welch's method (as implemented in *scipy.signal.welch*, segments of 100 timepoints, with 50 overlapping points between segments). Finally, each normalized timeseries was used as a regressor in a seed-based GLM analysis. The GLM statistics and thresholding were carried out exactly as described above for burst-suppression maps. A total of 8 seed-based group-level analyses were carried out (4 species x 2 seeds).

In the human dataset, we further examined whether the BOLD signal SD and PSD of the two regions differed significantly between the two EEG-defined states. We focused on 12 human subjects, in which the EEG showed clear burst-suppression at the high sevoflurane dose (3.9–4.6%), and continuous slow waves at both the intermediate (3%) and the low (2%) sevoflurane doses. For each of V1 and cingulate seeds, we examined the effects of sevoflurane dose on three response variables: BOLD signal amplitude (SD), low-frequency $\log_{10}$PSD (integrated between 0.005–0.05 Hz), and high-frequency $\log_{10}$PSD (integrated between 0.05–0.12 Hz). The lower frequency range corresponded to the timescale of burst-suppression in the human dataset. The effect of sevoflurane dose on each of the three response variables was probed with repeated-measures ANOVA (sevoflurane dose as the within-subject repeated-measures factor, jamovi v1.8, see supplementary Table A.1). The Greenhouse-Geisser sphericity correction was applied when needed (Mauchly's sphericity test with $P < 0.05$). In cases of significant ANOVA effects ($P < 0.05$), we performed Tukey post-hoc pairwise comparisons between sevoflurane dose levels (jamovi 1.8, see supplementary Table A.2). Least Squares Means were estimated for the three levels of sevoflurane dose. Results are summarized in supplementary Figure A.8.

4

IN VIVO TWO-PHOTON CALCIUM IMAGING OF THE RAT CORTEX DURING ISOFLURANE-INDUCED BURST-SUPPRESSION.

PEOPLE INVOLVED IN THE STUDY

Nikoloz Sirmpilatze[1,3,4], Philipp Schwedhelm[2], Jessica König[1], Daniel Hillier[2], Vladislav Kozyrev[2], Kristin Kötz[1], Kerstin Fuhrmann[1], Adrienn Volak[6], Josephine Jüttner[6], Stefan Nessler[5], Christine Stadelmann-Nessler[5], Botond Roska[6], and Susann Boretius[1,3,4].

1. Functional Imaging Laboratory, German Primate Center—Leibniz Institute for Primate Research, Göttingen, Germany
2. Junior Research Group Visual Circuits and Repair, German Primate Center—Leibniz Institute for Primate Research, Göttingen, Germany
3. Georg-August University of Göttingen, Göttingen, Germany
4. International Max Planck Research School for Neurosciences, Göttingen, Germany
5. Institute for Neuropathology, University Medical Center, Göttingen, Germany
6. Institute of Molecular and Clinical Ophthalmology, Basel, Switzerland

OWN CONTRIBUTIONS

- Conceptualization and study design (together with PS and SB)
- Data collection:
  - Anesthesia (together with JK, KK, SB)
  - Surgeries (together with JK)
  - Two-photon imaging
- Data analysis
- Data interpretation
- Data visualization
- Writing

ABSTRACT

In Chapter 3 we used fMRI to show that burst-suppression—a pattern of synchronous neural activity appearing during deep anesthesia—was differently distributed in primate and rodent brains. Burst-suppression involved the entire neocortex in rats but appeared to leave out the visual cortex in humans and nonhuman primates. To address the source of this difference, we would need to directly record neural activity in the visual cortex of a primate and a rodent during burst-suppression. We advanced this goal by undertaking methodological development for *in vivo* two-photon calcium imaging in isoflurane-anesthetized animals. In this study we report a series of pilot experiments in rats, in which we evaluated multiple necessary experimental components. We tested viral constructs for expressing genetically-encoded calcium indicators and excitatory opsins in somatosensory and visual areas. We also developed the surgical expertise for implanting chronically stable cranial windows and fiber-optic cannulas. In two animals we successfully recorded from hundreds of layer 2/3 neurons across multiple imaging sessions, for up to 3 months. These recordings captured burst-suppression activity across a range of isoflurane doses in both the somatosensory and the visual cortex. We were also able to evoke bursts through flashes of light and electrical stimulation of the forepaw. In conclusion, we have demonstrated the feasibility of longitudinal *in vivo* two-photon calcium imaging in isoflurane-anesthetized rats. The developed expertise and the acquired preliminary data will enable us to design hypothesis-driven studies of burst-suppression in both rats and marmosets.

4.1 INTRODUCTION

4.1.1 *Motivation*

In Chapter 3 we reported that brain areas involved in burst-suppression during anesthesia differed between primates and rodents. The entire neocortex was correlated with burst-suppression in rats, whereas several cortical areas were uncoupled from this activity in primates. The uncoupled areas largely overlapped with unimodal primary cortices, the primary visual cortex (V1) being the most prominent example. If these primate areas do not follow the rest of the cortex in burst-suppression, what is the nature of their neural activity? Possible answers include a continuous slow wave state or a state of constant suppression. Local disruption of neurovascular coupling is yet another possibility, since it would render neural activity 'invisible' to BOLD fMRI. Limited by the low temporal resolution of fMRI and its reliance on neurovascular coupling, our previous studies (Chapter 3) did not allow us to differentiate between these alternatives.

To answer the above question, we would need to directly record neural activity from the uncoupled areas during the burst-suppression state. Moreover, to address the primate-rodent difference, we must do so in at least two species. Our results from Chapter 3 indicated a suitable pair of candidates—common marmosets and rats. These two species are of comparable body size, and both possess lissencephalic (smooth) cortices. These properties allow us to study them with the same methods, and even the same pieces of equipment. Importantly for our question, the extensive marmoset visual system, which

showed no correlation to burst-suppression, offers an easily accessible target for direct recordings of neural activity (Mitchell and Leopold, 2015).

Apart from determining the nature of V1 activity during burst-suppression, such targeted neural recordings could also address two secondary questions that arose from Chapter 3. The first concerns the role of primary sensory areas in generating sensory-evoked bursts. During burst-suppression even weak sensory stimuli are known to trigger a burst excitation of the cortex (Hartikainen et al., 1995; Hudetz and Imas, 2007; Kroeger and Amzica, 2007; Land et al., 2012). Such sensory-evoked bursts would be expected to originate at the cortical area that first receives the stimulus, and from there spread rapidly throughout the cortex. This view is supported by the existing evidence in rodents (Schwalm et al., 2017; Stroh et al., 2013) but appears to be contradicted by the exclusion of early sensory areas that we found in primates. This apparent paradox could be investigated by recording V1 activity during visually-evoked bursts, in both primates and rodents. The second question concerns the timescale of burst-suppression. In humans, burst and suppression epochs alternate quasi-periodically at an exceptionally slow timescale, with each epoch lasting up to several minutes. According to a neurophysiological-metabolic model of burst-suppression, this alternation is dictated by a depletion-recovery cycle of metabolic resources and thus depends on the cerebral metabolic rate (Ching et al., 2012). In our fMRI data we observed that the alternations occur more frequently in nonhuman primates, and even more so in rats. That said, the observed fMRI timescales also depend on the hemodynamic response function, which may in itself be faster in rodents (Lambers et al., 2020; Silva et al., 2007). Direct neural recordings would allow us to measure the true timescale of the phenomenon and its precise dependency on anesthetic dose. Relating these parameters to the cerebral metabolic rate of each species could provide crucial support for the neurophysiological-metabolic model (Ching et al., 2012).

4.1.2 *Neural recording techniques*

Given the aforementioned aims, we sought a neural recording technique that satisfies the following requirements:

- Can be applied to both rats and marmosets *in vivo*.
- Is suited for longitudinal, repeated-measures experimental designs. For practical and ethical reasons we wish to keep the number of animals, especially marmosets, to a minimum.
- Can achieve sub-second temporal resolution, to accurately measure the duration of burst and suppression epochs (especially in rats).
- Can resolve neural activity at the level of single cells or cortical columns.
- Does not rely on neurovascular coupling.
- Can record multiple neurons simultaneously, to identify the presence of synchrony.

There are broadly two modalities that could satisfy these needs: electrophysiology and calcium imaging. Each of them offers a wide array of possibilities, which we will explore in the next paragraphs.

Among electrophysiological techniques, EEG has historically been the most widely used for measuring burst-suppression—for clinical and research purposes (Kroeger et al., 2013; Young, 2000). However, EEG cannot spatially resolve neural activity at the level of specific cortical areas and lacks spiking information. Intracellular recordings (e.g. patch clamp) permit measuring the membrane potential and have been used for studying the cellular mechanisms of burst-suppression (Steriade et al., 1994). On the flip side, their application in a living animal is challenging and limited to a few cells at a time. Extracellular recordings could be the most promising approach for our needs, for a number of reasons. Firstly, they yield information about both spikes and local field potentials. Secondly, thanks to recent technological advances in multi-electrode arrays (e.g. neuropixel probes), hundreds of neurons can be recorded simultaneously at millisecond timescales (Jun et al., 2017; Steinmetz et al., 2018, 2021). Thirdly, such probes can be chronically implanted and yield data for extended periods of time in both rodents (Daal et al., 2021; Luo et al., 2020) and nonhuman primates (Trautmann et al., 2019).

Calcium imaging, which tracks the intracellular calcium concentration as a proxy for neural activity, has matured into a powerful and popular tool at the forefront of modern neuroscience (Grienberger and Konnerth, 2012). The newest generation of fluorescent calcium indicators offers high sensitivity, fast kinetics, and a variety of excitation and emission wavelengths to choose from (Chen et al., 2013; Dana et al., 2016). The fluorescent signal can be read in various ways, including fiber photometry, widefield imaging, and multiphoton microscopy (Grienberger and Konnerth, 2012). In fiber photometry light is delivered and retrieved through an implanted optical fiber. The acquired fluorescent signal represents the population neural activity from a bulk area adjacent to the implanted fiber (no cellular resolution). The method's advantages include lightweight design, less invasive surgeries, and the ability to be combined with MRI (Albers et al., 2018; Liang et al., 2017; Schwalm et al., 2017). Widefield calcium imaging involves removing a large portion of the skull to image the entire dorsal surface of the cortex. This method is suited for imaging large-scale cortical dynamics in mice (Cramer et al., 2019; Ren and Komiyama, 2021) and has previously been used to study burst-suppression in rats (Ming et al., 2021). However, given the lack of transgenic lines expressing calcium indicators in rats and marmosets, such experiments would necessitate the bulk loading of the entire neocortex with chemical calcium dyes. This procedure as well as the invasiveness of the required skull preparation render this method incompatible with longitudinal study designs. Multiphoton (two- or three-photon) microscopy—through recent innovations in lasers, optics, and surgical protocols—enables recordings from thousands of neurons at sub-second temporal resolution (Lecoq et al., 2019; Stringer et al., 2019). Neural activity can be imaged through a chronically implanted cranial window for up to several months, in both rodents (Koletar et al., 2019; Stringer et al., 2019) and marmosets (Ebina et al., 2018; Sadakane et al., 2015; Santisakultarm et al., 2016). Expression of genetically-encoded calcium indicators (GECIs) under the window can be achieved via targeted stereotaxic injections of viral constructs (Ebina et al., 2018; Grienberger and Konnerth, 2012; Sadakane et al., 2015).

The techniques that can better serve our needs are extracellular electrophysiological recordings via multi-electrode arrays and multi-photon calcium-imaging through chronically implanted cranial windows. We chose the latter approach, due to the local availability of the necessary equipment and expertise. Specifically, the Junior Research Group

'Visual Circuits and Repair', which was established at the German Primate Center in 2019, offered their state-of-the-art two-photon microscope to be used for this study. One of the group's goals is to develop *in vivo* two-photon calcium imaging capabilities in primates. In collaboration with the group's Dr. Philipp Schwedlehm, we designed the current study to demonstrate the feasibility of longitudinal two-photon calcium imaging in isoflurane-anesthetized rats. All materials and methods were selected in a way that would allow their seamless translation to marmosets, at a later stage.

4.1.3 *Stimulus modalities*

To explore our questions about evoked bursts, the current study goes beyond simply recording the spontaneous neural activity under isoflurane anesthesia; it also includes stimulating the brain in various ways. Specifically, we chose three stimulus modalities:

1. Visual stimulation using brief flashes of light; such stimuli are known to evoke bursts in multiple species, with the expected burst origin at V1 (Hartikainen et al., 1995; Hudetz and Imas, 2007; Kroeger and Amzica, 2007; Land et al., 2012; Stroh et al., 2013).
2. Electrical forepaw stimulation (EFS); this is one of the most widely used sensory stimuli in rats, familiar to us from the study in Chapter 2 (Sirmpilatze et al., 2019). Thus, we could gauge the appropriate stimulus intensity and we anticipated the exact location of cortical activation (contralateral forelimb region of the primary somatosensory cortex, S1FL).
3. Optogenetic stimulation of the cortex, which has been used to evoke bursts in mice (Stroh et al., 2013). Unlike sensory stimuli, which first pass through thalamic relay nuclei, optogenetic stimuli are expected to directly excite the cortex. The necessary opsins can be introduced via viral transduction, similarly to calcium indicators.

4.1.4 *Study scope and goals*

The experiments described in this chapter constitute a pilot study. Its overall aim was to develop and test methods for longitudinal *in vivo* two-photon calcium imaging through chronically implanted cranial windows in isoflurane-anesthetized rats. The developed methods and preliminary results will be used to design future hypothesis-driven studies in both rats and marmosets. The pilot study's specific goals were the following:

1. To test an array of viral constructs for expressing GECIs and opsins in the rat neocortex, specifically V1 and S1FL.
2. To develop the surgical expertise for stereotaxic injections as well as for implanting chronically-stable cranial windows and fiber-optic cannulas.
3. To test the two-photon microscope and assess the feasibility of large-scale multicellular recordings *in vivo*.
4. To estimate the timescale of burst-suppression and its dependency on isoflurane dose.

5. To assess the capacity of sensory and optogenetic stimuli to evoke bursts.

4.2 MATERIALS AND METHODS

4.2.1 *Animals*

Seven female adult Wistar rats (Charles Rivers Laboratories, Sulzfeld, Germany) were used in this study, weighing 305–325 g at the start of experiments. The rats were group-housed in cages with environmental enrichment, at a 12/12-hour light/dark cycle, with 20–24 °C temperature and 45–55% humidity. Water and standard chow were provided ad libitum. The experiments were carried out with the approval of the ethics committee of the Lower Saxony State Office for Consumer Protection and Food Safety (approval number 33.19-42502-04-19/3275) and in accordance with the guidelines from Directive 2010/63/EU of the European Parliament on the protection of animals used for scientific purposes.

4.2.2 *Experimental timeline*

In two animals (Rats 1 & 2), we first performed a stereotaxic surgery to inject the viral constructs and followed up one month later with a second surgery for placing the cranial implants (windows and fiber-optic cannulas). Two-photon imaging was initiated one week after the second surgery. We modified the timeline for the other five animals, by performing both the stereotaxic injections and the implant placement in a single surgery and initiating two-photon imaging after a minimum recovery period of two weeks. We planned to perform up to nine imaging sessions, with at least one week between sessions. At the end of the final imaging session the rats were euthanized and transcardially perfused.

4.2.3 *Viral constructs*

The viral constructs were provided by the Complex Viruses Platform, Institute of Molecular and Clinical Ophthalmology in Basel. All constructs were based on the AAV9 vector and were under the control of one of two gene promoters—human synapsin 1 (hSyn) or human elongation factor 1 (EF1a). hSyn is known to drive exclusively neuronal expression (Kügler et al., 2003). EF1a primarily targets neurons but also leads to some astrocytic expression (Tsuchiya et al., 2002). Each vector contained one of five possible payloads: three GECIs and two excitatory opsins. Two of the GECIs emit green light (GCaMP6s, Chen et al., 2013; GCaMP7s, Dana et al., 2019) and the third one red (jRGECO1a, Dana et al., 2016). The two opsins were Channelrhodopsin-2 (ChR2, responding to blue light, peak wavelength ≈470 nm, Nagel et al., 2003; Zhang et al., 2006), and ChrimsonR (responding to amber light, peak wavelength ≈590 nm, Klapoetke et al., 2014). The reason for testing multiple constructs (10 in total: 2 promoters x 5 payloads) in this pilot study was to ultimately select a suitable GECI-opsin combination for future experiments. The ideal GECI-opsin pair should be characterized by minimal optical crosstalk (e.g. GCaMP-

ChrimsonR, or jRGECO1a-ChR2) and a long co-expression time-window (Emiliani et al., 2015). To test the various combinations in the target cortical areas, we distributed the ten constructs among the seven animals, with four injection sites per animal—two in V1 and two in S1FL. The constructs were allocated to the 28 sites such that each construct would be injected at least once in both S1FL and V1 (see Table 4.1). In a few sites we injected saline as a control.

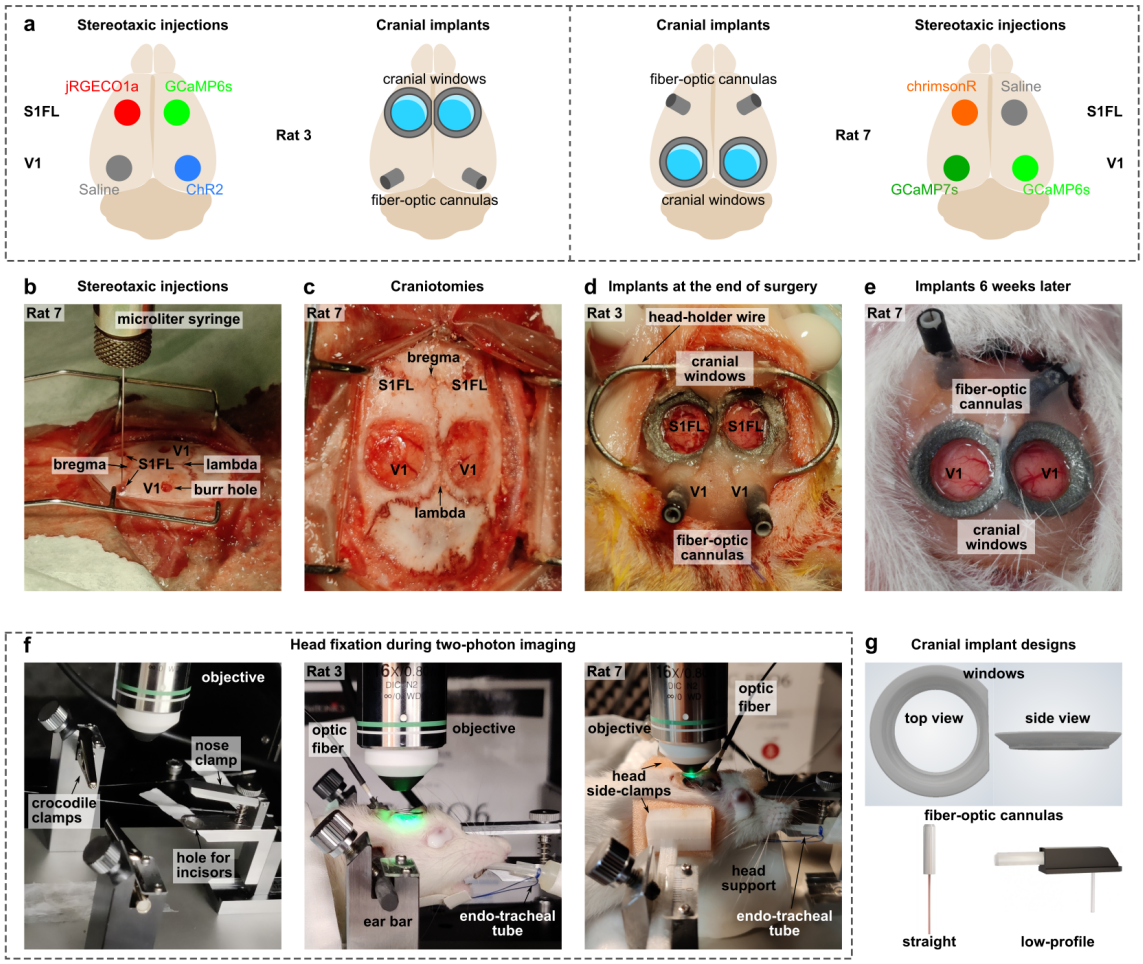

Figure 4.1: Surgeries and cranial implants. The two possible configurations for cranial implants are shown in **a**, using Rats 3 & 7 as examples. In Rat 3 cranial windows were implanted bilaterally over the forelimb region of the primary somatosensory cortex (S1FL), providing access to neurons expressing fluorescent calcium indicators; fiber-optic cannulas were implanted bilaterally in the primary visual cortex (V1), for delivering excitation light to opsin-expressing neurons. The positions of windows and cannulas in Rat 7 were swapped. The designs for the window and fiber-optic cannulas can be seen in **g**. Panels **b–d** show photographs from different phases of the surgery and panel **e** depicts the head implant six weeks after surgery. The various head fixation approaches we employed during two-photon imaging can be seen in **f**.

RAT ID	AREA	SIDE	IMPLANT	VIRAL CONSTRUCT	TITER (GC/ML)
1	S1FL	L	Window	AAV9-hSyn-GCaMP7s	$4.37x10^{15}$
		R	Window	AAV9-hSyn-GCaMP6s	$3.14x10^{14}$
	V1	L	Fiber	AAV9-hSyn-chrimsonR-tdTomato	$5.82x10^{13}$
		R	Fiber	Saline	
2	S1FL	L	Fiber	AAV9-hSyn-chrimsonR-tdTomato	$5.82x10^{13}$
		R	Fiber	Saline	
	V1	L	Window	AAV9-hSyn-GCaMP7s	$4.37x10^{15}$
		R	Window	AAV9-hSyn-GCaMP6s	$3.14x10^{14}$
3	S1FL	L	Window	AAV9-hSyn-jRGECO1a	$1.96x10^{14}$
		R	Window	AAV9-EF1a-GCaMP6s	$1.96x10^{14}$
	V1	L	Fiber	Saline	
		R	Fiber	AAV9-hSyn-ChR2-EGFP	$4.18x10^{13}$
4	S1FL	L	Fiber	Saline	
		R	Fiber	AAV9-hSyn-ChR2-EGFP	$4.18x10^{13}$
	V1	L	Window	AAV9-hSyn-jRGECO1a	$1.96x10^{14}$
		R	Window	AAV9-EF1a-GCaMP6s	$1.96x10^{14}$
5	S1FL	L	Window	AAV9-EF1a-jRGECO1a	$8.26x10^{13}$
		R	Window	AAV9-EF1a-GCaMP7s	$2.25x10^{14}$
	V1	L	Fiber	AAV9-EF1a-chrimsonR-tdTomato	$7.13x10^{13}$
		R	Fiber	AAV9-EF1a-ChR2-EGFP	$4.13x10^{12}$
6	S1FL	L	Fiber	AAV9-EF1a-chrimsonR-tdTomato	$7.13x10^{13}$
		R	Fiber	AAV9-EF1a-ChR2-EGFP	$4.13x10^{12}$
	V1	L	Window	AAV9-EF1a-jRGECO1a	$8.26x10^{13}$
		R	Window	AAV9-EF1a-GCaMP7s	$2.25x10^{14}$
7	S1FL	L	Fiber	AAV9-hSyn-chrimsonR-tdTomato	$5.82x10^{13}$
		R	Fiber	Saline	
	V1	L	Window	AAV9-hSyn-GCaMP7s	$4.37x10^{15}$
		R	Window	AAV9-hSyn-GCaMP6s	$3.14x10^{14}$

Table 4.1: The allocation of viral constructs to injection sites per animal. S1FL: forelimb region of the primary somatosensory cortex; V1: primary visual cortex; L: left; R: right.

4.2.4 *Implants*

Each animal received four cranial implants—one above each injection site. Two of those were cranial windows for providing access to GECI-expressing areas and the other two were fiber-optic cannulas for delivering excitation light to opsin-expressing areas. The four implants were placed in two possible configurations (see Table 4.1): windows above S1FL with fibers above V1 (in Rats 1, 3, & 5) or the other way around (in Rats 2, 4, 6, & 7). Figure 4.1a illustrates both configurations. The cranial windows were designed by Dr. Philipp Schwedhelm and 3D-printed using titanium (Sculpteo, Villejuif, France). They were ring shaped (see Figure 4.1g), with an opening of 6 mm in diameter on the brain-facing side. The diameter widened towards the other side to accommodate the microscope's objective lens. A glass cover slip (also 6 mm in diameter) was fixed on the brain-facing side with superglue. The fiber-optic cannulas were made of borosilicate glass, with a core diameter of 400 µm and NA of 0.66, ending in a conical tip (Doric Lenses Inc., Franquet, Quebec, Canada). The fiber tip length was 2 mm for S1FL and 1.5 mm for V1. Except for the conventional straight cannulas, in some cases we also implanted a low-profile version that bends at 90° immediately after exiting the skull (see Figure 4.1g). We additionally implanted an oval-shaped steel wire (see Figure 4.1d) in 6/7 rats, for fixing the head during imaging ('head-holder wire'). We omitted the wire in Rat 7, for reasons that will become apparent in following sections.

4.2.5 *Surgery*

The surgical protocols were developed and performed together with Dr. Jessica König, whose long-standing experience with stereotaxic surgery was indispensable. The surgical procedure was first trained and iteratively refined on rat cadavers. Further improvements were continually made with each animal. Important deviations in individual rats will be pointed out. Here we will describe the surgical procedure performed in 5/7 rats, combining the stereotaxic injections with the implantation of cranial windows and fiber-optic cannulas. The remaining two animals (Rats 1 & 2) received the stereotaxic injections and the implants in two separate operations, one month apart.

Anesthesia was induced via a combination of medetomidine (0.4 mg/kg, Dorbene vet 1 mg/ml, Zoetis) and ketamine (70 mg/kg, Ketamin 10%, Medistar) delivered i.p. This was followed by s.c. injections of buprenorphine (0.04 mg/kg, Buprenovet 0.3 mg/ml, Bayer Vital) for analgesia, enrofloxacine (7.5 mg/kg, Enrofloxacin 2.5%, WDT) for antibiotic prophylaxis, and glycopyrronium bromide (0.03 ml per animal, Robinul 0.2 mg/ml, Riemser Biosyn) for preventing secretions. The scalp was shaved and a protective ointment (Bepanthen, Bayer) was applied to the eyes. The rats were intubated with a custom-made flexible endo-tracheal tube and fixed in a rat stereotaxic device (Narishige, Japan). The endotracheal tube was connected to a respirator (SAR-100 Small Animal Ventilator, CWE Inc, USA) and mechanical ventilation was performed at a rate of 45–55 bpm. Anesthesia was monitored through capnography (NONIN Respsense II, SANIMED GmbH, Germany) and pulse oximetry (PhysioSuite, Kent Scientific Corporation, USA). Rectal temperature was maintained constant at 37°C using a feedback-controlled heating pad (PhysioSuite, Kent Scientific Corporation, USA). Anesthesia was supplemented with isoflurane, start-

ing at ≈1.5 hours after induction and gradually adjusted from 0.5 to 1.5% by the end of the surgery.

All surgical procedures were done under sterile conditions. The shaved scalp was disinfected using alternating swabs with iodine solution and 70% ethanol. An incision was made at the midline and the scalp was retracted. The upper surface of the skull was scraped clean and swabbed with a 3% hydrogen peroxide solution. Using a stereotaxic micromanipulator (Narishige, Japan), four target points were marked on the skull according to the Paxinos rat brain stereotaxic atlas (Paxinos and Watson, 2007), using the bregma as reference: bilateral S1FL (+0.5 mm anterior, ±3.5 mm lateral) and bilateral V1 (-5.5 mm posterior, ±4 mm lateral). Burr holes (≈1.5 mm in diameter) were drilled at each marked point (High Speed Rotary Micromotor Kit, Foredom Blackstone Industries LLC, USA) without rupturing the dura. A microliter syringe (model CAL87930, Hamilton, USA) was loaded with the allocated viral solution (or saline, see Table 4.1) and inserted in each burr hole until the needle tip touched the dura (see Figure 4.1b). The needle was slowly lowered to the target injection depth: 1 mm below the dura for S1FL, 0.7 mm for V1. Approximately 1 µl of the solution was injected at each target site using a motorized stereotaxic microinjector (model IMS-20, Narishige, Japan). The injection lasted 3 minutes in Rats 1–2 (0.333 µl/min), 6 minutes in Rats 3–4 (0.166 µl/min), and 10 minutes in Rats 5–7 (0.1 µl/min). The needle was left in place additionally for 5–10 minutes to allow for viral vector diffusion and then slowly retracted.

After completing all four stereotaxic injections, two large circular craniotomies (6 mm in diameter) were made using the drill, either above S1FL or above V1 (see Figure 4.1c). Each craniotomy was centered around the corresponding injection site. The skull rim around the craniotomies was thinned to better accommodate the window implants. The dura was carefully removed from the craniotomies and bleedings were stopped by cold saline. After ensuring that the craniotomy was clean and free of bleeding, the windows were lowered into the craniotomies and their circumference was carefully sealed with light-cured dental cement (PANAVIA SA Cement Universal, Kuraray Europe GmbH, Germany). Fiber-optic cannulas were inserted into the remaining two burr holes (after puncturing the dura using a needle tip) and glued to the surrounding bone with a small amount of the light-cured dental cement. Subsequently, the steel wire head-holder was placed around the implants (in 6/7 rats). The entire construction was covered in more dental cement across the exposed dorsal surface of the skull. For this step, we used the same light-cured cement in Rats 1 & 2 but switched to a different one in Rats 3–7 (Paladur, Kulzer GmbH, Germany). The rostral and caudal ends of the skin incision were closed with intracutaneous sutures, ensuring a tight fit of the skin around the cement-covered area (see Figure 4.1d–e).

The entire surgery lasted 5–7 hours. At its end isoflurane was stopped, atipamezole was injected s.c. (0.75 mg/kg, Atipazole 5 mg/ml, Prodivet) to antagonize any remaining medetomidine, and a second dose of buprenorphine (0.04 mg/kg) was given s.c. The animals were disconnected from the respirator and extubated once spontaneous breathing was established. A third dose of buprenorphine (0.04 mg/kg) was administered 6 hours after the end of surgery and fluids were injected s.c. if deemed necessary (1 ml of glucose 5% & 1 ml of Ringer-lactate). The animals recovered overnight in a heated cage. Analgesia was continued over three post-operative days with daily injections of meloxicam (1 mg/kg

s.c., Metacam 5 mg/ml, Boehringer Ingelheim). Antibiotic coverage was maintained for five post-operative days with daily injections of enrofloxacine (7.5 mg/kg s.c.).

4.2.6 *Two-photon calcium imaging*

Anesthesia was induced inside a chamber filled with 5% isoflurane. After the righting reflex was lost, the animals were intubated with a custom-made endo-tracheal tube and mechanically ventilated at a rate of 45–55 bpm (SAR-100 Small Animal Ventilator, CWE Inc, USA). Isoflurane was supplied through the respirator at a dose of 2–3%, using a 1:1 mixture of air and oxygen as the carrier gas. The rats were transferred to the microscope and positioned in a stereotaxic frame (Narishige, Japan), using an incisor attachment and a nose clamp (Figure 4.1f). We initially planned to further fix the head by attaching crocodile clamps on either side of the head-holder wire (see Figure 4.1d,f). In practice, we discovered that this applied overwhelming force to the implant and caused its detachment from the skull in several cases (see Section 4.3). Therefore, we came up with alternative solutions for head fixation without applying force to the implant or causing pain. For Rat 3 we used custom-made blunt ear bars dabbed with a lidocaine-containing ointment (EMLA 5%, AstraZeneca). For Rats 6 & 7, we constructed a fully innocuous head fixation system, including a head support from below and two clamps on the sides (see Figure 4.1f). All contact points were padded with memory foam. The success of this system in Rat 6 allowed us to completely forgo the head-holder wire in Rat 7. Throughout the imaging session (lasting up to five hours), anesthesia was monitored via capnography (NONIN Respsense II, SANIMED GmbH, Germany) and pulse oximetry (PhysioSuite, Kent Scientific Corporation, USA). Rectal temperature was maintained constant at 37°C using a feedback-controlled heating pad (PhysioSuite, Kent Scientific Corporation, USA). Isoflurane dose was adjusted between 1.5–2.5% during imaging. At the end of each imaging session isoflurane was stopped and the animal was extubated as soon as spontaneous breathing was established.

Two-photon imaging was performed using a customized FEMTOSmart Dual microscope (Femtonics, Hungary) equipped with the following modules: a motorized tilting objective unit, a piezo objective positioner, galvanometric and resonant scanners, GaAsP photomultipliers, a 16X objective lens (Nikon LWD, water immersion, NA 0.8), and a CMOS camera. The imaging system was controlled via MESC v4.0 software. For each cranial window we located the pial surface by visualizing blood vessels with green illumination and tilted the objective lens to be perpendicular to the surface. Two-photon excitation was performed with a tunable pulsed femtosecond laser (InSight X3, Spectra-Physics), using 940 nm for GCaMP and 1040 nm for jRGECO1a. We searched for fluorescent neuronal expression at multiple locations within each cranial window, reaching depths of 500 µm below the pial surface. At locations where sufficient expression was found, neural population activity was recorded by imaging a single-plane timeseries (frame rate 30.9 fps, 512 x 512 pixels, field-of-view 650 x 650 μm^2). Multiple such recordings were acquired per imaging session, each one lasting between 250 and 660 s. The imaging depth ranged 50–250 µm (mean ± SD: 142 ± 43 µm), corresponding to cortical layer 2/3. The time between recordings was used to change the imaging location within the cranial window, switch to

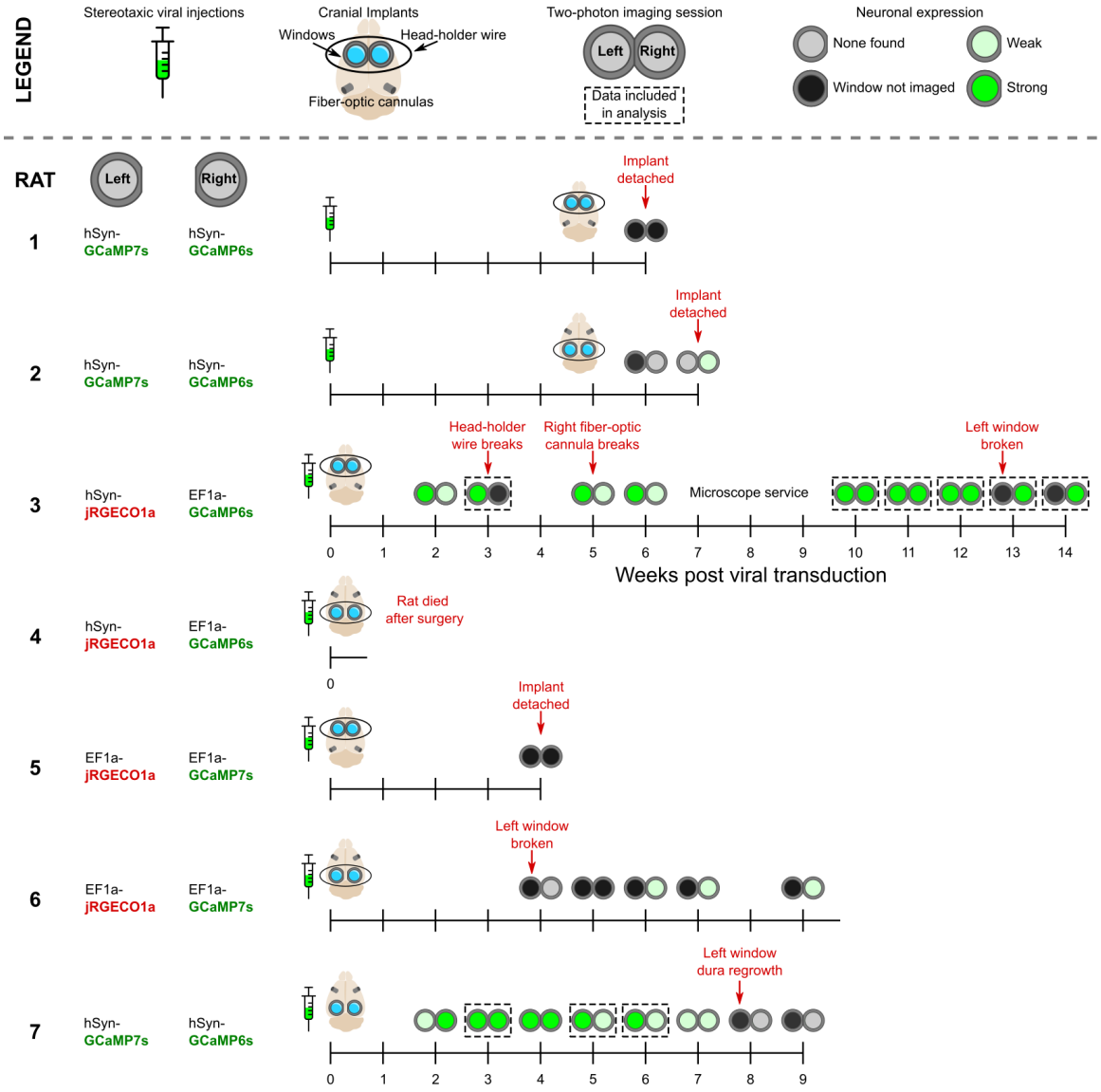

Figure 4.2: Experimental timelines per animal. The following information is depicted for each rat in the study: the timing of surgeries and two-photon imaging sessions, the configuration of cranial implants, the injected fluorescent calcium indicators, and a qualitative estimate for the strength of calcium indicator expression in each imaging session. Unexpected adverse events, such as animal deaths or implant failures, are indicated on the timelines. The imaging sessions that yielded neural activity recordings included in analysis are framed by dashed boxes.

the other cranial window, or adjust the isoflurane dose (always followed by a minimum equilibration period of 10 minutes).

4.2.7 *Histology*

The rats were sacrificed by injecting an overdose of ketamine (Ketamin 10%, Medistar) and medetomidine (Dorbene vet 1 mg/ml, Zoetis) i.p. and perfused transcardially with cold PBS, followed by 4% paraformaldehyde (PFA) in 0.1 M phosphate buffer. The heads were cut and postfixed in 4% PFA for 2 days. Subsequently, they were stored in PBS and sent to the Institute of Neuropathology (University Medical Center Göttingen) for processing and staining. This process is still ongoing (results pending).

4.2.8 *Sensory and optogenetic stimulation*

We obtained two types of recordings—with or without external stimulation, hereafter referred to as 'stimulation' and 'rest', respectively. Stimuli were delivered at intervals of 15 s, alternating between modalities. Some recordings were obtained with sensory stimulation only (visual and somatosensory), while others also included optogenetic stimulation. Each stimulus presentation was brief, lasting either 50 or 100 ms. The parameters used for each stimulus modality are given below:

1. ELECTRICAL FOREPAW STIMULATION (EFS). The stimuli were delivered to the right forepaw via a pair of needle electrodes inserted between digits 2–3 and 3–4. Each stimulation epoch was composed of 10 Hz unipolar pulses with a pulse width of 0.3 ms and an amplitude of either 1.5 or 3 mA (Stimulus Generator 4002, Multi Channel Systems MCS GmbH, Reutlingen, Germany).
2. VISUAL STIMULATION. A single flash of white light delivered by a high-power 3W LED positioned approximately 20 cm in front of the animal. The measured power at the location of the eyes was $\approx 0.35\ \mu W/mm^2$. Note that the eyes were covered by an opaque white ointment (Bepanthen, Bayer).
3. OPTOGENETIC STIMULATION. A single flash of excitation light was generated by LED sources (Doric Lenses Inc., Franquet, Quebec, Canada) at 465 (blue) or 595 nm (amber) and delivered to the implanted cannulas via a fiber-optic patch cord (core diameter 400 µm, NA 0.57). Stimulus intensity and timing were controlled via Doric Neuroscience Studio v5.4.1. Blue light intensity was varied between 200 and 800 mA, corresponding to an output power range of 14.4–42.8 mW/mm^2 (measured at the animal end of the patch cord). The amber light intensity was set to 1000 mA, corresponding to output power of 12.8–15.1 mW/mm^2.

4.2.9 *Two-photon image processing*

After excluding recordings with insufficient signal-to-noise ratio or excessive motion, we were left with 79 recordings acquired across nine sessions from two rats (Rats 3 & 7, see Figure 4.2). The total duration of the retained data added up to 8.27 hours (see Table 4.2

RAT ID	AREA	SIDE	VIRAL CONSTRUCT	STIMULATION	RECORDINGS	DURATION (MIN)
3	S1FL	L	AAV9-hSyn-jRGECO1a	No	13	73.08
				Yes	12	71.75
	V1	R	AAV9-EF1a-GCaMP6s	No	15	98.75
				Yes	23	154.08
7	S1FL	L	AAV9-hSyn-GCaMP7s	No	5	30.83
				Yes	6	37.00
	V1	R	AAV9-hSyn-GCaMP6s	No	3	18.50
				Yes	2	12.33
TOTAL					79	496.33

Table 4.2: Analyzed two-photon calcium imaging recordings.

for the distribution of time across animals and cortical areas). The image timeseries were preprocessed by first identifying frames containing photostimulation artifacts (from visual or optogenetic flashes) and replacing them with the preceding un-corrupted frame. We then down-sampled the data to a temporal resolution of 6.18 fps by averaging every five frames. The down-sampled recordings were further analyzed using suite2p v0.10.143 (Pachitariu et al., 2017). The specific steps of the suite2p pipeline, including some custom modifications, will be described in the following paragraph.

Motion correction was performed via rigid registration of all frames to a reference image, using phase correlation as a similarity metric. This was followed by automatic activity-based region-of-interest (ROI) detection. Suite2p uses a built-in classifier to assign a cell probability for each ROI, i.e. the probability of it being a neuronal soma. The classifier makes use of both anatomical (size, aspect ratio, compactness) and functional ROI metrics (skewness, correlation with neighboring pixels). It has been trained by manual labeling of somata in the visual cortex of GCaMP6-expressing mice. Since our data differed from the training dataset in a number of ways, we did not rely on the built-in classifier and instead implemented a customized classification procedure. As a first step, we excluded parts of the field-of-view with very low mean fluorescence, to account for the fact that neuronal expression in our data was not ubiquitous (unlike in genetically engineered mouse lines). We then used some of the anatomical and functional ROI metrics computed by suite2p and applied the following criteria: radius < 16 µm (derived from a 2D gaussian fit of the ROI mask), compactness < 1.25 (1 is a disc, larger values are less compact), and skewness of the activity trace > 0.2. We considered a ROI to be a 'cell' if its center was within the non-excluded part of the image and if it satisfied all three criteria. We verified through visual inspection that our procedure led to more plausible cell candidates than the built-in suite2p classifier (see example in supplementary Figure A.10). We extracted each cell's fluorescent trace by averaging pixels inside it. We then estimated the signal baseline using the suite2p approach: smoothing (gaussian kernel with standard deviation of 1 s) followed by calculating the rolling maximum of the

rolling minimum (window size 40 s). Each fluorescent trace was normalized as percent signal change relative to the baseline (ΔF/F).

$$\Delta F/F = 100 \cdot \frac{fluorescence - baseline}{baseline}$$

4.2.10 *Detection of bursts*

We implemented a custom python algorithm for automatically detecting burst and suppression epochs in calcium imaging recordings. We started by taking the mean ΔF/F fluorescent trace across cells and applied min-max scaling (minimum set to 0, maximum to 1). We identified peaks in the scaled signal by using the *scipy.signal.find_peaks* function (minimal distance between peaks 1s; peak prominence threshold 0.15, based on a window length of 3 s). For each peak we extracted its onset (when the signal rose above 30% of the peak height) and offset (when the signal fell below 20% of the peak height). The epochs between peak onsets and offsets were defined as bursts and the ones between bursts as suppressions. If a suppression lasted for less than 1 s, we made it part of the two surrounding bursts. This threshold—the so-called 'silent' second—is often used to define suppressions and has been proposed as an endpoint for assessing anesthetic potency in animals (Korkmaz and Wahlström, 1997; Pilge et al., 2014). The above approach entails that several peaks occurring in rapid succession will be assigned to a single burst epoch. By inspecting the assigned epochs across all recordings (see examples in Figure 4.4), we identified 9/79 recordings for which the peak detection had failed and excluded those from downstream analysis. For the remaining 70 recordings we computed the burst-suppression ratio (BSR)—defined as the time spent in suppression divided by the total recording time. We also extracted the amplitude of the first peak per burst epoch (hereafter referred to as the 'burst amplitude'). To determine which bursts were likely to be stimulus-evoked, we counted the number of burst onsets within 1 second from the start of each stimulus. The number of these stimulus-evoked bursts as a ratio of total stimulus presentations will be referred to as burst-triggering probability.

4.3 RESULTS

4.3.1 *Animal survival and implant longevity*

The timelines for every animal are shown in Figure 4.2, including animal deaths and implant failures. Six out of seven rats survived the surgeries, with one (Rat 4) succumbing to respiratory depression during the post-operative period. Rats 1 & 2 showed motor deficits (paretic limbs) for ≈ 12 hours following the virus injection surgery. We hypothesized that these could have resulted from swelling due to rapid virus injection. Slower injection rates were used for the following rats and no further motor impairments were observed. All subsequent animals showed rapid post-operative recovery, with normal spontaneous behavior the day after the surgery. Wound healing was satisfactory in 6/7 animals. One animal (Rat 6) developed a hypertrophic skin reaction at the posterior wound margin, which grew slowly over several weeks.

In Rats 1 & 2 we encountered structural problems with the implants. Specifically, the entire cranial implant detached from the skull surface during the first (Rat 1) or the second (Rat 2) two-photon imaging session. The incidents occurred when we applied external force to the implants—clamping the steel wire for head fixation or plugging an optical fiber. The weak point was the attachment of the dental cement to the skull surface. This led us to re-evaluate our surgical procedure. For subsequent animals we used a different cement (see Section 4.2.5) that had worked well for nonhuman primate surgeries. We hoped that the more liquid consistency of the new cement would allow for deeper penetration into skull pores, leading to firmer attachment. This indeed improved the stability of the implants but was only part of the solution. We encountered the same problem in yet another animal (Rat 5), again while trying to fix the head via the steel wire. In Rat 3 the implant remained attached to the skull, but the steel wire itself broke. We decided that this head fixation method could not be relied upon and turned to the alternative solutions described above (see Figure 4.1f and Section 4.2.6).

For two-photon imaging, it is important that cranial windows remain intact and clear for multiple weeks. In two cases the window glass cracked, either 13 weeks (Rat 3, left window) or 4 weeks (Rat 6, left window) after surgery. In both cases the window was sealed with glue, and imaging was continued through the other window. In another case (Rat 7, left window) we observed the gradual regrowth of dura from the craniotomy edges, leading to a complete obstruction of imaging from the 8th week onwards. The right windows in Rats 3, 6, and 7 remained clear for at least 14, 9, and 9 weeks after surgery, respectively. The fiber-optic cannulas remained intact and functional in most cases, with one exception in Rat 3 (right cannula broken during the 5th week).

RAT ID	AREA	SIDE	VIRAL CONSTRUCT	N	DETECTED CELLS	MAXΔF/F (%)
3	S1FL	L	AAV9-hSyn-jRGECO1a	23	300.3 ± 49.3	10.6 ± 5.3
		R	AAV9-EF1a-GCaMP6s	34	169.6 ± 68.1	5.1 ± 1.8
7	V1	L	AAV9-hSyn-GCaMP7s	7	211.6 ± 21.8	5.1 ± 1.1
		R	AAV9-hSyn-GCaMP6s	4	249.0 ± 39.1	3.4 ± 1.2

Table 4.3: Number of detected cells and maximum fluorescence change (maxΔF/F) per imaged window. Values represent mean $\pm$ SD across recordings. N: Number of recordings included in the analysis.

4.3.2 *Neuronal expression of calcium indicators*

During two-photon imaging we assessed the strength and extent of viral expression in both cranial windows. We imaged at multiple locations per window, reaching depths of 500 µm. GECI-expressing neurons were identified functionally, through their characteristic activity traces: flat baselines interrupted by sharp peaks in fluorescence. Isoflurane dose was varied between 1.5–2.5% to cover a range of anesthetic depths. This way we ensured that the absence of neuronal activity would not be due to constant suppression from an excessive anesthetic dose. Figure 4.2 depicts our qualitative assessment of neuronal expression across imaging sessions. We considered expression to be strong if there

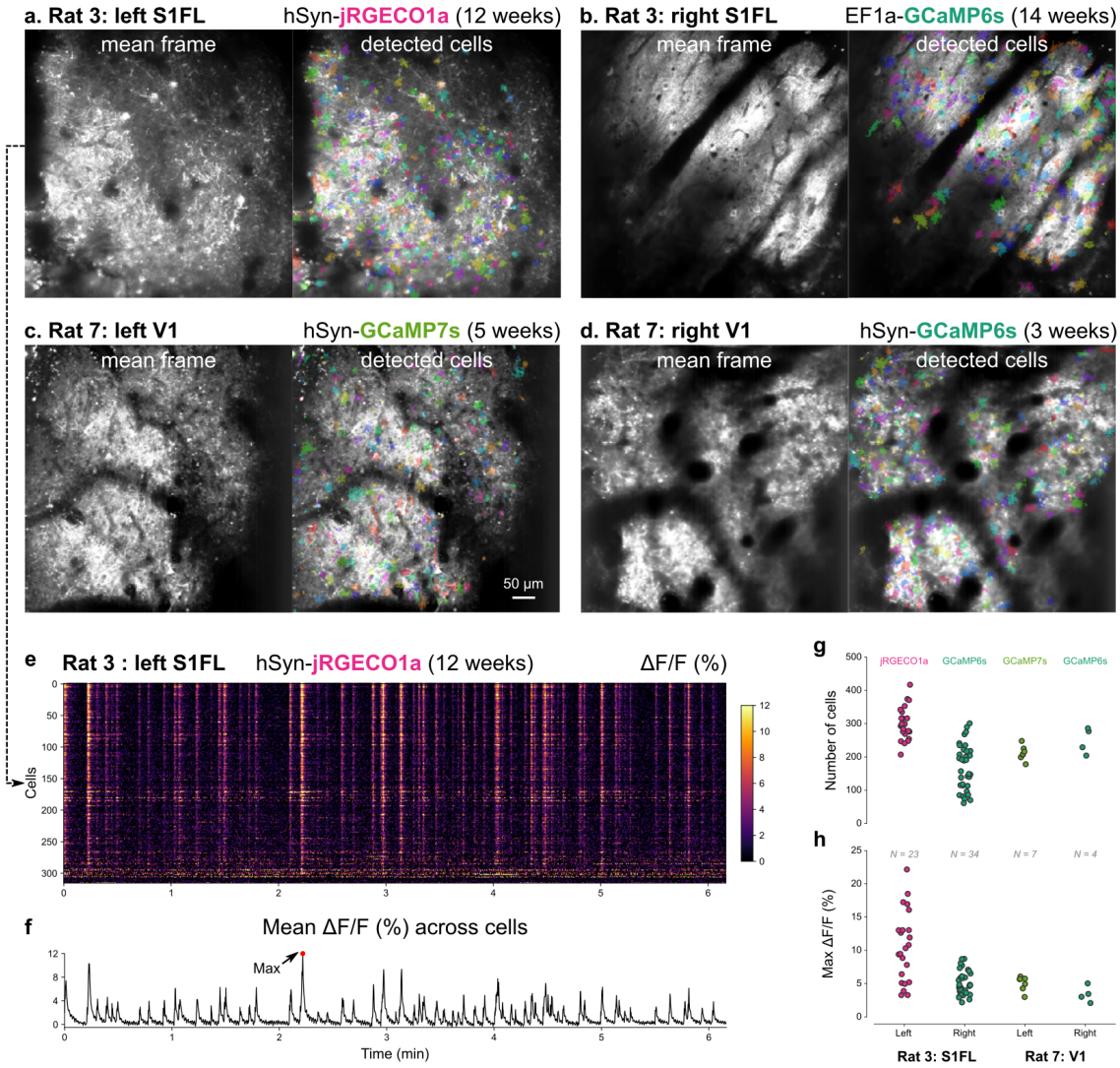

Figure 4.3: Neuronal expression of calcium indicators. Panels **a–d** show example recordings from the left and right cranial windows of two rats. For every recording the mean frame is shown alongside the masks of the detected cells. The expressed viral constructs and the weeks since viral injection are also indicated. The fluorescent traces ($\Delta F/F$) of the cells in example **a** are represented as a heatmap in **e**, exhibiting marked synchrony. The mean $\Delta F/F$ across cells is shown in **f**, with its maximum value indicated (max$\Delta F/F$). Panels **g** and **h** show the number of detected cells and the max$\Delta F/F$ across recordings.

DOSE (%)	N_R	BSR	N_E	BURST DUR. (S)	SUPPR. DUR. (S)	BURST AMPLITUDE (%)
1.50	12	0.28 ± 0.14	414	6.26 ± 7.80	2.59 ± 1.42	3.55 ± 3.59
1.75	4	0.40 ± 0.06	250	4.37 ± 3.76	2.89 ± 1.60	3.76 ± 1.62
2.00	31	0.64 ± 0.16	1355	2.51 ± 1.60	5.38 ± 5.09	3.40 ± 2.32
2.25	8	0.82 ± 0.08	247	1.94 ± 0.87	10.10 ± 15.28	2.39 ± 1.31
2.50	13	0.83 ± 0.05	357	1.95 ± 0.80	9.53 ± 10.11	3.33 ± 2.88

Table 4.4: Burst-suppression across isoflurane doses. Burst-suppression ratio (BSR) values represent mean ± SD across recordings (N_R). Burst duration, suppression duration, and burst amplitude values represent mean ± SD across epochs (N_E). N_E = number of bursts = number of suppressions.

was at least one patch of active neurons with minimum area equal to 300 μm^2 (approximately half the field-of-view). Examples of patches with strong expression can be found in Figure 4.3a–d. If the fluorescent patch was smaller, or it contained no clear neuronal activity, the expression was considered to be low. To get a more quantitative measure of neuronal expression, we evaluated two metrics per recording: the number of detected cells and the maximum peak in mean cellular fluorescence—max$\Delta F/F$ (see Figure 4.3e–f). Expression was strongest in Rat 3, lasting for at least three months in both windows (Figure 4.2). The left window (expressing hSyn-jRGECO1a in S1FL) contained the most cells, with the highest changes in fluorescence: 300.9 ± 49.3 cells, max$\Delta F/F = 10.6 \pm 5.3\%$ (across recordings). For detailed results see Table 4.3 and Figure 4.3g–h.

4.3.3 *Burst-suppression across isoflurane doses*

Based on the literature and on our own fMRI data from isoflurane-anesthetized rats (Chapter 3), we expected to encounter burst-suppression at a dose of 2%. The calcium imaging recordings acquired at 2% indeed exhibited the telltale signs of burst-suppression. Single-cell fluorescent traces were almost entirely synchronous: peaks in fluorescence (bursts) and periods of silence (suppressions) occurred simultaneously across cells (see example in Figure 4.3e). Suppressions occupied $\approx 2/3$ of the recording time ($BSR = 0.64 \pm 0.16$). If the observed synchronous activity truly represents burst-suppression, it should exhibit predictable dose-dependent behavior. Increasing the isoflurane dose should reduce the duration of bursts and prolong the duration of suppressions, while decreasing the dose should have the opposite effect. Our preliminary data, covering a dose range of 1.5–2.5% fully conformed to this expectation (see Figure 4.4). BSR increased monotonically from 0.28 ± 0.14 at a dose of 1.5% to 0.83 ± 0.05 at 2.5%. This was accompanied by a decrease in the duration of bursts (from 6.26 ± 7.80 s at 1.5% to 1.95 ± 0.80 s at 2.5%) at the expense of suppressions (from 2.59 ± 1.42 s at 1.5% to 9.52 ± 10.11 s at 2.5%). The burst amplitude did not appear to vary across doses. Detailed results are given on Table 4.4.

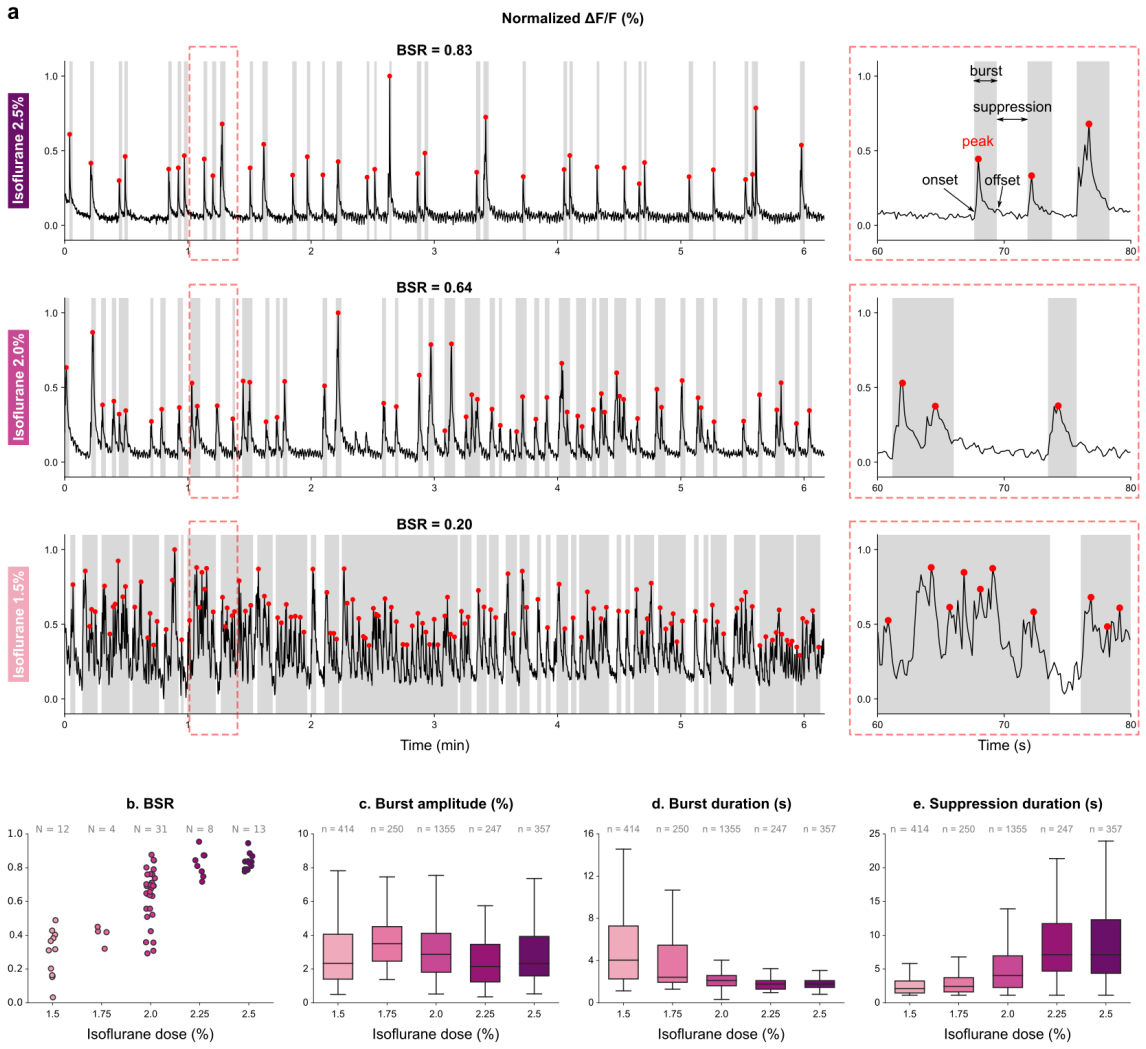

Figure 4.4: Burst-suppression across isoflurane doses. **a.** Representative fluorescence traces acquired at three doses of isoflurane (2.5, 2.0, and 1.5%). Each trace represents the mean ΔF/F signal across cells, after min-max normalization. All three recordings were acquired in the left S1FL window of Rat 3, during the same imaging session (12 weeks post viral induction with hSyn-jRGECO1a). Insets to the right offer an expanded view on 20 seconds of each recording. Identified peaks are marked in red. Detected burst epochs are shaded in gray. **b.** Burst-suppression ratio (BSR)—time spent in suppression divided by total time—is plotted across isoflurane doses (N: number of recordings). Burst amplitude (**c**), burst duration (**d**), and suppression duration (**e**) are shown as boxplots across isoflurane doses (n: number of bursts/suppressions).

4.3.4 *Stimulus-evoked bursts*

During early exploratory tests we observed that stimuli with longer duration (100 ms compared to 50 ms) and higher amplitude (EFS 3mA compared to 1.5 mA) evoked neuronal responses more readily. The results reported here concern the longer (100 ms) and stronger (3mA) stimulus variants. Within the scope of this pilot study, we focused on two immediate goals: visualizing neural activity traces during the peri-stimulus period and detecting stimulus-evoked bursts. We took the min-max scaled mean $\Delta F/F$ traces and extracted peri-stimulus epochs—from -1 to $+3$ seconds relative to stimulus onset. We divided the extracted epochs across the four imaged brain areas (bilateral S1FL and V1) and across isoflurane doses (whenever stimulation recordings were acquired at more than one dose). The peri-stimulus activity traces can be viewed in Figure 4.5 for sensory and in Figure 4.6 for optogenetic stimuli. We also estimated the burst-triggering probability by counting burst onsets occurring within 1 second of the stimulus start and dividing them by the number of evaluated stimulus epochs.

At high isoflurane doses (2.25–2.5%), most EFS and visual stimuli were followed by bursts within the 1-second window (Figure 4.5). These evoked bursts occurred across cortical areas, not being confined to the stimulus-appropriate regions (left S1FL for right forepaw stimulation, bilateral V1 for visual stimulation). Visually-evoked bursts peaked at ≈490 ms after the stimulus onset in all cortical areas. EFS-evoked bursts peaked earlier in the stimulus-appropriate area (≈320 ms in the left S1FL) and later in the other three (≈490 ms). At the isoflurane dose of 2% approximately half of the stimuli led to evoked-bursts, which also occurred across all areas. Only few bursts were triggered at the lowest isoflurane dose (1.5%), with most traces showing no sign of change (Figure 4.5a–b).

The picture was less clear for optogenetic stimuli (Figure 4.6). Unfortunately, Rats 3 and 7—the source of almost all our usable calcium imaging data (see Table 4.2 and Figure 4.2)—each had only one functional fiber-optic cannula. Hence, optogenetic stimulation was performed in either the left V1 of Rat 3, which had received a control injection of saline, or the left S1FL of Rat 7—injected with the red-shifted opsin ChrimsonR. Ideally, we would only expect responses upon amber-light (595 nm) stimulation of the area transfected with ChrimsonR. Instead, we observed more reliable triggering of bursts upon blue-light illumination (Rat 7, left S1FL, isoflurane 2.25%, see Figure 4.6c–d). The evoked responses peaked at ≈490 ms, similarly to most sensory-evoked bursts. We also observed triggered bursts upon stimulating the saline-injected left V1 of Rat 3, with both amber and blue light (see Figure 4.6b). These responses peaked later ($\geqslant$810 ms). We will offer a plausible explanation for these puzzling results in the discussion.

4.4 DISCUSSION

In this study we performed pilot experiments to develop and test methods for *in vivo* longitudinal two-photon calcium imaging in isoflurane-anesthetized rats. We employed an array of viral constructs to express GECIs and opsins in the rat neocortex. We additionally developed and refined surgical approaches for chronically implanting cranial windows and fiber-optic cannulas in the rat skull. We were able to obtain neuronal calcium activity traces during isoflurane-induced burst-suppression, capturing both spontaneous and

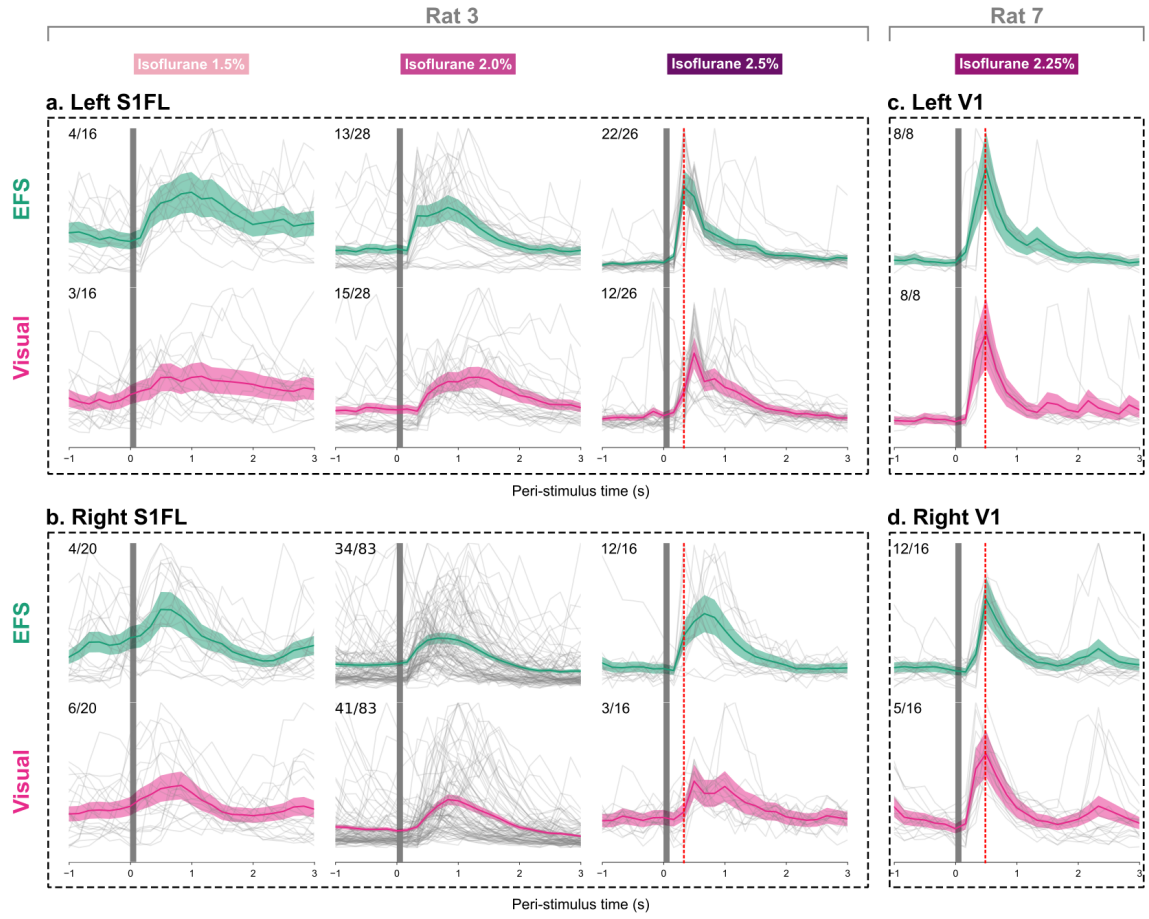

Figure 4.5: Responses to sensory stimulation. Responses to somatosensory (EFS) and visual stimulation are shown in four cortical areas: bilateral S1FL (Rat 3, **a** & **b**) and bilateral V1 (Rat 7, **c** & **d**). The traces are extracted from the mean $\Delta F/F$ signal across cells, after min-max normalization. Each plot shows individual stimulus epochs (gray lines), along with the mean (thick line) and SEM (colored bands) across epochs. The ratio at the top left of each plot is the burst-triggering probability: i.e. number of burst onsets occurring within 1 second of stimulus start as a ratio of analyzed stimulus epochs. All stimuli have a duration of 100 ms (vertical gray bands). The vertical red dashed lines are aligned with the peaks of the EFS-evoked responses in the left S1FL ($\approx$320 ms) and V1 ($\approx$490 ms). EFS: electrical forepaw stimulation (of the right forepaw). S1FL: forelimb region of the primary somatosensory cortex; V1: primary visual cortex.

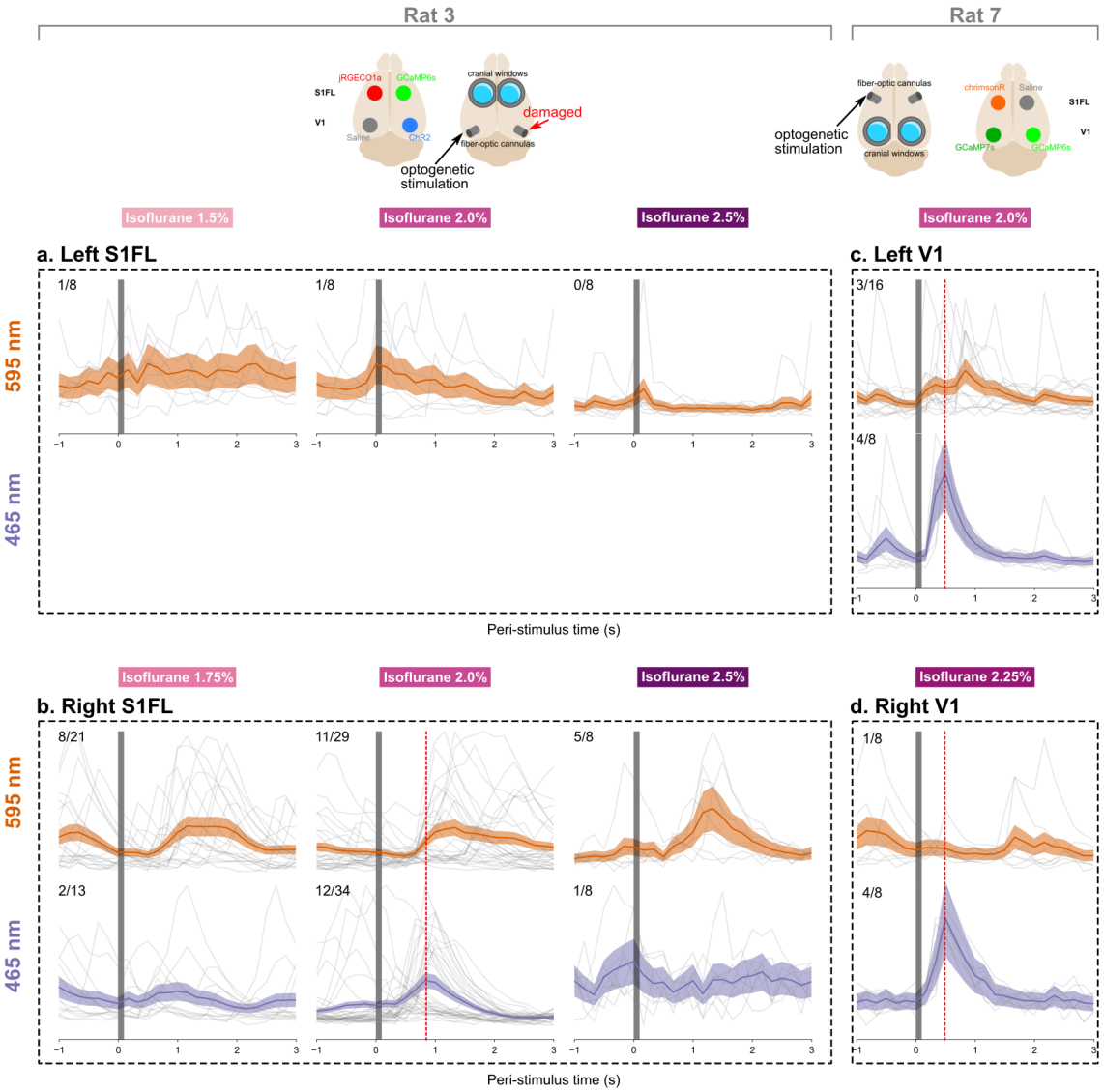

Figure 4.6: Responses to optogenetic stimulation. Responses to blue (465 nm) or amber (595 nm) light are recorded in four cortical areas: bilateral S1FL (Rat 3, **a** & **b**) and bilateral V1 (Rat 7, **c** & **d**). The schematic at the top shows the injected viral constructs and the location of cannulas used for light delivery. The traces are extracted from the mean $\Delta F/F$ signal across cells, after min-max normalization. Each plot shows individual stimulus epochs (gray lines), along with the mean (thick line) and SEM (colored bands) across epochs. The ratio at the top left of each plot is the burst-triggering probability: i.e. number of burst onsets occurring within 1 second of stimulus start as a ratio of analyzed stimulus epochs. All stimuli have a duration of 100 ms (vertical gray bands). The vertical red dashed lines are aligned with the peaks of the blue-light-evoked response in the right S1FL (≈810 ms) and V1 (≈490 ms). S1FL: forelimb region of the primary somatosensory cortex; V1: primary visual cortex.

stimulus-evoked bursts. We thereby reproduced the known dose-dependent properties of burst-suppression and evaluated the capacity of various sensory and optogenetic stimuli to evoke bursts. In the following paragraphs we will first discuss the methodological problems we encountered and identify possibilities for improvement. Then, we will examine how our preliminary data relates to the results of Chapter 3 and to other studies of burst-suppression in rodents. Finally, we will conclude with ideas about the translation of the developed methods to marmosets.

4.4.1 *Methodological considerations*

CALCIUM INDICATORS The project hinged on the successful expression of GECIs in cortical neurons through viral transduction. We took two approaches for assessing expression—two-photon imaging and histology. The first was fully realized only in Rats 3 and 7, in which we directly observed fluorescent layer 2/3 neurons and recorded their activity over multiple weeks (see Figure 4.2 and Table 4.2). The hSyn-jRGECO1a construct performed the best: it led to extensive expression from the 2nd up to at least the 12th week, with the largest number of detected neurons ($\approx$ 300 per imaged plane) and the highest peaks in fluorescence (see Figure 4.3 and Table 4.3). Unfortunately, most injected GECI constructs could not be evaluated via two-photon microscopy, forcing us to solely rely on the pending histological data. Histological localization of transfected cells only represents a snapshot at the time of death. It neither provides an expression timeline, nor can it offer information on the functional signal-to-noise ratio. Considering the above, we are inclined to keep using the hSyn-jRGECO1a construct for future experiments. Apart from performing very well in practice, this construct also possesses several theoretical advantages. It is driven by the hSyn promoter, which is reportedly the more neuron-specific one of the two we tested (Kügler et al., 2003). Moreover, jRGECO1a is characterized by fast response kinetics and comparable sensitivity to GCaMP6 (Dana et al., 2016). Lastly, the red-shifted excitation and emission spectra of jRGECO1a should allow for deeper tissue penetration (due to reduced light scattering and tissue absorption) and minimize phototoxicity (Dana et al., 2016).

OPSINS A secondary aim was to co-express an excitatory opsin in a different cortical area. Since we had no optical access to the sites injected with opsin constructs, we could not assess their fluorescence directly. We had hoped to get indirect evidence for opsin expression, by evoking bursts via the opsin-specific excitation wavelength. Having failed in this, we must make do with histological information. From an optical point of view, hSyn-ChR2 should be a suitable partner for hSyn-jRGECO1a (Emiliani et al., 2015). If its neuronal expression can be confirmed histologically, this construct will be a prime candidate for use in future experiments. However, we must first address the issue of non-specific evoked responses during our attempts at optogenetic stimulation (Figure 4.6). A likely explanation for our results is that excitation light intended for opsins acted as a visual stimulus. This can conceivably occur in two ways: light can escape from the connection point with the cannula and reach the eyes externally, or it can travel though brain tissue and reach the retina internally. This explains why our best 'optogenetic' responses were observed with blue light in Rat 7: rat retinas are much more sensitive to blue than to

amber light (Rocha et al., 2016) and the cannula in Rat 7 was implanted in S1FL—closer to the eyes. If the external way is the culprit, the issue could be remedied by meticulous optical insulation of all fiber-optic connections. If the problem persists, it may be impossible to perform purely optogenetic stimulation during burst-suppression, given the brain's hypersensitivity to visual flashes during this state (Hartikainen et al., 1995; Hudetz and Imas, 2007; Kroeger and Amzica, 2007; Land et al., 2012).

CRANIAL IMPLANTS The next important milestone was the structural integrity and longevity of cranial implants, which is what we had most problems with. We learned through our mistakes and have already identified problematic components. Implant detachments occurred upon external force application, usually during head fixation. Even though the rats were group-housed in conventional cages, no implants were lost spontaneously or removed by cagemates. This narrows the problem down to head fixation. The solution we employed for Rat 7 consisted of a completely innocuous head support setup that applied no force to the implant (see Figure 4.1f). This setup does not prevent all motion and would not be suited for awake recordings. However, it may be sufficient for our deeply anesthetized animals, where the only source of motion is mechanical ventilation. Periodic noise from respiratory motion was clearly present in the calcium imaging data, albeit with much smaller magnitude than the neural signal. It is best to avoid it altogether, since it induces drift along the z-axis, which cannot be remedied by any existing motion correction algorithm (Stringer and Pachitariu, 2019). We could further minimize head motion by iterative improvements of our fixation setup. If this will not be enough, we would have to completely alter our implant design and firmly anchor a head plate to the skull via bone screws.

DATA ACQUISITION The presented two-photon imaging data consisted of a single-plane time-series covering a 650 μm^2 square (512 x 512 pixels) at 30.9 fps, yielding ≈300 neurons in the best case. Our two-photon system also allows alternative modes of imaging, which can be advantageous for specific experimental questions. The piezo-electric objective positioner permits the rapid acquisition of multiple planes along the z-axis, covering a range of 400 µm. In cases with extensive neuronal expression across cortical depths, this mode could be used for the simultaneous recording of even more neurons, at the cost of temporal resolution. In practice we could cover 3–4 imaging places at a rate of ≈3 fps, comparable to what is often used in mice (Stringer et al., 2019). We could also move towards increasing the temporal resolution up to 100 Hz, by decreasing the field-of-view, or via line-scanning. This would allow us to precisely measure delays in burst onsets across cortical areas and thus infer the likely origin and direction of travelling bursts. Ultimately, the above imaging modes could be alternated within or across imaging sessions. Our longitudinal experimental design in theory permits the imaging of the same group of neurons for multiple weeks. It would be of interest to examine the reproducibility of their activity between sessions. We already attempted to locate the same imaging plane across sessions, using the pial vessels as landmarks. However, this proved hard in practice, due to shifting vessel morphology and variations in the positioning of the animal and the objective. Accurate localization of the same neurons would require a specialized automatic head positioning system (Scott et al., 2013).

DATA ANALYSIS The automatic segmentation of ROIs and the identification of cells is perhaps the most crucial step in calcium imaging data analysis (Pnevmatikakis, 2019; Stringer and Pachitariu, 2019). In Section 4.2.9 we outlined our approach, which was based on the suite2p pipeline (Pachitariu et al., 2017). Due to the partial failure of the built-in suite2p classifier on our data (see Supplementary Figure A.10), and the lack of time for manually reviewing every detected cell, we resorted to applying hard decision criteria for cell classification. A better solution for future analysis would be to manually label the acquired pilot dataset and use it to re-train the suite2p classifier. It would also be prudent to reproduce the findings with other software packages (Giovannucci et al., 2019; Inan et al., 2021). Another important issue is neuropil contamination. Since the point-spread function in two-photon imaging is wider along the z-axis, the signal of any given cell is contaminated by the average activity of diffuse out-of-focus axons and dendrites. Suite2p explicitly models neuropil contributions as part of ROI detection (Pachitariu et al., 2017), but we do not know how well this method fares during burst-suppression. The profound synchrony characterizing this state could complicate the separation of single-cell activity from that of the average population. As a final analysis step, underlying spike trains can be inferred through deconvolution of cellular fluorescent signals (Pachitariu et al., 2018). The estimated spike trains should better reflect the true onset and duration of bursts. Analyzing the population spike data is among our future goals. For example, we could use embedding algorithms to identify ensembles of co-active neurons and track their activity across anesthetic doses (Stringer et al., 2019; Wenzel et al., 2019).

4.4.2 *The anesthetic dose-dependency of burst-suppression*

Our preliminary calcium imaging data (Figure 4.4) demonstrate that the temporal properties of burst-suppression scale with isoflurane dose: increasing the dose leads to longer bursts and shorter suppressions, without changing the amplitude of bursts. These findings are in complete agreement with local field potential recordings in rats anesthetized with isoflurane (Stenroos et al., 2021). They also shed light on why most fMRI-detected instances of burst-suppression in rats were found at an isoflurane dose of 2% (see Figure 3.5). As detailed in Table 4.4, a 2% dose corresponds to suppressions occupying $\approx 2/3$ of the time. Individual bursts are separated by intervals of 5.38 s on average and can thus be captured by the temporal resolution of fMRI (2 s). The shorter suppression duration at 1.5% (2.59 s) is below the Nyquist limit for fMRI—meaning individual bursts can no longer be separated. At 2.5% bursts are sparsely spaced and very short in duration, perhaps corresponding to only a few spikes per cell. fMRI may lack the sensitivity to detect hemodynamic responses to such small events. In other words, an isoflurane dose of 2% maximizes the effect of burst-suppression on BOLD fMRI, by eliciting bursts that are long enough to produce robust hemodynamic responses, but also adequately spaced to be resolved by fMRI acquisition rates.

4.4.3 *Stimulus-evoked bursts*

We observed burst-suppression in all four imaged cortical areas (bilateral S1FL and V1), which re-affirms the results of Chapter 3 regarding the pancortical distribution of burst-

suppression in rats (see Figure 3.5). We also demonstrated the ability of very brief (100 ms) visual and somatosensory stimuli to trigger the onset of bursts, reproducing the findings of several other studies (Hartikainen et al., 1995; Hudetz and Imas, 2007; Kroeger and Amzica, 2007; Land et al., 2012). These bursts were generalized and not confined to one cortical area. Interestingly, the bursts evoked by stimulation of the right forepaw, peaked first at the left somatosensory cortex (≈320 ms) and then in the other three areas (≈490 ms, a difference of 1 frame in our down-sampled data at 6.18 fps). This is in line with results from isoflurane-anesthetized mice, where calcium travelling waves were reported to originate at the stimulated area, before spreading throughout the cortex (Stroh et al., 2013). The time to cover the entire cortex has been estimated at ≈100 ms in rats (Ming et al., 2021). Perhaps imaging at higher temporal resolutions (or re-analyzing our raw 30.9 fps data) will also reveal a similar delay for visually-evoked bursts. Intriguingly, bursts can be more readily evoked at higher isoflurane doses. This can be attributed to the existence of a post-burst refractory period, which has been reported in mice (Stroh et al., 2013). At lower doses, any external stimulus is likely to coincide with an ongoing spontaneous burst or with its refractory period. At higher doses, where spontaneous bursts are rare, the incoming stimulus is more likely to strike fertile ground and initiate the next burst. We could test this hypothesis by examining the burst triggering probability as a function of the time elapsed since the previous burst.

4.4.4 *From rats to marmosets*

Our preliminary findings recapitulate several known features of burst-suppression in rodents, including the hyper-reactivity to visual stimulation. The rat visual cortex appears capable of generating and propagating bursts like any other cortical area. It is therefore all the more interesting to repeat these experiments in the marmoset visual cortex and find out what is responsible for its apparent uncoupling from burst-suppression. Most materials and methods used in this study should work just as well in marmosets, with slight modifications (e.g. scaling up the cranial windows). We are confident that we can overcome the remaining methodological hurdles through additional experiments in rats. Based on the fMRI map of burst-suppression in marmosets (see Figure 3.4), the most suitable location for a cranial window would be at anterior visual areas—for example around area MT. The window can thus also include neighboring regions engaged in burst-suppression. Recording the spontaneous and stimulus-evoked neuronal activity at both visual and non-visual areas across isoflurane concentrations will likely give us the answers we seek.

5

GENERAL DISCUSSION

We opened this thesis by claiming that a researcher is faced with a 'rock and a hard place' decision when it comes to making an animal 'a part of circuit': restraint or anesthesia. However, this may no longer be true. We are living through the era of 'awake behaving' neuroscience. There is a general tendency to obtain data in naturalistic conditions and under circumstances that are ethologically relevant for the animal. These trends are enabled by marvelous technological developments, like virtually reality and fully implantable wireless brain-computer interfaces. This is a most welcome development both for the animals and the researchers: we are increasingly able to observe brain function in the 'real' world while minimizing animal suffering. What is the place for anesthetized measurements in this brave new world? In light of what we learned through this thesis, we will discuss three possible niches for the continued use of anesthetics in neuroimaging and neurophysiological experiments.

5.1 ANESTHESIA AS A NECESSARY EVIL

Like most researchers, this is how we initially approached the problem. Anesthesia is sometimes just necessary, either to protect the animals from pain or to keep them from moving. This will continue being true despite the aforementioned exciting developments, at least for some time. However, there are several steps we can take, either as individual researchers or as a scientific field, to make the most out of anesthesia when it is unavoidable.

Firstly, we should prioritize transparency and standardization efforts to increase the reproducibility of anesthetized animal experiments. Anesthesia is often treated as more of an art than a science, with individual research groups keeping to their own 'secret sauce'. We must do better. We owe it to our animals, to avoid unnecessary harm, as the 3R principles mandate. We can reduce the number of animals used for research by eliminating unnecessary sources of variance, like the ones introduced by needless variations of anesthetic protocols. We also owe it to other researchers. No future student should be frustrated by the inability to reproduce vaguely phrased protocols. Fortunately, efforts for increasing standardization are already underway. The nonhuman primate neuroimaging community has realized the added value of pooling data and resources, and that this also applies to anesthetic protocols (Milham et al., 2018; Milham et al., 2020). The mouse fMRI field, which has been troubled by technical difficulties and irreproducibility, is also moving towards aggregating datasets across labs and systematically examining the effects of

anesthesia (Grandjean et al., 2020; Reimann and Niendorf, 2020). Similar initiatives are currently underway for rats and they will include the data we acquired for Chapter 2.

Secondly, we should aim to systematically characterize the protocols that are currently in use, like we attempted with our study in Chapter 2. This characterization should include data from as many modalities as possible: pharmacology, cardiovascular and respiratory physiology, neurophysiology, and neuroimaging. Our end goal should be to build a functional 'fingerprint' for each anesthetic protocol, which can serve as a lookup table for estimating the expected effects on variables of interest. With regards to fMRI, this characterization could include BOLD responses to a standardized set of openly shared stimuli, as well as functional 'connectomes' describing the expected correlation structure of task-free acquisitions. Through such efforts, we can make informed decisions about which protocol to use for what purpose, and how to interpret the results. Ideally, such principled fingerprinting should be first completed for healthy wild-type animals before we take a shot at pathologies.

5.2 INVESTIGATING ANESTHETIC MECHANISMS OF ACTION

Anesthesia is a miraculous discovery that has utterly transformed medicine over the last two centuries. Clinicians routinely use anesthetics every day, at every hospital around the world. We take this success for granted and tend to forget that we do not understand how anesthetics work (Brown et al., 2010, 2011; Franks, 2008). This lack of understanding almost certainly prevents us from making full use of their benefits. A key challenge is posed by the remarkable molecular diversity of anesthetic agents. Molecules ranging from noble gases (Xenon) to complex barbiturates lead to a set of rather similar effects (Franks, 2008). Another puzzling aspect is the universality of anesthetics: they act on animals as distant as humans and *C. elegans*. It is hard to imagine how such diversity could be unified in a single theoretical framework. That said, anesthesia research is reawakening, and functional neuroimaging of anesthetized animals—through fMRI or calcium imaging—can certainly be part of the effort. Perhaps the key to understanding anesthesia cannot be found in the molecular actions of individual drugs, but rather on the level of large-scale emergent patterns of brain function. Combining functional neuroimaging with causal perturbations of neural activity may hold the biggest promise for making headway in that direction.

5.3 ANESTHESIA AS A TOOL FOR UNDERSTANDING UNCONSCIOUS STATES

The anesthetized brain is not simply a 'quieter' awake brain; it rather represents a fundamentally different configuration of brain function. In fact, multiple such configurations may exist depending on the agent and the dose. If we imagine all these as occupying a landscape, the awake condition probably fills a small corner of it. Beyond it we will find sleep, and even further a large collection of anesthetized and comatose states. The studies in this thesis support this view. Medetomidine preserves the functional segregation of brain areas, with stimuli reaching their 'appropriate' targets. In our landscape of possibilities, we could probably place medetomidine close to sleep. Isoflurane, on the other hand, produces several radically different states depending on its dose. These span an astonishing spectrum, from mild sleep-like sedation to what is essentially reversible

brain death. Some of these states, like burst-suppression, behave in ways that defy our intuitions. One would expect a deeply anesthetized brain to be unresponsive. Yet, the opposite appears to be true. Even the slightest stimulus can elicit a generalized reaction that spreads through the brain like a seizure. It is not a loss of responsiveness, but rather a loss of response specificity. Burst-suppression probably forms a major attractor on our landscape, a common endpoint for many conditions—as evidenced by its appearance in hypoxia, hypothermia, coma, and metabolic encephalopathies. It is worth finding out what other attractors are out there and how we can travel between them. Anesthetics are the safest and most convenient means of transport to the unexplored reaches of this landscape.

Part II

APPENDIX

A

SUPPLEMENTARY MATERIAL

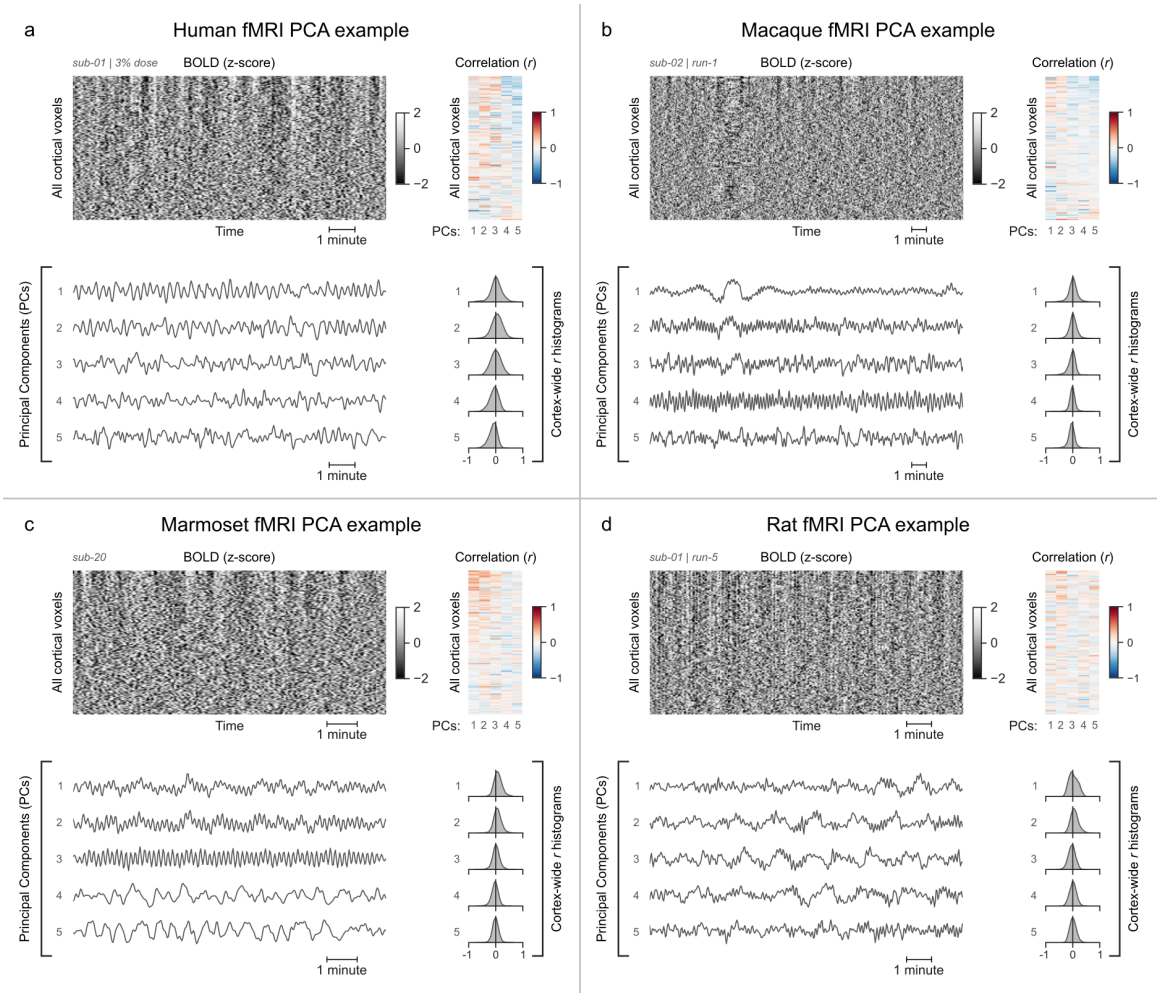

Figure A.1: Examples of fMRI runs without asymmetric PCs. Panel **a.** corresponds to a human subject (same as in Figure 3.1) anesthetized with 3% sevoflurane, while the other panels show an example from each animal species: macaque (**b**), marmoset (**c**), and rat (**d**). For each example, the cortical BOLD fMRI signal is represented as a carpet plot. The rows (voxels) are ordered according to their correlation with the mean cortical signal to better visualize widespread fluctuations. The first five temporal PCs of the signal are plotted below the carpet plot. The Pearson's correlation coefficients (r) between the PCs and all cortical voxels are represented both as a heatmap and as histograms for each PC. All PCs have symmetric histograms, centered around $r = 0$.

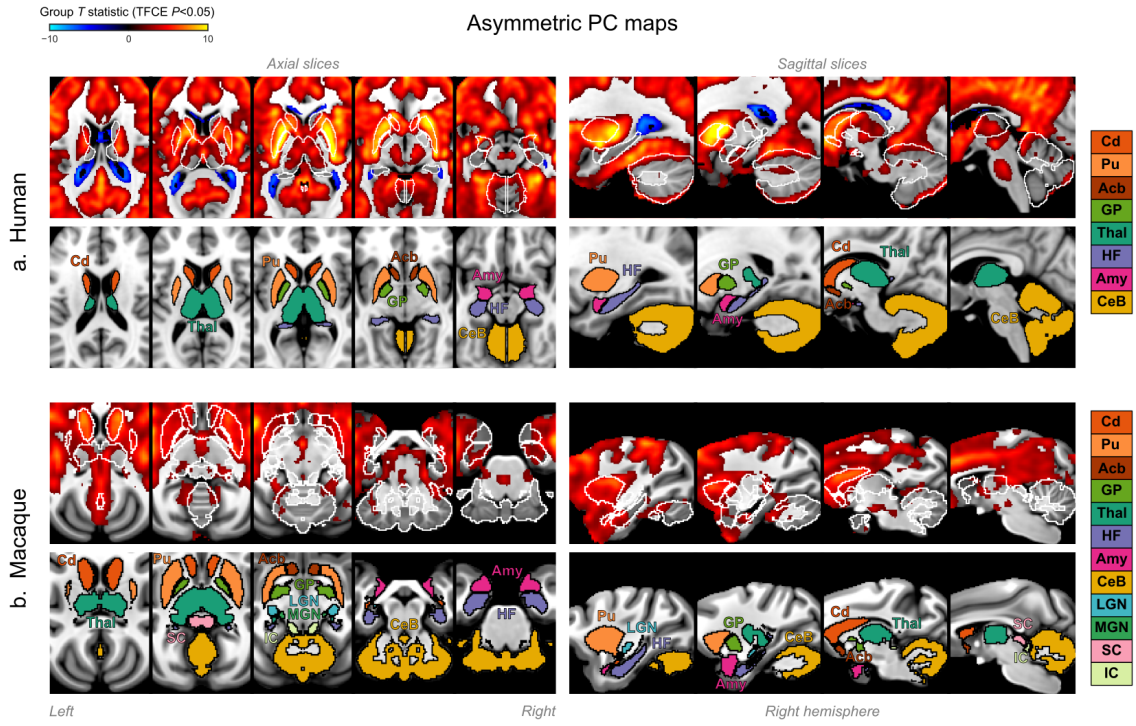

Figure A.2: Correlation of subcortical structures with burst-suppression in humans and macaques. **a.** Group statistic map showing the spatial distribution of asymmetric PCs in humans (same map as in Figure 3.2b). The views are adjusted to focus on subcortical structures, on axial and sagittal slices. The corresponding macaque map (same as in Figure 3.3c) is shown in **b.** For each species, the bottom row shows the location of major subcortical structures, defined based on the human Harvard-Oxford subcortical structural atlas and the Subcortical Atlas of the Rhesus Macaque (SARM). Cd: caudate; Pu: putamen; Acb: accumbens; GP: globus pallidus; Thal: thalamus; HF: hippocampal formation; Amy: amygdala; CeB: cerebellum; LGN: lateral geniculate nucleus; MGN: medial geniculate nucleus; SC: superior colliculus; IC: inferior colliculus.

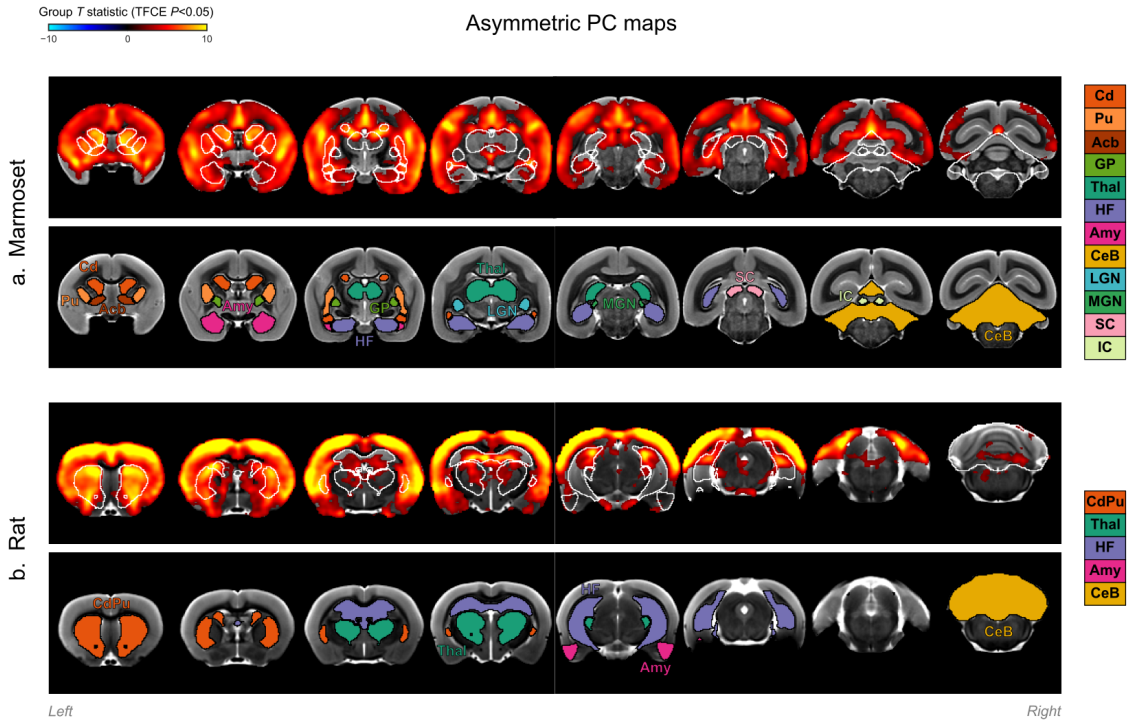

Figure A.3: Correlation of subcortical structures with burst-suppression in marmosets and rats. **a.** Group statistic map showing the spatial distribution of asymmetric PCs in marmosets (same map as in Figure 3.4c). The views are adjusted to focus on subcortical structures, on coronal slices. The corresponding rat map (same as in Figure 3.5c) is shown in **b.** For each species, the bottom row shows the location of major subcortical structures, defined based on the Marmoset Brain Mapping coarse subcortical atlas and the SIGMA rat brain atlas. Cd: caudate; Pu: putamen; Acb: accumbens; GP: globus pallidus; Thal: thalamus; HF: hippocampal formation; Amy: amygdala; CeB: cerebellum; LGN: lateral geniculate nucleus; MGN: medial geniculate nucleus; SC: superior colliculus; IC: inferior colliculus.

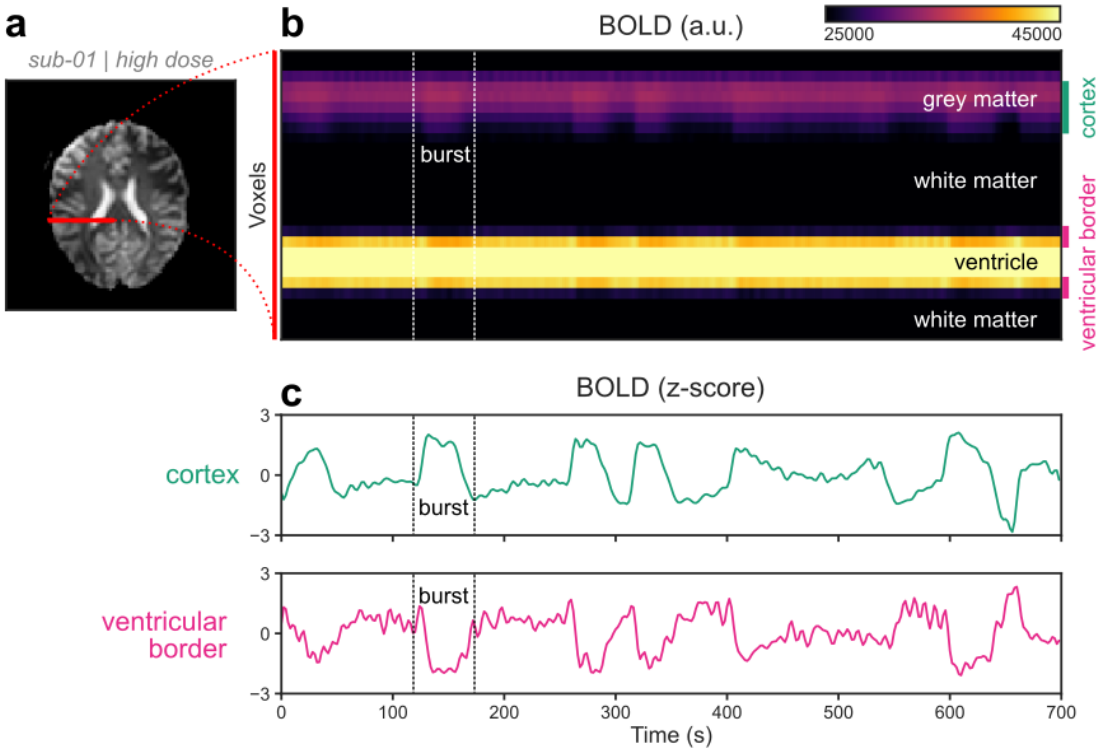

Figure A.4: Ventricular motion during burst-suppression. Panel **a** shows an axial slice from an echo planar imaging (EPI) BOLD fMRI scan of a human subject during burst-suppression (same run as in Figure 3.1). A line profile is marked in red, stretching from the pial surface of the right hemisphere towards the midline, going through cortical grey matter, white matter, and the lateral ventricle. The BOLD signal across this line profile is plotted in **b** for the entire duration of the fMRI run (700 s). One of the bursts is marked by vertical dashed lines. The voxels corresponding to cortex and ventricular borders are marked by green and fuchsia lines, respectively. **c.** During bursts, the mean BOLD signal of the cortical voxels rises—as expected, whereas the signal at the ventricular borders falls. This is most likely caused by an inward motion of the ventricular borders, with the low-intensity BOLD signal of the surrounding white matter replacing the higher-intensity ventricular signal. Even if the motion occurs on a sub-voxel scale, partial volume effects would still cause the darkening of the border.

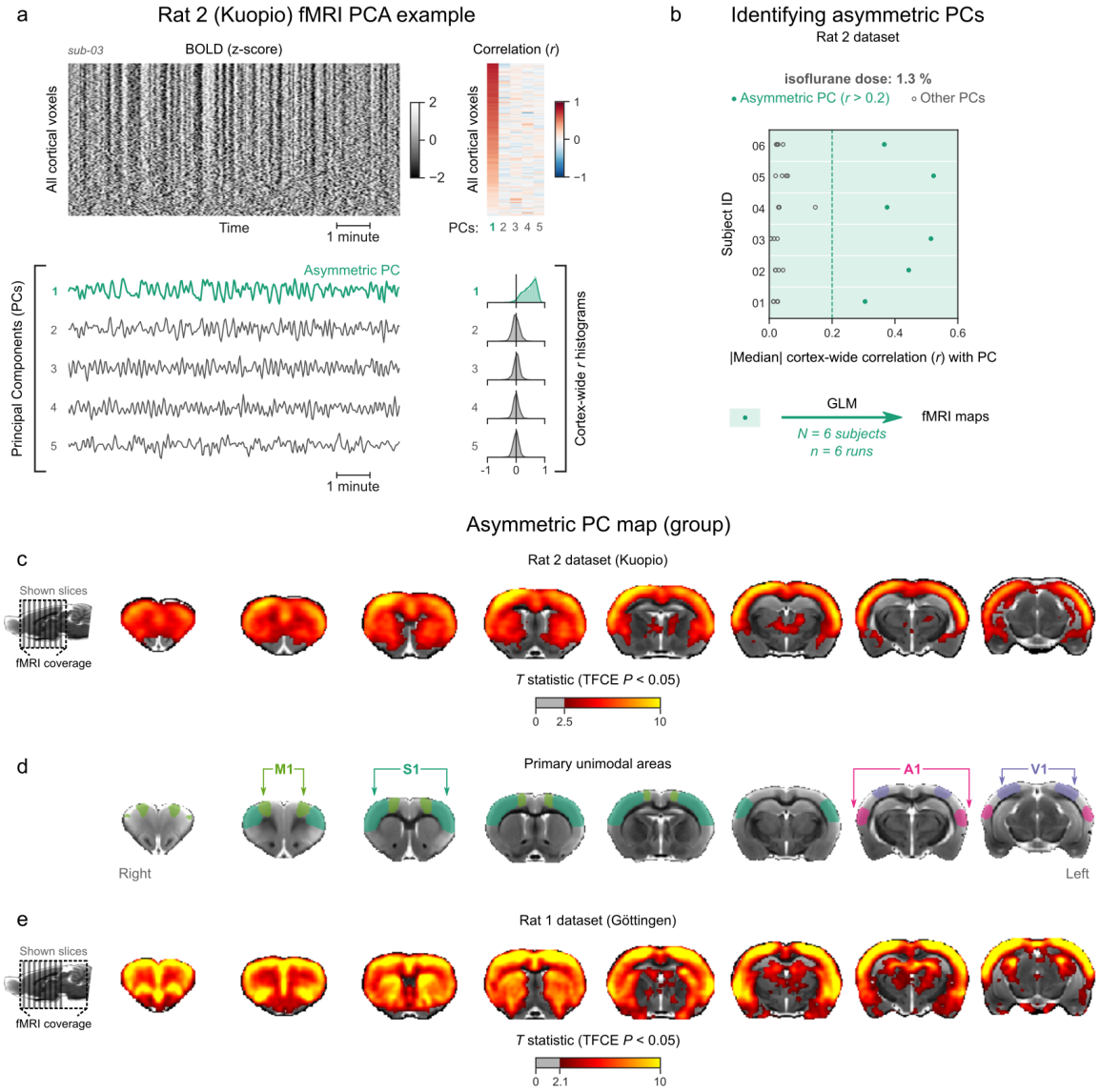

Figure A.5: Identifying and mapping burst-suppression in the Rat 2 dataset. **a.** The cortical BOLD fMRI signal of an isoflurane-anesthetized subject from the Rat 2 dataset is represented as a carpet plot. The first five temporal PCs of the signal are plotted below the carpet plot. The Pearson's correlation coefficients (r) between the PCs and all cortical voxels are represented both as a heatmap and as histograms for each PC. The first PC captures the widespread fluctuation that is visible on the carpet plot and has an asymmetric r histogram. **b.** Cortex-wide median r values for the first five PCs are plotted as dots across the entire Rat 2 dataset (6 animals, one fMRI run each). All fMRI runs have a prominent asymmetric PC ($r > 0.2$, highlighted in green) and are used as regressors for GLM analysis. The group asymmetric PC map—computed via a second-level analysis of single-subject GLMs—is shown in **c**, overlaid on a study-specific volumetric template. The group statistics were carried out with FSL randomise; the resulting T statistic maps were thresholded using Threshold-Free Cluster Enhancement (TFCE) and a corrected $P < 0.05$. The locations of primary motor (M1), somatosensory (S1), auditory (A1), and visual (V1) cortices—based on the SIGMA rat brain atlas—are indicated for reference (**d**). The corresponding map of the Rat 1 dataset (the same as in Figure 3.5c) is shown in **e**, for comparison.

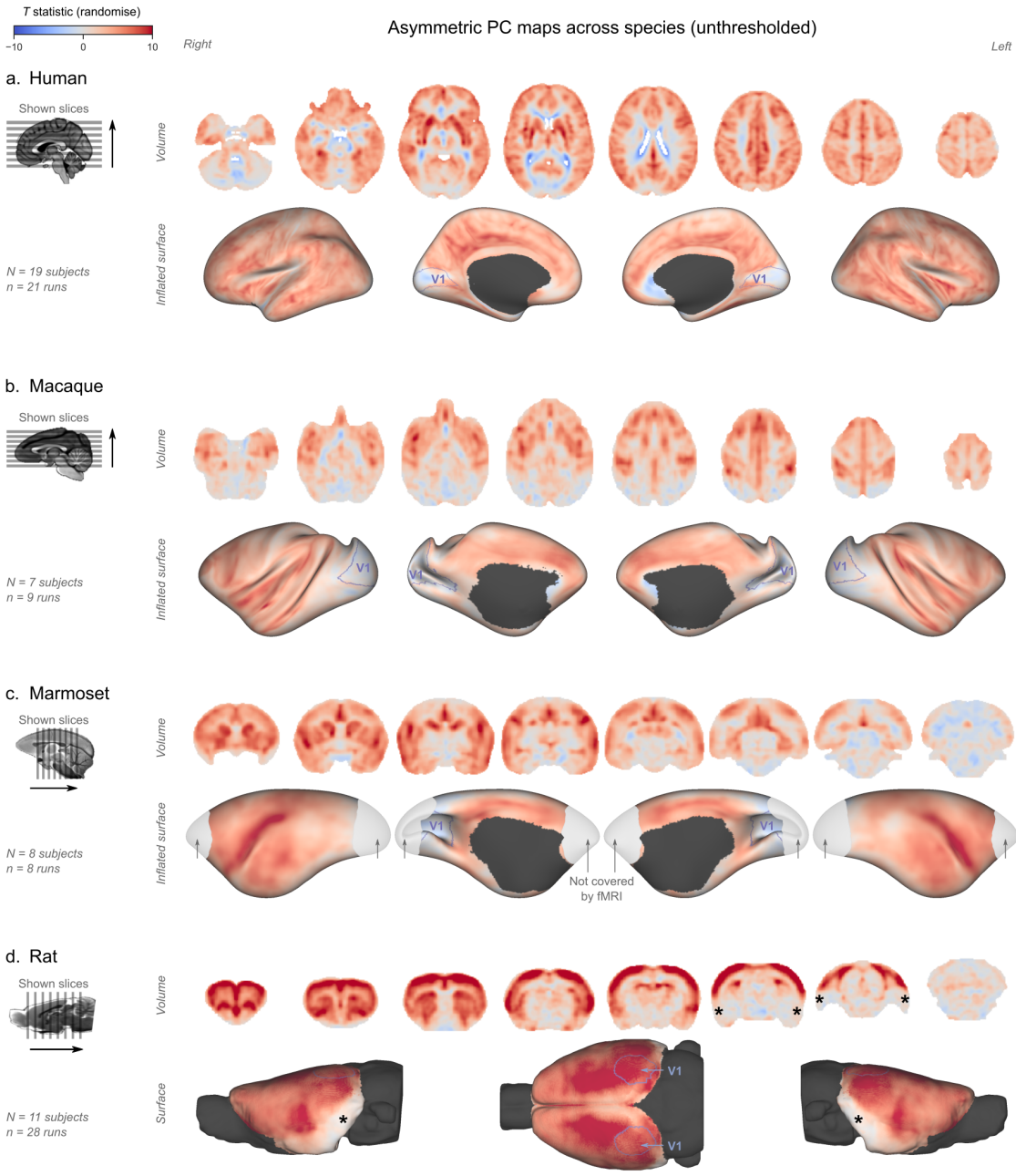

Figure A.6: Unthresholded burst-suppression maps across species. The group-level T statistic maps are shown here without thresholding, overlaid on volumetric slices and surfaces identical to the ones given in Figures 3.2, 3.3, 3.4, and 3.5. The location of V1 for each species is marked by purple outlines. Asterisks on the rat map indicate areas with low signal-to-noise ratio (see also Supplementary Figure A.7).

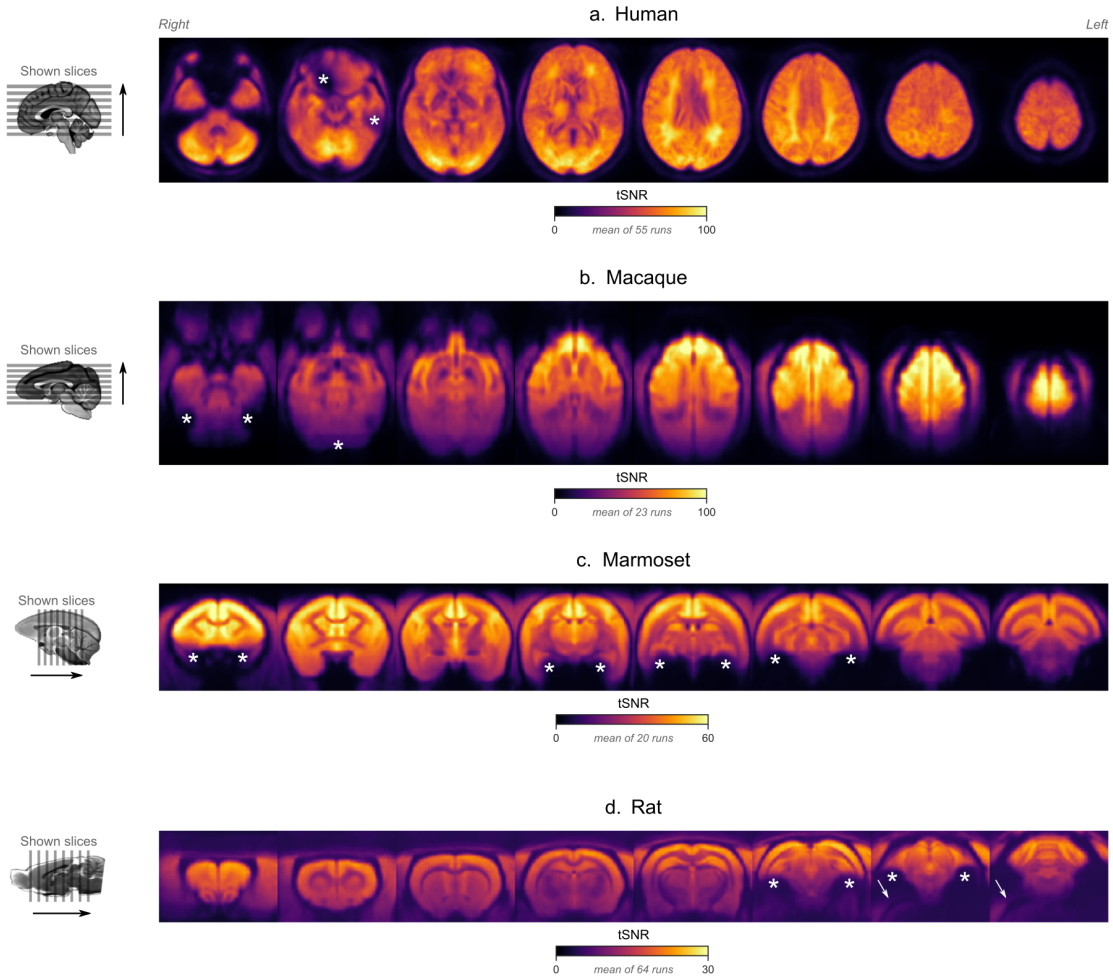

Figure A.7: Temporal signal-to-noise (tSNR) maps across species. The tSNR maps are overlaid on species-specific volumetric templates (same slices as in Figures 3.2, 3.3, 3.4, and 3.5). For each fMRI run, tSNR was computed prior to preprocessing, by dividing the mean of the EPI image across time with its standard deviation across time. The maps shown here represent the average tSNR values across all analyzed fMRI runs (with or without burst-suppression). Note the different scale bars for each species, indicating an overall reduction of tSNR in the smaller animals. Asterisks indicate areas with low tSNR, either due to increased distance from the coil (e.g. cerebellum in macaques), or due to susceptibility-induced distortions and signal drop-outs (e.g. orbitofrontal cortex in humans, medial temporal regions in marmosets, areas close to the ear canals in rats). An EPI ghost artifact is indicated by arrows on the rat map (**d**).

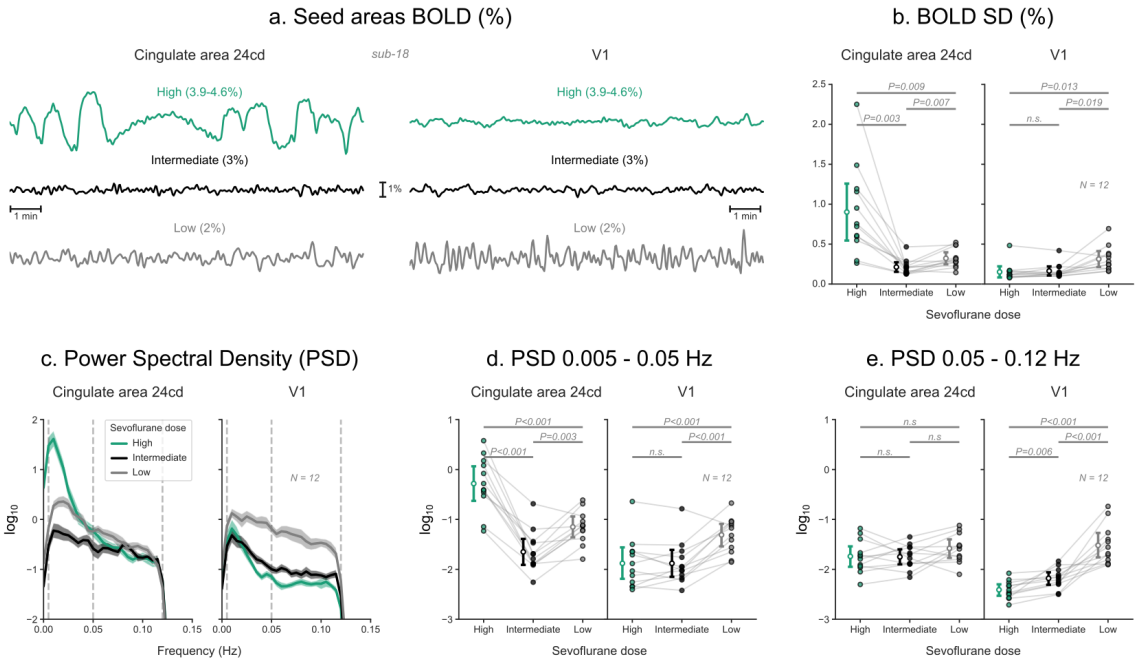

Figure A.8: BOLD signal timeseries across sevoflurane doses in humans. **a.** BOLD signal timeseries extracted from two regions-of-interest—left cingulate area 24cd and left V1—of a human subject, across three doses of sevoflurane anesthesia. **b.** The standard deviations (SD) of these timeseries are plotted as dots across 12 human subjects. The estimated Least Squares Means, with 95% confidence intervals, are plotted to the left of the dots. P values indicate the results of Tukey post-hoc pairwise comparisons, following a repeated-measure ANOVA (sevoflurane dose as the within-subject repeated measure). **c.** For each region and sevoflurane dose, the decadic logarithm of the BOLD signal's power spectral density (PSD) is plotted as mean ± SEM across the 12 subjects. Panels **d** and **e** show the integrated log10PSD within a low (0.005–0.05 Hz) and a high (0.05–0.12 Hz) frequency range, respectively. Estimated Least Squares Means, confidence intervals, and P values are shown as in panel **b**. N: number of subjects; n.s.: non-significant. Detailed results of repeated-measures ANOVAs and post-hoc tests are given in Table A.1 and Table A.2, respectively.

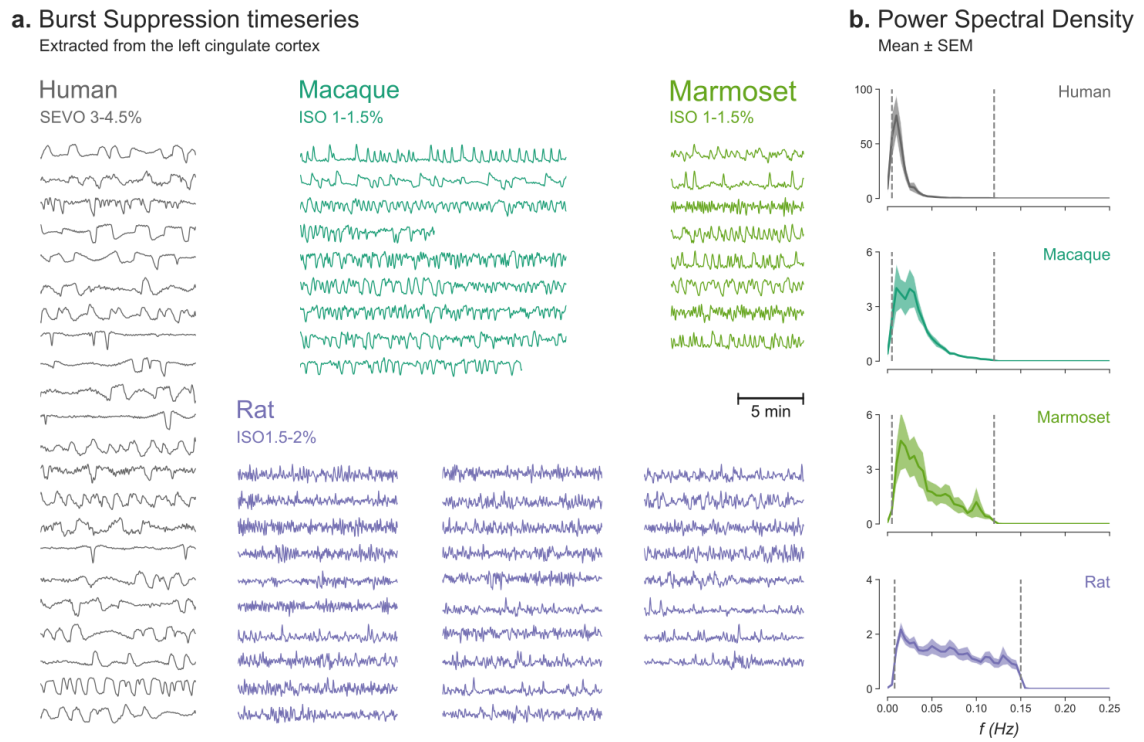

Figure A.9: Burst-suppression timescales across species. **a.** BOLD fMRI signal timeseries extracted from a region-of-interest in the cingulate cortex are shown for all runs classified as burst-suppression across the four species. This region—also used for the seed-based analysis (see Figure 3.6)—was selected because of its strong correlation with burst-suppression (i.e. asymmetric PCs) in all species. All timeseries are shown here min-max scaled (between 0 and 1) to put the emphasis on differences in time, not in amplitude. The timeseries peaks appear shorter in duration and occur more frequently as we move from humans to nonhuman primates and finally, to rats. This effect is reflected on the power spectral density plots of the timeseries (**b**), with increasingly higher frequencies being present from top to bottom. Power spectral density was computed from timeseries normalized to percent-signal-change (relative to the means), prior to min-max scaling. Vertical dashed lines indicate the cutoffs of the bandpass filter that was used for fMRI preprocessing.

VARIABLE	EFFECT	SPHER. CORR.	SUM OF SQ	DF	MEAN SQ	F	P	η^2
SD in Cg	Dose	GG	3.29	1.05	3.1310	16.5	0.002	0.470
	Residual	GG	2.20	11.56	0.1900			
SD in V1	Dose	GG	0.194	1.13	0.1723	11	0.005	0.285
	Residual	GG	0.194	12.38	0.0157			
PSD_{low} in Cg	Dose	None	11.51	2	5.7560	46.3	< 0.001	0.646
	Residual	None	2.74	22	0.1240			
PSD_{low} in V1	Dose	None	2.56	2	1.2785	23.2	< 0.001	0.293
	Residual	None	1.21	22	0.0552			
PSD_{high} in Cg	Dose	None	0.216	2	0.1082	1.82	0.186	0.073
	Residual	None	1.308	22	0.0595			
PSD_{high} in V1	Dose	GG	5.22	1.28	4.0790	36.2	< 0.001	0.677
	Residual	GG	1.58	14.07	0.1130			

Table A.1: Repeated-measures ANOVA results for Supplementary Figure A.8. SD: standard deviation; PSD_{low}: $\log_{10}$ of power spectral density integrated between 0.005–0.05 Hz; PSD_{high}: $\log_{10}$ of power spectral density integrated between 0.05–0.12 Hz; Cg: left cingulate area 24cd; V1: left primary visual cortex; Sq: squares; GG: Greenhouse-Geisser sphericity correction.

VARIABLE	COMPARISON	MEAN DIFFERENCE	SE	DF	t	P_{tukey}
SD in Cg	High - Intermediate	0.689	0.1571	11	4.39	0.003
	High - Low	0.580	0.1565	11	3.70	0.009
	Intermediate - Low	−0.109	0.0287	11	−3.89	0.007
SD in V1	High - Intermediate	−0.0119	0.0132	11	−0.905	0.649
	High - Low	−0.1613	0.0464	11	−3.472	0.013
	Intermediate - Low	−0.1493	0.0455	11	−3.280	0.019
PSD_{low} in Cg	High - Intermediate	1.369	0.156	11	8.79	< 0.001
	High - Low	0.868	0.159	11	5.48	< 0.001
	Intermediate - Low	−0.501	0.113	11	−4.42	0.003
PSD_{low} in V1	High - Intermediate	0.0029	0.0666	11	0.0436	0.999
	High - Low	−0.5639	0.1086	11	−5.1917	< 0.001
	Intermediate - Low	−0.5668	0.1066	11	−5.3177	< 0.001
PSD_{high} in V1	High - Intermediate	−0.228	0.0574	11	−3.98	0.006
	High - Low	−0.897	0.1355	11	−6.62	< 0.001
	Intermediate - Low	−0.669	0.1198	11	−5.58	< 0.001

Table A.2: Post-hoc pairwise tests for Supplementary Figure A.8. SD: standard deviation; PSD_{low}: $\log_{10}$ of power spectral density integrated between 0.005–0.05 Hz; PSD_{high}: $\log_{10}$ of power spectral density integrated between 0.05–0.12 Hz; Cg: left cingulate area 24cd; V1: left primary visual cortex.

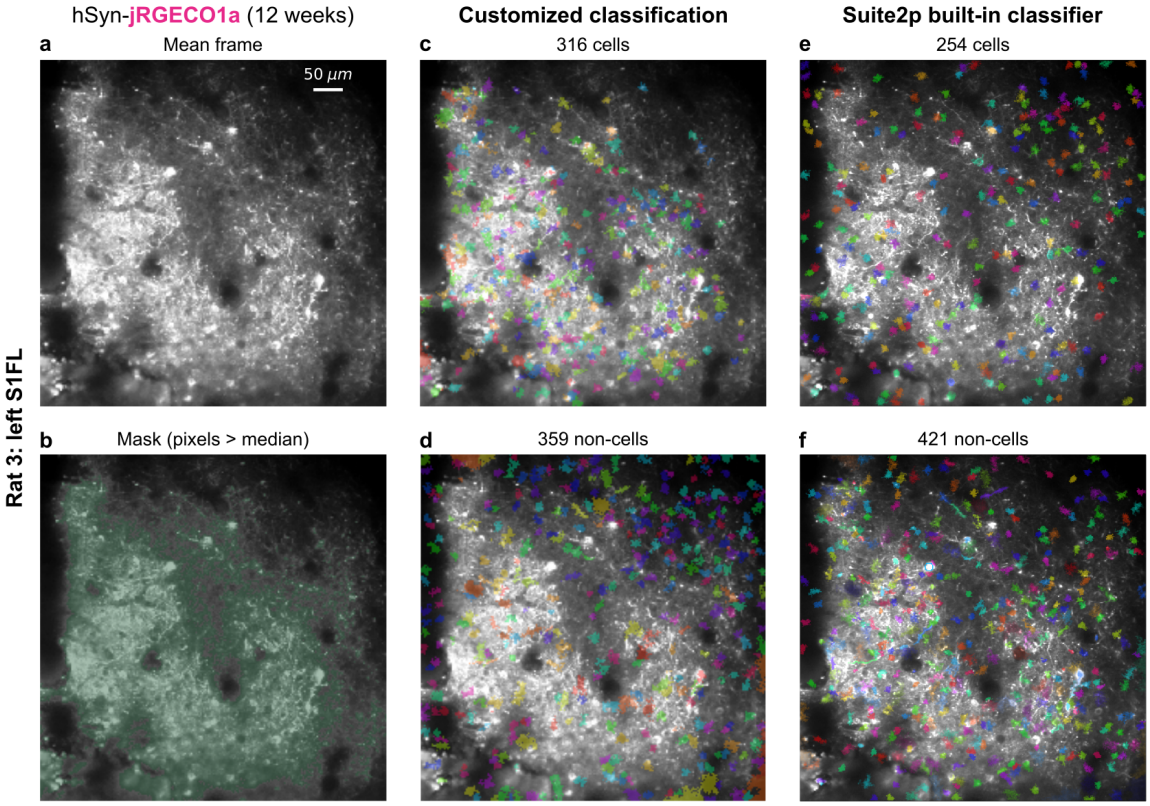

Figure A.10: ROI detection and cell classification. **a.** The mean frame of an example recording acquired in the left S1FL of Rat 3. Suite2p detected 675 ROIs, 254 of which were classified as cells (neuronal somata) by its built-in classifier (**e** and **f**). We customized the classification procedure, by first excluding ROIs in areas with low mean fluorescence (**b**) and then applying three decision criteria based on ROI morphology and activity trace skewness (see Section 4.2.9). Our customized procedure classified 316/675 ROIs as cells (**c** and **d**). ROI: region-of-interest; S1FL: forepaw region of the primary somatosensory cortex.

BIBLIOGRAPHY

Aedo-Jury, F., M. Schwalm, L. Hamzehpour, and A. Stroh (2020). "Brain states govern the spatio-temporal dynamics of resting-state functional connectivity." In: *eLife* 9.

Akrawi, W. P., J. C. Drummond, C. J. Kalkman, and P. M. Patel (1996). "A comparison of the electrophysiologic characteristics of EEG burst-suppression as produced by isoflurane, thiopental, etomidate, and propofol." In: *Journal of Neurosurgical Anesthesiology* 8.

Albers, F., L. Wachsmuth, T. M. van Alst, and C. Faber (2018). "Multimodal Functional Neuroimaging by Simultaneous BOLD fMRI and Fiber-Optic Calcium Recordings and Optogenetic Control." In: *Molecular Imaging and Biology* 20.

An, J., D. Jonnalagadda, V. Moura, P. L. Purdon, E. N. Brown, and M. B. Westover (2015). "Spatial variation in automated burst suppression detection in pharmacologically induced coma." In: *Annual International Conference of the IEEE Engineering in Medicine and Biology Society*.

Aquino, K. M., B. D. Fulcher, L. Parkes, K. Sabaroedin, and A. Fornito (2020). "Identifying and removing widespread signal deflections from fMRI data: Rethinking the global signal regression problem." In: *NeuroImage* 212.

Avants, B., C. Epstein, M. Gossman, and J. Gee (2008). "Symmetric diffeomorphic image registration with cross-correlation: Evaluating automated labeling of elderly and neurodegenerative brain." In: *Medical Image Analysis* 12.

Avants, B. B., N. J. Tustison, G. Song, P. A. Cook, A. Klein, and J. C. Gee (2011). "A reproducible evaluation of ANTs similarity metric performance in brain image registration." In: *NeuroImage* 54.

Avants, B. B., P. Yushkevich, J. Pluta, D. Minkoff, M. Korczykowski, J. Detre, and J. C. Gee (2010). "The optimal template effect in hippocampus studies of diseased populations." In: *NeuroImage* 49.

Bandettini, P. A., A. Jesmanowicz, E. C. Wong, and J. S. Hyde (1993). "Processing strategies for time-course data sets in functional MRI of the human brain." In: *Magnetic Resonance in Medicine* 30.

Bandettini, P. A., E. C. Wong, R. S. Hinks, R. S. Tikofsky, and J. S. Hyde (1992). "Time course EPI of human brain function during task activation." In: *Magnetic Resonance in Medicine* 25.

Barrière, D. A. et al. (2019). "The SIGMA rat brain templates and atlases for multimodal MRI data analysis and visualization." In: *Nature Communications* 10.

Benjamini, Y. and Y. Hochberg (1995). "Controlling the false discovery rate: a practical and powerful approach to multiple testing." In: *Journal of the Royal Statistical Society B* 57.

Biswal, B., F. Zerrin Yetkin, V. M. Haughton, and J. S. Hyde (1995). "Functional connectivity in the motor cortex of resting human brain using echo-planar MRI." In: *Magnetic Resonance in Medicine* 34.

Bojak, I., Z. V. Stoyanov, and D. T. Liley (2015). "Emergence of spatially heterogeneous burst suppression in a neural field model of electrocortical activity." In: *Frontiers in Systems Neuroscience* 9.

Bol, C. J. J. G., M. Danhof, D. R. Stanski, and J. W. Mandema (1997). "Pharmacokinetic-Pharmacodynamic Characterization of the Cardiovascular, Hypnotic, EEG and Ventilatory Responses to Dexmedetomidine in the Rat." In: *The Journal of Pharmacology and Experimental Therapeutics* 283.

Bol, C. J. J. G., J. P. W. Vogelaar, and J. W. Mandema (1999). "Anesthetic profile of dexmedetomidine identified by stimulus-response and continuous measurements in rats." In: *The Journal of Pharmacology and Experimental Therapeutics* 291.

Brenner, R. P. (1985). "The Electroencephalogram in Altered States of Consciousness." In: *Neurologic Clinics* 3. Symposium on Electrodiagnosis.

Brown, E. N., R. Lydic, and N. D. Schiff (2010). "General anesthesia, sleep, and coma." In: *NEJM* 363.

Brown, E. N., P. L. Purdon, and C. J. van Dort (2011). "General anesthesia and altered states of arousal: a systems neuroscience analysis." In: *Annual Review of Neuroscience* 34.

Brynildsen, J. K., L.-M. Hsu, T. J. Ross, E. A. Stein, Y. Yang, and H. Lu (2017). "Physiological characterization of a robust survival rodent fMRI method." In: *Magnetic Resonance Imaging* 35.

Buxton, R. B. and L. R. Frank (1997). "A model for the coupling between cerebral blood flow and oxygen metabolism during neural stimulation." In: *JCBFM* 17.

Buxton, R. B., E. C. Wong, and L. R. Frank (1998). "Dynamics of blood flow and oxygenation changes during brain activation: The balloon model." In: *Magnetic Resonance in Medicine* 39.

Chao, T. H. H., J. H. Chen, and C. T. Yen (2014). "Repeated BOLD-fMRI imaging of deep brain stimulation responses in rats." In: *PLoS ONE* 9.

Chen, T.-W. et al. (2013). "Ultra-sensitive fluorescent proteins for imaging neuronal activity." In: *Nature* 499.

Chen, X., F. Sobczak, Y. Chen, Y. Jiang, C. Qian, Z. Lu, C. Ayata, N. K. Logothetis, and X. Yu (2019). "Mapping optogenetically-driven single-vessel fMRI with concurrent neuronal calcium recordings in the rat hippocampus." In: *Nature Communications* 10.

Ching, S., P. L. Purdon, S. Vijayan, N. J. Kopell, and E. N. Brown (2012). "A neurophysiological-metabolic model for burst suppression." In: *PNAS* 109.

Clark, D. L. and B. S. Rosner (1973). "Neurophysiologic effects of general anesthetics. I. The electroencephalogram and sensory evoked responses in man." In: *Anesthesiology* 38.

Cloostermans, M. C., F. B. van Meulen, C. J. Eertman, H. W. Hom, and M. J. A. M. van Putten (2012). "Continuous electroencephalography monitoring for early prediction of neurological outcome in postanoxic patients after cardiac arrest." In: *Critical Care Medicine* 40.

Cordes, D., V. Haughton, J. D. Carew, K. Arfanakis, and K. Maravilla (2002). "Hierarchical clustering to measure connectivity in fMRI resting-state data." In: *Magnetic Resonance Imaging* 20.

Cox, R. W. (1996). "AFNI: software for analysis and visualization of functional magnetic resonance neuroimages." In: *Computers and Biomedical Research* 29.

Cramer, J. V., B. Gesierich, S. Roth, M. Dichgans, M. Düring, and A. Liesz (2019). "In vivo widefield calcium imaging of the mouse cortex for analysis of network connectivity in health and brain disease." In: *NeuroImage* 199.

Daal, R. J. J. van, Ç. Aydin, F. Michon, A. A. A. Aarts, M. Kraft, F. Kloosterman, and S. Haesler (2021). "Implantation of Neuropixels probes for chronic recording of neuronal activity in freely behaving mice and rats." In: *Nature Protocols* 16.

Damoiseaux, J. S., S. A. R. B. Rombouts, F. Barkhof, P. Scheltens, C. J. Stam, S. M. Smith, and C. F. Beckmann (2006). "Consistent resting-state networks across healthy subjects." In: *PNAS* 103.

Dana, H. et al. (2016). "Sensitive red protein calcium indicators for imaging neural activity." In: *eLife* 5.

Dana, H. et al. (2019). "High-performance calcium sensors for imaging activity in neuronal populations and microcompartments." In: *Nature Methods* 16.

Denk, W., J. H. Strickler, and W. W. Webb (1990). "Two-photon laser scanning fluorescence microscopy." In: *Science* 248.

Detsch, O., E. Kochs, M. Siemers, B. Bromm, and C. Vahle-Hinz (2002). "Increased responsiveness of cortical neurons in contrast to thalamic neurons during isoflurane-induced EEG bursts in rats." In: *Neuroscience Letters* 317.

Dijkhuizen, R. M., J. Ren, J. B. Mandeville, O. Wu, F. M. Ozdag, M. A. Moskowitz, B. R. Rosen, and S. P. Finklestein (2001). "Functional magnetic resonance imaging of reorganization in rat brain after stroke." In: *PNAS* 98.

Ebina, T. et al. (2018). "Two-photon imaging of neuronal activity in motor cortex of marmosets during upper-limb movement tasks." In: *Nature Communications* 9.

Emiliani, V., A. E. Cohen, K. Deisseroth, and M. Häusser (2015). "All-Optical Interrogation of Neural Circuits." In: *Journal of Neuroscience* 35.

Erhardt, E. B., S. Rachakonda, E. J. Bedrick, E. A. Allen, T. Adali, and V. D. Calhoun (2011). "Comparison of multi-subject ICA methods for analysis of fMRI data." In: *Human Brain Mapping* 32.

Fischl, B. (2012). "FreeSurfer." In: *NeuroImage* 62.

Fischl, B., M. I. Sereno, R. B. Tootell, and A. M. Dale (1999). "High-resolution intersubject averaging and a coordinate system for the cortical surface." In: *Human Brain Mapping* 8.

Flecknell, P. (2015). *Laboratory Animal Anaesthesia: Fourth Edition*. Elsevier Inc.

Fleischmann, A., S. Pilge, T. Kiel, S. Kratzer, G. Schneider, and M. Kreuzer (2018). "Substance-Specific Differences in Human Electroencephalographic Burst Suppression Patterns." In: *Frontiers in Human Neuroscience* 12.

Flynn, N. M., N. Bulijubasic, Z. J. Bosnjak, and J. P. Kampine (1992). "Isoflurane Produces Endothelium-independent Relaxation in Canine Middle Cerebral Arteries." In: *Anesthesiology* 76.

Fox, M. D. and M. E. Raichle (2007). "Spontaneous fluctuations in brain activity observed with functional magnetic resonance imaging." In: *Nature Reviews Neuroscience* 8.

Franks, N. P. (2008). "General anaesthesia: from molecular targets to neuronal pathways of sleep and arousal." In: *Nature Reviews Neuroscience* 9.

Froudist-Walsh, S., T. Xu, M. Niu, L. Rapan, D. S. Margulies, K. Zilles, X.-J. Wang, and N. Palomero-Gallagher (2021). "Gradients of receptor expression in the macaque cortex." In: *bioRxiv*.

Fulcher, B. D., J. D. Murray, V. Zerbi, and X.-J. Wang (2019). "Multimodal gradients across mouse cortex." In: *PNAS* 116.

Fultz, N. E., G. Bonmassar, K. Setsompop, R. A. Stickgold, B. R. Rosen, J. R. Polimeni, and L. D. Lewis (2019). "Coupled electrophysiological, hemodynamic, and cerebrospinal fluid oscillations in human sleep." In: *Science* 366.

Gao, Y.-R. R., Y. Ma, Q. Zhang, A. T. Winder, Z. Liang, L. Antinori, P. J. Drew, and N. Zhang (2017). "Time to wake up: Studying neurovascular coupling and brain-wide circuit function in the un-anesthetized animal." In: *NeuroImage* 153.

Gilson, M., N. E. Kouvaris, G. Deco, J. F. Mangin, C. Poupon, S. Lefranc, D. Rivière, and G. Zamora-López (2019). "Network analysis of whole-brain fMRI dynamics: A new framework based on dynamic communicability." In: *NeuroImage* 201.

Giovannucci, A. et al. (2019). "CaImAn an open source tool for scalable calcium imaging data analysis." In: *eLife* 8.

Glasser, M. F. et al. (2016). "A multi-modal parcellation of human cerebral cortex." In: *Nature* 536.

Glover, G. H. (1999). "Deconvolution of Impulse Response in Event-Related BOLD fMRI1." In: *NeuroImage* 9.

Goense, J. B. M. and N. K. Logothetis (2008). "Neurophysiology of the BOLD fMRI signal in awake monkeys." In: *Current biology* 18.

Golkowski, D. et al. (2017). "Coherence of BOLD signal and electrical activity in the human brain during deep sevoflurane anesthesia." In: *Brain and Behavior* 7.

Gorgolewski, K., C. D. Burns, C. Madison, D. Clark, Y. O. Halchenko, M. L. Waskom, and S. S. Ghosh (2011). "Nipype: A Flexible, Lightweight and Extensible Neuroimaging Data Processing Framework in Python." In: *Frontiers in Neuroinformatics* 5.

Grabner, G., A. L. Janke, M. M. Budge, D. Smith, J. Pruessner, and D. L. Collins (2006). "Symmetric atlasing and model based segmentation: An application to the hippocampus in older adults." In: *Lecture Notes in Computer Science*. Vol. 4191. Springer Verlag.

Grandjean, J. et al. (2020). "Common functional networks in the mouse brain revealed by multi-centre resting-state fMRI analysis." In: *NeuroImage* 205.

Greicius, M. (2008). "Resting-state functional connectivity in neuropsychiatric disorders." In: *Current Opinions in Neurology* 21.

Grienberger, C. and A. Konnerth (2012). "Imaging calcium in neurons." In: *Neuron* 73.

Grubb, R. L., M. E. Raichle, J. O. Eichling, and M. M. Ter-Pogossian (1974). "The Effects of Changes in PaCO2 Cerebral Blood Volume, Blood Flow, and Vascular Mean Transit Time." In: *Stroke* 5.

Hartig, R., D. Glen, B. Jung, N. K. Logothetis, G. Paxinos, E. A. Garza-Villarreal, A. Messinger, and H. C. Evrard (2021). "The Subcortical Atlas of the Rhesus Macaque (SARM) for neuroimaging." In: *NeuroImage* 235.

Hartikainen, K. M., M. Rorarius, J. J. Perakyla, P. J. Laippala, and V. Jantti (1995). "Cortical reactivity during isoflurane burst-suppression anesthesia." In: *Anesthesia and Analgesia* 81.

Helmchen, F. and W. Denk (2005). "Deep tissue two-photon microscopy." In: *Nature Methods* 2.

Hemmings, H. C. (2009). "Sodium channels and the synaptic mechanisms of inhaled anaesthetics." In: *British Journal of Anaesthesia* 103.

Hillman, E. M. C. (2014). "Coupling mechanism and significance of the BOLD signal: a status report." In: *Annual Review of Neuroscience* 37.

Hofmeijer, J., M. C. Tjepkema-Cloostermans, and M. J. A. M. van Putten (2014). "Burst-suppression with identical bursts: A distinct EEG pattern with poor outcome in postanoxic coma." In: *Clinical Neurophysiology* 125.

Hudetz, A. G. and O. A. Imas (2007). "Burst activation of the cerebral cortex by flash stimuli during isoflurane anesthesia in rats." In: *Anesthesiology* 107.

Huntenburg, J. M., L. Y. Yeow, F. Mandino, and J. Grandjean (2021). "Gradients of functional connectivity in the mouse cortex reflect neocortical evolution." In: *NeuroImage* 225.

Iida, H., H. Ohata, M. Iida, Y. Watanabe, and S. Dohi (1998). "Isoflurane and sevoflurane induce vasodilation of cerebral vessels via ATP-sensitive K+ channel activation." In: *Anesthesiology* 89.

Inan, H. et al. (2021). "Fast and statistically robust cell extraction from large-scale neural calcium imaging datasets." In: *bioRxiv*.

Jenkinson, M., C. F. Beckmann, T. E. Behrens, M. W. Woolrich, and S. M. Smith (2012). "FSL." In: *NeuroImage* 62.

Jonckers, E., D. Shah, J. Hamaide, M. Verhoye, and A. van der Linden (2015). "The power of using functional fMRI on small rodents to study brain pharmacology and disease." In: *Frontiers in pharmacology* 6.

Jun, J. J. et al. (2017). "Fully integrated silicon probes for high-density recording of neural activity." In: *Nature* 551.

Jung, B., P. A. Taylor, J. Seidlitz, C. Sponheim, P. Perkins, L. G. Ungerleider, D. Glen, and A. Messinger (2021). "A comprehensive macaque fMRI pipeline and hierarchical atlas." In: *NeuroImage* 235.

Kalthoff, D., C. Po, D. Wiedermann, and M. Hoehn (2013). "Reliability and spatial specificity of rat brain sensorimotor functional connectivity networks are superior under sedation compared with general anesthesia." In: *NMR in Biomedicine* 26.

Klapoetke, N. C. et al. (2014). "Independent Optical Excitation of Distinct Neural Populations." In: *Nature methods* 11.

Koletar, M. M., A. Dorr, M. E. Brown, J. McLaurin, and B. Stefanovic (2019). "Refinement of a chronic cranial window implant in the rat for longitudinal in vivo two-photon fluorescence microscopy of neurovascular function." In: *Scientific Reports* 9.

Korkmaz, S. and G. Wahlström (1997). "The EEG burst suppression threshold test for the determination of CNS sensitivity to intravenous anesthetics in rats." In: *Brain Research Protocols* 1.

Kroeger, D. and F. Amzica (2007). "Hypersensitivity of the anesthesia-induced comatose brain." In: *The Journal of Neuroscience* 27.

Kroeger, D., B. Florea, and F. Amzica (2013). "Human brain activity patterns beyond the isoelectric line of extreme deep coma." In: *PloS ONE* 8.

Kügler, S., E. Kilic, and E. Bähr (2003). "Human synapsin 1 gene promoter confers highly neuron-specific long-term transgene expression from an adenoviral vector in the adult rat brain depending on the transduced area." In: *Gene therapy* 10.

Lambers, H., M. Segeroth, F. Albers, L. Wachsmuth, T. M. van Alst, and C. Faber (2020). "A cortical rat hemodynamic response function for improved detection of BOLD activation under common experimental conditions." In: *NeuroImage* 208.

Land, R., G. Engler, A. Kral, and A. K. Engel (2012). "Auditory Evoked Bursts in Mouse Visual Cortex during Isoflurane Anesthesia." In: *PLoS ONE* 7.

Lecoq, J., N. Orlova, and B. F. Grewe (2019). "Wide. Fast. Deep: Recent Advances in Multiphoton Microscopy of In Vivo Neuronal Activity." In: *Journal of Neuroscience* 39.

Lewis, L. D., S. N. Ching, V. S. Weiner, R. A. Peterfreund, E. N. Eskandar, S. S. Cash, E. N. Brown, and P. L. Purdon (2013). "Local cortical dynamics of burst suppression in the anaesthetized brain." In: *Brain* 136.

Li, X., P. X. Morgan, J. Ashburner, J. Smith, and C. Rorden (2016). "The first step for neuroimaging data analysis: DICOM to NIfTI conversion." In: *Journal of Neuroscience Methods* 264.

Liang, Z., Y. Ma, G. D. R. Watson, and N. Zhang (2017). "Simultaneous GCaMP6-based fiber photometry and fMRI in rats." In: *Journal of Neuroscience Methods* 289.

Liang, Z., G. D. R. Watson, K. D. Alloway, G. Lee, T. Neuberger, and N. Zhang (2015). "Mapping the functional network of medial prefrontal cortex by combining optogenetics and fMRI in awake rats." In: *NeuroImage* 117.

Liley, D. T. J. and M. Walsh (2013). "The Mesoscopic Modeling of Burst Suppression during Anesthesia." In: *Frontiers in Computational Neuroscience* 7.

Lindauer, U. et al. (2010). "Neurovascular coupling in rat brain operates independent of hemoglobin deoxygenation." In: *JCBFM* 30.

Liu, C., F. Q. Ye, C. C.-C. Yen, J. D. Newman, D. Glen, D. A. Leopold, and A. C. Silva (2018). "A digital 3D atlas of the marmoset brain based on multi-modal MRI." In: *NeuroImage* 169.

Liu, C., C. C. C. Yen, D. Szczupak, X. Tian, D. Glen, and A. C. Silva (2021). "Marmoset Brain Mapping V3: Population multi-modal standard volumetric and surface-based templates." In: *NeuroImage* 226.

Liu, X., X.-H. Zhu, Y. Zhang, and W. Chen (2011). "Neural origin of spontaneous hemodynamic fluctuations in rats under burst-suppression anesthesia condition." In: *Cerebral Cortex* 21.

Liu, X., X. H. Zhu, Y. Zhang, and W. Chen (2013). "The change of functional connectivity specificity in rats under various anesthesia levels and its neural origin." In: *Brain Topography* 26.

Logothetis, N. K., J. Pauls, M. Augath, T. Trinath, and A. Oeltermann (2001). "Neurophysiological investigation of the basis of the fMRI signal." In: *Nature* 412.

Logothetis, N. K and J. Pfeuffer (2004). "On the nature of the BOLD fMRI contrast mechanism." In: *Magnetic Resonance Imaging* 22.

Lukasik, V. M. and R. J. Gillies (2003). "Animal anaesthesia for in vivo magnetic resonance." In: *NMR in Biomedicine* 16.

Lukatch, H. S., C. E. Kiddoo, and M. B. MacIver (2005). "Anesthetic-induced Burst Suppression EEG Activity Requires Glutamate-mediated Excitatory Synaptic Transmission." In: *Cerebral Cortex* 15.

Lukatch, H. S. and B. M. MacIver (1996). "Synaptic Mechanisms of Thiopental-induced Alterations in Synchronized Cortical Activity." In: *Anesthesiology* 84.

Luo, T. Z., A. G. Bondy, D. Gupta, V. A. Elliott, C. D. Kopec, and C. D. Brody (2020). "An approach for long-term, multi-probe neuropixels recordings in unrestrained rats." In: *eLife* 9.

Lyons, M. R. and A. E. West (2011). "Mechanisms of specificity in neuronal activity-regulated gene transcription." In: *Progress in Neurobiology* 94.

Mandino, F. et al. (2020). "Animal Functional Magnetic Resonance Imaging: Trends and Path Toward Standardization." In: *Frontiers in Neuroinformatics* 13.

Mansfield, P. (1977). "Multi-planar image formation using NMR spin echoes." In: *Journal of Physics C: Solid State Physics* 10.

Marcus, D. et al. (2011). "Informatics and Data Mining Tools and Strategies for the Human Connectome Project." In: *Frontiers in Neuroinformatics* 5.

Margulies, D. S. et al. (2016). "Situating the default-mode network along a principal gradient of macroscale cortical organization." In: *PNAS* 113.

Masamoto, K., M. Fukuda, A. Vazquez, and S.-G. Kim (2009). "Dose-dependent effect of isoflurane on neurovascular coupling in rat cerebral cortex." In: *The European Journal of Neuroscience* 30.

Masamoto, K. and I. Kanno (2012). "Anesthesia and the quantitative evaluation of neurovascular coupling." In: *JCBFM* 32.

Masamoto, K., T. Kim, M. Fukuda, P. Wang, and S.-G. Kim (2007). "Relationship between neural, vascular, and BOLD signals in isoflurane-anesthetized rat somatosensory cortex." In: *Cerebral Cortex* 17.

Milham, M. P. et al. (2018). "An Open Resource for Non-human Primate Imaging." In: *Neuron* 100.

Milham, M. et al. (2020). "Accelerating the Evolution of Nonhuman Primate Neuroimaging." In: *Neuron* 105.

Miller, K. L. et al. (2016). "Multimodal population brain imaging in the UK Biobank prospective epidemiological study." In: *Nature Neuroscience* 19.

Ming, Q. et al. (2021). "Isoflurane-Induced Burst Suppression Is a Thalamus-Modulated, Focal-Onset Rhythm With Persistent Local Asynchrony and Variable Propagation Patterns in Rats." In: *Frontiers in Systems Neuroscience* 14.

Mitchell, J. F. and D. A. Leopold (2015). "The marmoset monkey as a model for visual neuroscience." In: *Neuroscience Research* 93.

Moeller, S., E. Yacoub, C. A. Olman, E. Auerbach, J. Strupp, N. Harel, and K. Ugurbil (2010). "Multiband multislice GE-EPI at 7 tesla, with 16-fold acceleration using partial parallel imaging with application to high spatial and temporal whole-brain fMRI." In: *Magnetic Resonance in Medicine* 63.

Moraschi, M., M. DiNuzzo, and F. Giove (2012). "On the origin of sustained negative BOLD response." In: *Journal of Neurophysiology* 108.

Muller, L., F. Chavane, J. Reynolds, and T. J. Sejnowski (2018). "Cortical travelling waves: mechanisms and computational principles." In: *Nature Reviews Neuroscience* 19.

Mullinger, K. J., S. D. Mayhew, A. P. Bagshaw, R. Bowtell, and S. T. Francis (2014). "Evidence that the negative BOLD response is neuronal in origin: A simultaneous EEG-BOLD-CBF study in humans." In: *NeuroImage* 94.

Mumford, J. A., S. Horvath, M. C. Oldham, P. Langfelder, D. H. Geschwind, and R. A. Poldrack (2010). "Detecting network modules in fMRI time series: A weighted network analysis approach." In: *NeuroImage* 52.

Nagel, G., T. Szellas, W. Huhn, S. Kateriya, N. Adeishvili, P. Berthold, D. Ollig, P. Hegemann, and E. Bamberg (2003). "Channelrhodopsin-2, a directly light-gated cation-selective membrane channel." In: *PNAS* 100.

Nakai, J., M. Ohkura, and K. Imoto (2001). "A high signal-to-noise Ca2+ probe composed of a single green fluorescent protein." In: *Nature Biotechnology* 19.

Neher, E. and T. Sakaba (2008). "Multiple roles of calcium ions in the regulation of neurotransmitter release." In: *Neuron* 59.

Nickerson, L. D., S. M. Smith, D. Öngür, and C. F. Beckmann (2017). "Using Dual Regression to Investigate Network Shape and Amplitude in Functional Connectivity Analyses." In: *Frontiers in Neuroscience* 0.

Ogawa, S., T. M. Lee, A. R. Kay, and D. W. Tank (1990). "Brain magnetic resonance imaging with contrast dependent on blood oxygenation." In: *PNAS* 87.

Paasonen, J., R. A. Salo, A. Shatillo, M. M. Forsberg, J. Närväinen, J. K. Huttunen, and O. Gröhn (2016). "Comparison of seven different anesthesia protocols for nicotine pharmacologic magnetic resonance imaging in rat." In: *European Neuropsychopharmacology* 26.

Paasonen, J., P. Stenroos, R. A. Salo, V. Kiviniemi, and O. Gröhn (2018). "Functional connectivity under six anesthesia protocols and the awake condition in rat brain." In: *NeuroImage* 172.

Paasonen, J. et al. (2020). "Multi-band SWIFT enables quiet and artefact-free EEG-fMRI and awake fMRI studies in rat." In: *NeuroImage* 206.

Pachitariu, M., C. Stringer, M. Dipoppa, S. Schröder, L. F. Rossi, H. Dalgleish, M. Carandini, and K. D. Harris (2017). "Suite2p: beyond 10,000 neurons with standard two-photon microscopy." In: *bioRxiv*.

Pachitariu, M., C. Stringer, and K. D. Harris (2018). "Robustness of Spike Deconvolution for Neuronal Calcium Imaging." In: *Journal of Neuroscience* 38.

Pan, W.-J., J. C. W. Billings, J. K. Grooms, S. Shakil, and S. D. Keilholz (2015). "Considerations for resting state functional MRI and functional connectivity studies in rodents." In: *Frontiers in Neuroscience* 9.

Pasley, B. N., B. A. Inglis, and R. D. Freeman (2007). "Analysis of oxygen metabolism implies a neural origin for the negative BOLD response in human visual cortex." In: *NeuroImage* 36.

Pawela, C. P., B. B. Biswal, A. G. Hudetz, M. L. Schulte, R. Li, S. R. Jones, Y. R. Cho, H. S. Matloub, and J. S. Hyde (2009). "A protocol for use of medetomidine anesthesia in rats for extended studies using task-induced BOLD contrast and resting-state functional connectivity." In: *NeuroImage* 46.

Paxinos, G. and C. Watson (2007). *The rat brain in stereotaxic coordinates*. Elsevier.

Peeters, R. R., I. Tindemans, E. Schutter, and A. van der Linden (2001). "Comparing BOLD fMRI signal changes in the awake and anesthetized rat during electrical forepaw stimulation." In: *Magnetic Resonance Imaging* 19.

Pelled, G., K. H. Chuang, S. J Dodd, and A. P Koretsky (2007). "Functional MRI detection of bilateral cortical reorganization in the rodent brain following peripheral nerve deafferentation." In: *NeuroImage* 37.

Pilge, S., D. Jordan, M. Kreuzer, E. F. Kochs, and G. Schneider (2014). "Burst suppression-MAC and burst suppression-CP(5)(0) as measures of cerebral effects of anaesthetics." In: *British Journal of Anaesthesia* 112.

Pnevmatikakis, E. A. (2019). "Analysis pipelines for calcium imaging data." In: *Current Opinion in Neurobiology* 55.

Power, J. D. et al. (2011). "Functional network organization of the human brain." In: *Neuron* 72.

Power, J. D. (2017). "A simple but useful way to assess fMRI scan qualities." In: *NeuroImage* 154.

Powers, W. J., I. B. Hirsch, and P. E. Cryer (1996). "Effect of stepped hypoglycemia on regional cerebral blood flow response to physiological brain activation." In: *The American Journal of Physiology* 270.

Raichle, M. E. (2011). "The restless brain." In: *Brain Connectivity* 1.

Raichle, M. E., A. M. MacLeod, A. Z. Snyder, W. J. Powers, D. A. Gusnard, and G. L. Shulman (2001). "A default mode of brain function." In: *PNAS* 98.

Ranft, A. et al. (2016). "Neural Correlates of Sevoflurane-induced Unconsciousness Identified by Simultaneous Functional Magnetic Resonance Imaging and Electroencephalography." In: *Anesthesiology* 125.

Reimann, H. M. and T. Niendorf (2020). "The (Un)Conscious Mouse as a Model for Human Brain Functions: Key Principles of Anesthesia and Their Impact on Translational Neuroimaging." In: *Frontiers in Systems Neuroscience* 14.

Reimann, H. M. et al. (2018). "Somatosensory BOLD fMRI reveals close link between salient blood pressure changes and the murine neuromatrix." In: *NeuroImage* 172.

Ren, C. and T. Komiyama (2021). "Characterizing Cortex-Wide Dynamics with Wide-Field Calcium Imaging." In: *Journal of Neuroscience* 41.

Rocha, F. A. d. F., B. D. Gomes, L. C. d. L. Silveira, S. L. Martins, R. G. Aguiar, J. M. de Souza, and D. F. Ventura (2016). "Spectral Sensitivity Measured with Electroretinogram Using a Constant Response Method." In: *PLOS ONE* 11.

Rudolph, U. and B. Antkowiak (2004). "Molecular and neuronal substrates for general anaesthetics." In: *Nature Reviews Neuroscience* 5.

Sadakane, O. et al. (2015). "In Vivo Two-Photon Imaging of Dendritic Spines in Marmoset Neocortex." In: *eNeuro* 2.

Sanchez-Vives, M. V., M. Massimini, and M. Mattia (2017). "Shaping the Default Activity Pattern of the Cortical Network." In: *Neuron* 94.

Santisakultarm, T. P., C. J. Kersbergen, D. K. Bandy, D. C. Ide, S. H. Choi, and A. C. Silva (2016). "Two-photon imaging of cerebral hemodynamics and neural activity in awake and anesthetized marmosets." In: *Journal of Neuroscience Methods* 271.

Schulz, K., E. Sydekum, R. Krueppel, C. J. Engelbrecht, F. Schlegel, A. Schröter, M. Rudin, and F. Helmchen (2012). "Simultaneous BOLD fMRI and fiber-optic calcium recording in rat neocortex." In: *Nature Methods* 9.

Schwalm, M. et al. (2017). "Cortex-wide BOLD fMRI activity reflects locally-recorded slow oscillation-associated calcium waves." In: *eLife* 6.

Scott, B. B., C. D. Brody, and D. W. Tank (2013). "Cellular Resolution Functional Imaging in Behaving Rats Using Voluntary Head Restraint." In: *Neuron* 80.

Seidlitz, J., C. Sponheim, D. Glen, F. Q. Ye, K. S. Saleem, D. A. Leopold, L. Ungerleider, and A. Messinger (2018). "A population MRI brain template and analysis tools for the macaque." In: *NeuroImage* 170.

Silva, A. C., A. P. Koretsky, and J. H. Duyn (2007). "Functional MRI impulse response for BOLD and CBV contrast in rat somatosensory cortex." In: *Magnetic Resonance in Medicine* 57.

Silverman, J. and W. W. Muir (1993). "A review of laboratory animal anesthesia with chloral hydrate and chloralose." In: *Laboratory Animal Science* 43.

Sinclair, M. D. (2003). "A review of the physiological effects of alpha2-agonists related to the clinical use of medetomidine in small animal practice." In: *The Canadian Veterinary Journal* 44.

Sirmpilatze, N., J. Baudewig, and S. Boretius (2019). "Temporal stability of fMRI in medetomidine-anesthetized rats." In: *Scientific Reports* 9.

Smith, S. M. and T. E. Nichols (2009). "Threshold-free cluster enhancement: Addressing problems of smoothing, threshold dependence and localisation in cluster inference." In: *NeuroImage* 44.

Sommers, M. G., J. van Egmond, L. H. D. J. Booij, and A. Heerschap (2009). "Isoflurane anesthesia is a valuable alternative for alpha-chloralose anesthesia in the forepaw stimulation model in rats." In: *NMR in Biomedicine* 22.

Steinmetz, N. A., C. Koch, K. D. Harris, and M. Carandini (2018). "Challenges and opportunities for large-scale electrophysiology with Neuropixels probes." In: *Current Opinion in Neurobiology* 50.

Steinmetz, N. A. et al. (2021). "Neuropixels 2.0: A miniaturized high-density probe for stable, long-term brain recordings." In: *Science* 372.

Stenroos, P., J. Paasonen, R. A. Salo, K. Jokivarsi, A. Shatillo, H. Tanila, and O. Gröhn (2018). "Awake rat brain functional magnetic resonance imaging using standard radio frequency coils and a 3D printed restraint kit." In: *Frontiers in Neuroscience*.

Stenroos, P. et al. (2021). "Isoflurane affects brain functional connectivity in rats 1 month after exposure." In: *NeuroImage* 234.

Steriade, M., F. Amzica, and D. Contreras (1994). "Cortical and thalamic cellular correlates of electroencephalographic burst-suppression." In: *Electroencephalography and Clinical Neurophysiology* 90.

Steriade, M., A. Nunez, and F. Amzica (1993). "A novel slow (< 1 Hz) oscillation of neocortical neurons in vivo: Depolarizing and hyperpolarizing components." In: *Journal of Neuroscience* 13.

Stringer, C. and M. Pachitariu (2019). "Computational processing of neural recordings from calcium imaging data." In: *Current Opinion in Neurobiology* 55.

Stringer, C., M. Pachitariu, N. Steinmetz, C. B. Reddy, M. Carandini, and K. D. Harris (2019). "Spontaneous behaviors drive multidimensional, brainwide activity." In: *Science* 364.

Stroh, A., H. Adelsberger, A. Groh, C. Rühlmann, S. Fischer, A. Schierloh, K. Deisseroth, and A. Konnerth (2013). "Making waves: initiation and propagation of corticothalamic Ca2+ waves in vivo." In: *Neuron* 77.

Svoboda, K. and R. Yasuda (2006). "Principles of Two-Photon Excitation Microscopy and Its Applications to Neuroscience." In: *Neuron* 50.

Swank, R. L. (1949). "Synchronization of spontaneous electrical activity of cerebrum by barbiturate narcosis." In: *Journal of Neurophysiology* 12.

Swank, R. L. and C. W. Watson (1949). "Effects of barbiturates and ether on spontaneous electrical activity of dog brain." In: *Journal of Neurophysiology* 12.

Todd, N., S. Moeller, E. J. Auerbach, E. Yacoub, G. Flandin, and N. Weiskopf (2016). "Evaluation of 2D multiband EPI imaging for high-resolution, whole-brain, task-based fMRI studies at 3T: Sensitivity and slice leakage artifacts." In: *NeuroImage* 124.

Trautmann, E. M. et al. (2019). "Accurate Estimation of Neural Population Dynamics without Spike Sorting." In: *Neuron* 103.

Tsuchiya, R., F. Yoshiki, Y. Kudo, and M. Morita (2002). "Cell type-selective expression of green fluorescent protein and the calcium indicating protein, yellow cameleon, in rat cortical primary cultures." In: *Brain Research* 956.

Tustison, N. J., B. B. Avants, P. A. Cook, Y. Zheng, A. Egan, P. A. Yushkevich, and J. C. Gee (2010). "N4ITK: Improved N3 bias correction." In: *IEEE Transactions on Medical Imaging*.

Ueki, M., F. Linn, and K. Hossmann (1988). "Functional activation of cerebral blood flow and metabolism before and after global ischemia of rat brain." In: *JCBFM* 8.

Van Essen, D. C., S. M. Smith, D. M. Barch, T. E. J. Behrens, E. Yacoub, and K. Ugurbil (2013). "The WU-Minn Human Connectome Project: an overview." In: *NeuroImage* 80.

Van Essen, D. and K. Ugurbil (2012). "The Future of the Human Connectome." In: *NeuroImage* 62.

Van Essen, D. C. V., C. J. Donahue, T. S. Coalson, H. Kennedy, T. Hayashi, and M. F. Glasser (2019). "Cerebral cortical folding, parcellation, and connectivity in humans, nonhuman primates, and mice." In: *PNAS* 116.

Vincent, J. L. et al. (2007). "Intrinsic functional architecture in the anaesthetized monkey brain." In: *Nature* 447.

Wade, A. R. (2002). "The Negative BOLD Signal Unmasked." In: *Neuron* 36.

Wang, J., X. Zuo, and Y. He (2010). "Graph-based network analysis of resting-state functional MRI." In: *Frontiers in Systems Neuroscience* 0.

Wang, M., Y. He, T. J. Sejnowski, and X. Yu (2018). "Brain-state dependent astrocytic Ca2+ signals are coupled to both positive and negative BOLD-fMRI signals." In: *PNAS* 115.

Weber, R., P. Ramos-Cabrer, D. Wiedermann, N. Van Camp, and M. Hoehn (2006). "A fully noninvasive and robust experimental protocol for longitudinal fMRI studies in the rat." In: *NeuroImage* 29.

Wenzel, M., S. Han, E. H. Smith, E. Hoel, B. Greger, P. A. House, and R. Yuste (2019). "Reduced Repertoire of Cortical Microstates and Neuronal Ensembles in Medically Induced Loss of Consciousness." In: *Cell Systems* 8.

Westover, M. B., S. Ching, V. M. Kumaraswamy, O. Akeju, E. Pierce, S. S. Cash, R. Kilbride, E. N. Brown, and P. L. Purdon (2015). "The human burst suppression electroencephalogram of deep hypothermia." In: *Clinical Neurophysiology* 126.

Williams, K. A., M. E. Magnuson, W. Majeed, S. M. LaConte, S. J. Peltier, X. Hu, and S. D. Keilholz (2010). "Comparison of alpha-chloralose, medetomidine and isoflurane anesthesia for functional connectivity mapping in the rat." In: *Magnetic Resonance Imaging* 28.

Winkler, A. M., G. R. Ridgway, M. A. Webster, S. M. Smith, and T. E. Nichols (2014). "Permutation inference for the general linear model." In: *NeuroImage* 92.

Wolf, T., U. Lindauer, A. Villringer, and U. Dirnagl (1997). "Excessive oxygen or glucose supply does not alter the blood flow response to somatosensory stimulation or spreading depression in rats." In: *Brain Research* 761.

Woolrich, M. W., B. D. Ripley, M. Brady, and S. M. Smith (2001). "Temporal Autocorrelation in Univariate Linear Modeling of FMRI Data." In: *NeuroImage* 14.

Worsley, K. J. (2001). "Statistical analysis of activation images." In: *Functional Magnetic Resonance Imaging*. Oxford University Press.

Wu, J., G. H. Ngo, D. Greve, J. Li, T. He, B. Fischl, S. B. Eickhoff, and B. T. Yeo (2018). "Accurate nonlinear mapping between MNI volumetric and FreeSurfer surface coordinate systems." In: *Human Brain Mapping* 39.

Yablonskiy, D. A., J. J. H. Ackerman, and M. E. Raichle (2000). "Coupling between changes in human brain temperature and oxidative metabolism during prolonged visual stimulation." In: *PNAS* 97.13.

Yeo, B. T. et al. (2011). "The organization of the human cerebral cortex estimated by intrinsic functional connectivity." In: *Journal of Neurophysiology* 106.

Young, G. B. (2000). "The EEG in coma." In: *Journal of Clinical Neurophysiology* 17.

Yu, X., Y. He, M. Wang, H. Merkle, S. J. Dodd, A. C. Silva, and A. P. Koretsky (2016). "Sensory and optogenetically driven single-vessel fMRI." In: *Nature Methods* 13.

Yushkevich, P. A., J. Piven, H. C. Hazlett, R. G. Smith, S. Ho, J. C. Gee, and G. Gerig (2006). "User-guided 3D active contour segmentation of anatomical structures: significantly improved efficiency and reliability." In: *NeuroImage* 31.

Zhang, D., H. Ding, D. Ye, X. Jia, and N. Thakor (2010). "Burst suppression EEG during hypothermia and rapid rewarming in isoflurane-anesthetized rats." In: *4th iCBBE*.

Zhang, F., L.-P. Wang, E. S. Boyden, and K. Deisseroth (2006). "Channelrhodopsin-2 and optical control of excitable cells." In: *Nature Methods* 3.

Zhang, Z., D.-C. Cai, Z. Wang, K. Zeljic, Z. Wang, and Y. Wang (2019). "Isoflurane-Induced Burst Suppression Increases Intrinsic Functional Connectivity of the Monkey Brain." In: *Frontiers in Neuroscience* 13.

Zhao, F., T. Zhao, L. Zhou, Q. Wu, and X. Hu (2008). "BOLD study of stimulation-induced neural activity and resting-state connectivity in medetomidine-sedated rat." In: *NeuroImage* 39.

Zucker, R. S. (1999). "Calcium- and activity-dependent synaptic plasticity." In: *Current Opinion in Neurobiology* 9.

van Alst, T. M., L. Wachsmuth, M. Datunashvili, F. Albers, N. Just, T. Budde, and C. Faber (2019). "Anesthesia differentially modulates neuronal and vascular contributions to the BOLD signal." In: *NeuroImage* 195.

There is no such thing as a self-made man.
We are made up of thousands of others.

— George Burton Adams

ACKNOWLEDGEMENTS

First and foremost, I wish to thank my PhD supervisor, Susann Boretius. She entrusted me with resources, time, moral support, and freedom to pursue my ideas. She was always available, going over and beyond what is expected of a supervisor. I cherish the brainstorming sessions in her office and her reassuring presence during experiments. Leading through example, she has fostered a welcoming environment for all lab members.

I probably would not be writing this thesis if not for Jürgen Baudewig. He taught me fMRI, got me excited about its capabilities and wary of its limitations. He recruited me to the lab and supervised my Master's thesis. His infectious child-like enthusiasm about all things science never failed to bring a smile to my face. I will never get rid of the impulsive urge to run into his office every time I get an exciting new result.

I looked forward to going to the lab every morning, and this is in no little part because of the supportive people waiting for me there. Rakshit Dadarwal embarked on his PhD journey at the same time as me and has been my trusty officemate ever since. I truly admire him for his kindness and perseverance in the face of adversity. Tor Rasmus Memhave joined us much later in the office but already managed to spark numerous interesting conversations. I thank him for proof-reading parts of this thesis and wish him good luck with his own research adventures. I am grateful to Philipp Schwedhelm for getting me excited about new methods and for pushing me out of my comfort zone. Without him this thesis would be one chapter shorter. The same goes for Jessica König, from whom I learned so much about surgery and anesthesia. Kristin Kötz is the technician every lab needs. I cannot count the number of times I called her to help me with a problem, and she always delivered. Michael Ortiz-Rios was ever eager to discuss science and kept me supplied with a steady stream of papers to read. Marco Deckers, an absolute wizard of electronics and 3D-printing, helped me with some of my setups. Kerstin Fuhrmann aided me with wet lab tasks and with ordering materials. Amir Moussavi, Judith Mylius, Renate Schweizer, Melanie Bückner, and Yasemin Betül Gültekin may not have worked with me directly but were always there when the need arose for helping hands and kind words. Shereen Petersen is probably the most capable secretary I will ever meet; there is nothing she cannot do. My thanks also go to the competent team of animal care takers for keeping our precious experimental subjects happy.

I had the fortune of working with many amazing collaborators. Special thanks go to Daniel Golkowski and Jaakko Paasonen for entrusting me with their data, and to Daniel

Hillier and Vladislav Kozyrev for supporting me through the calcium imaging experiments.

My PhD would not have been possible without the constant support of the IMPRS Neuroscience office. My thanks go to Jonas Barth, Franziska Kühne, and especially to Sandra Drube, for keeping this unique program up and running. I could not omit the late Michael Hörner, who contributed so much to making the program what it is. I also owe thanks to the members of my Thesis Advisory Committee—Professors Jochen Staiger and Hansjörg Scherberger—for their feedback and encouragement during our meetings.

Almost all analyses in this thesis were performed using free and open-source software. For that I am indebted to the people that believe in open science, and especially to the Brainhack community. I started this journey being clueless about coding. I owe all I know to the unsung heroes who share their code, write documentation, and leave helpful comments on obscure internet forums.

This goes to the people with whom I shared my life in Göttingen. To Dimos – we embarked on this journey together, through medical school, Master's, and PhD. You are perhaps the most intelligent and hard-working person I know, and I am lucky to have you here as my friend and family. I am looking forward to your exciting scientific accomplishments. To Myrto – thank you for brightening my life with your passion, warmth, and attention to detail. I relied on the last one quite a bit for this thesis, and I thank you for that. I admire your drive and perceptiveness; I am certain you will achieve whatever goals you set. To Tal – I am lucky for having known you as a classmate and a friend. I appreciate your sincerity, wit, and all the things we shared. To Tini – even if I left this town without a PhD degree, I would still feel fortunate for having met you here. Your support throughout the writing process was invaluable, through late night proof-reading or cooking. Here's to a thousand more dances.

To my family – I know how much you miss me and wish me by your side. I would not be the person I am without your love, trust, and support through thick and thin. To my mother – I owe my love of reading, thinking, and exploring to you. You deserved to see me kiss the Gänseliesel.

— Thank you